

NA 031443

OS-137

K

AN ANALYTICAL AND EXPERIMENTAL INVESTIGATION
OF THE HOVERING DYNAMICS
OF THE
AEROCRANE HYBRID HEAVYLIFT VEHICLE

ALL AMERICAN ENGINEERING COMPANY
P.O. Box 1247 801 S. Madison St.
Wilmington, DE 19899

June 1976

Final Report

Approved for Public Release

Distribution Unlimited

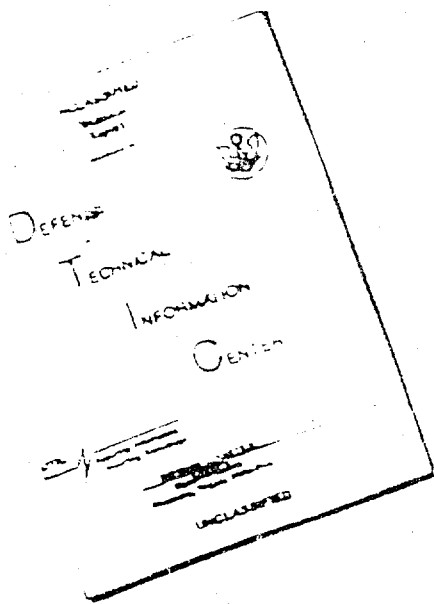
Prepared for:

DEPARTMENT OF THE NAVY
Naval Air Systems Command (03P32)
Washington, D.C. 20381

DEPARTMENT OF THE NAVY
Naval Air Development Center (31P3)
Air Vehicle Technology Department
Warminster, PA 18974

9 D D C
RECEIVED
NOV 1 1976
REFUGEE
D

DISCLAIMER NOTICE



THIS DOCUMENT IS BEST
QUALITY AVAILABLE. THE COPY
FURNISHED TO DTIC CONTAINED
A SIGNIFICANT NUMBER OF
PAGES WHICH DO NOT
REPRODUCE LEGIBLY.

UNCLASSIFIED

SECURITY CLASSIFICATION OF THIS PAGE (When Data Entered)

REPORT DOCUMENTATION PAGE		READ INSTRUCTIONS BEFORE COMPLETING FORM
1. REPORT NUMBER 14	2. GOVT ACCESSION NO. OS-137	3. RECIPIENT'S CATALOG NUMBER
4. TITLE (or Summary) 6 An Analytical and Experimental Investigation of the Hovering Dynamics of the Aerocrane Hybrid Heavy Lift Vehicle.		4. DATE OF REPORT/PERIOD COVERED 9 Final <i>rept.</i>
5. AUTHOR(s) Princeton University 10 W.F. Putt, Jr. H.C. Curtiss, Jr.		6. PERFORMING ORGANIZATION NUMBER OS-137
7. PERFORMING ORGANIZATION NAME AND ADDRESS All American Engineering Company P.O. Box 1247 801 S. Madison Street Wilmington, DE 19899		8. CONTRACT OR GRANT NUMBER(s) 15 N0019-75-C-0418
9. CONTROLLING OFFICE NAME AND ADDRESS Department of the Navy Naval Air Systems Command (03P32) Washington, D.C. 20361		10. PROGRAM ELEMENT, PROJECT, TASK AREA & WORK UNIT NUMBERS Air Task A03P-03P3/ 001B/6WF41-411-001 Work Unit No. DH806
11. MONITORING AGENCY NAME & ADDRESS (if different from Controlling Office) Department of the Navy Naval Air Development Center (31P3) Air Vehicle Technology Department Warminster, PA 18974		12. REPORT DATE 11 Jun 1976
13. DISTRIBUTION STATEMENT (of this Report) Approved for Public Release Distribution Unlimited		14. NUMBER OF PAGES 12 96p 94
15. DISTRIBUTION STATEMENT (of the abstract entered in Block 20, if different from Report) 16 ADSP-03P3/001-B6WF41-411-001		
16. SUPPLEMENTARY NOTES		
17. KEY WORDS (Continue on reverse side if necessary and identify by block number) AEROCRANE DYNAMIC STABILITY VTOL HEAVY-LIFT HOVER HYBRID		
18. ABSTRACT (Continue on reverse side if necessary and identify by block number) The results of an analytical and experimental investigation of the hovering dynamics of an AEROCRANE hybrid heavy lift vehicle are discussed and compared. Analytical representations of the hovering aerodynamics and equations of motion are developed and discussed. The experimental program, including flight test of a 0.107 scale Froude model, is discussed. Piloted and unpiloted analog computer simulations of the hovering dynamics are compared with flight test results. The influence of feedback stabilization is investigated and recommendations made for a stabilization system to improve the hovering operation by a remote pilot with limited motion cues.		

SECURITY CLASSIFICATION OF THIS PAGE (When Data Entered)

SECURITY CLASSIFICATION OF THIS PAGE (When Data Entered)

INTRODUCTION

In mid-1974 All American Engineering Company (AAE) funded, built and flew at the Company's Wilmington Delaware plant a 0.1 Froude Scaled free flight spherical model of a 50 ton slingload AEROCRANE. In October 1974 AAE proposed to the U.S. Navy a program to perform the engineering and fabrication to modify the model to provide proportional remote control; install instrumentation and provide a monitoring station; conduct flight tests in a government airship hanger; and reduce flight data. This was responsive to the U.S. Navy/U.S. Forest Service interest in the AEROCRANE concept and its potential application to a variety of civil and military short haul heavy lift applications.

In June 1975 the Navy issued contract N00019-75-C-0418 to perform the work proposed, including the planning and execution of a flight test program at the Naval Air Station, Lakehurst, New Jersey, to determine:

- a. Trim conditions for a range of speeds, gross weights and vertical center of gravity positions.
- b. Rigid airframe dynamics in response to discrete control input excitations.
- c. Regions of deteriorated flying qualities in forward flight and vertical descent.

The Navy selected the Naval Air Development Center (NADC), Warminster, Pennsylvania to provide technical direction of the contract effort. AAE selected Princeton University (Department of Aerospace and Mechanical Sciences), Princeton, New Jersey as its subcontractor for model instrumentation, flight test, and data collection and analysis.

By October 1975 it was apparent that weight and cost growth in the model, mostly associated with the instrumentation package, would necessitate the construction of a new, larger 0.1 Froude scaled model. This led to schedule slippage and cost growths which were accommodated in a contract amendment in March 1976 providing for the construction and flight test of a new model.

Hovering flight tests commenced in Hanger No. 1 at the Naval Air Station, Lakehurst on 13 April 1976. These continued until 22 April 1976 at which time the test model received minor damage during an in-flight contact with an extended boom of the ground support vehicle. The primary cause of the "accident" was the development of a mild instability in hovering flight. The ground based controller had difficulty in detecting this instability, in its incipient stages, from his observation point on the ground. This contributed to, and was aggravated by, failure of the heading - hold retrograde system of the model and resulted in loss of control. This report discusses, *inter alia*, this instability and the relatively simple, straightforward corrective measures recommended for adoption in future flight test vehicles. Moreover, it reports the successful development of a verified analytical model which can be used in forecasting future test results.

Following damage to the test model, NADC, NAVAIR and the Contractor mutually agreed: that the objectives of the hovering phase of the flight test program had been achieved, that the data collected during that phase should be reduced and analyzed, that the hovering phase results were to be reported, and the effort under contract N00019-75-C-0418 be limited to hovering flight tests. This was effectuated in a contract amendment dated 6 August 1976.

The report which follows constitutes a summation of all effort under the aforementioned contract.

ACCESSION NO.	
1118	DATA SOURCE
104	<input checked="" type="checkbox"/> DATA SOURCE
MANUFACTURER	
NOTIFICATION	
BY	
REF ID: A6459400000000000000000000000000	
COMPUTER INTEGRITY CODES	
10000000000000000000000000000000	
SPECIAL	
A	

D D C
 RECORDED
 NOV 1 1976
 REQUESTED
 D

AN ANALYTICAL AND EXPERIMENTAL INVESTIGATION
OF THE HOVERING DYNAMICS OF THE
AEROCRANE HYBRID HEAVY LIFT VEHICLE

by

W. F. Putman and
H. C. Curtiss, Jr.

Technical Report 1291

Princeton University
Department of Aerospace and Mechanical Sciences

D D C
RECORDED
NOV 1 1978
RECORDED
D

June 1976

DISTRIBUTION STATEMENT A
Approved for public release;
Distribution Unlimited

SUMMARY

A 0.107 Froude scaled dynamically similar free flight model of a proposed 10-ton payload AEROCANE vehicle was designed, fabricated and tested in hovering flight by the staff of the Dynamic Model Track, Aerospace and Mechanical Sciences Department, Princeton University. In addition to the model, instrumentation and ground support equipment necessary to operate the model were designed and fabricated. The experimental program was conducted in Hangar No. 1 at Lakehurst Naval Air Station, Lakehurst, New Jersey.

An analytical representation of the hovering flight dynamics was developed including theoretical techniques for prediction of the vehicle aerodynamic stability derivatives. These analytical representations were employed in an analog computer simulation of the vehicle dynamics to investigate the dynamic motions of the model in hovering flight.

Excellent correlation of the analog simulation with the experimentally observed vehicle dynamics was obtained. In addition, a simplified analytical representation of the vehicle dynamics was developed which provided good physical insight into the dynamic motions and aided greatly the understanding and interpretation of the dynamic behavior in hovering flight.

Studies were made analytically and with the analog simulator of the influence of feedback stabilization on the vehicle's hovering dynamics, with and without piloting. It was determined that a feedback stabilization utilizing crossed altitude feedback was both practical and effective in stabilizing the motions and allowing the remote operator to position the model satisfactorily in hovering flight.

TABLE OF CONTENTS

	<u>Page</u>
LIST OF ILLUSTRATIONS.....	i
NOMENCLATURE.....	iii
INTRODUCTION.....	1
EXPERIMENTAL APPARATUS.....	4
TABLE I: MODEL GEOMETRIC AND INERTIAL CHARACTERISTICS.....	5
EXPERIMENTAL PROGRAM.....	15
EQUATIONS OF MOTION.....	20
DYNAMIC STABILITY.....	29
FEEDBACK EFFECTS.....	36
ANALOG SIMULATION.....	40
CONCLUSIONS.....	46
RECOMMENDATIONS.....	47
REFERENCES.....	48
FIGURES.....	49
APPENDIX A: ROTOR AERODYNAMICS.....	77
APPENDIX B: NUMERICAL VALUES FOR STABILITY DERIVATIVES.....	91

LIST OF ILLUSTRATIONS

<u>Figure</u>		<u>Page</u>
1	Overall View of Dynamic Model.....	49
2	Dynamic Model in Hovering Flight.....	50
3	General Arrangement Drawing of Model.....	51
4	Internal Assembly Structure.....	52
5	Rotating Wings of Model.....	53
6	Rotating Wing Root Assembly.....	54
7	Rotating Wing Tip Assembly and Nacelle.....	55
8	Propulsion System Assembly.....	56
9	Rotating Wing Pitch Actuator Assembly.....	57
10	Goniola Assembly.....	58
11	Umbilical Support Boom.....	59
12	Pilot's Control Console.....	60
13	Engineer's Control Console.....	61
14	Angle of Attack and Sideslip Vanes.....	62
15	Axis System and Nomenclature.....	63
16	Angular Dynamic Modes of Motion of AEROCRANE.....	64
17	Stability Boundaries as a Function of Pendulous Mode Frequency.....	65
18	Physical Picture of Retrograde Mode Motion.....	66
19	Physical Picture of Advancing Mode Motion.....	67
20	Typical Transient Response of AEROCRANE in Hovering Flight to Longitudinal Control Step Input.....	68
21	Stability Boundaries in Dimensionless Form Including Dependence of Model Characteristics on Thrust Coefficient..	69

<u>Figure</u>		<u>Page</u>
22	Dimensionless Stability Boundaries, Thrust Coefficient vs. Dimensionless Pendulous Frequency Squared.....	70
23	Root Locus, Dual Axis Attitude Feedback.....	71
24	Root Locus, Dual Axis Rate Feedback.....	72
25	Analog Schematic.....	73
26	Time History - Nominal Configuration.....	74
27	Time History - Nominal Configuration Limit Cycle as Compared to Flight Test Data	75
28	Time History - Crossed Attitude Feedback, $K_A = 0.1\%$	76
A-1	Definition of Rotor Forces and Moments.....	88
A-2	Comparison of Theory and Experiment for Control Effectiveness of Rigid Propeller.....	89
A-3	Variation of Cosine Component of Induced Velocity with Forward Speed and Angle of Attack as Determined by Theory of Reference 7.....	90

NOMENCLATURE

a	rotor blade lift curve slope
Δ_{1s}	longitudinal cyclic pitch
b	number of blades
Δ_{1s}	lateral cyclic pitch
c	blade chord, ft
C_D	drag coefficient of centerbody, $C_D = \frac{D}{\frac{1}{2} \rho V^2 \pi R_0^2}$
C_L	rolling moment coefficient, $C_L = \frac{L}{\rho \pi R^2 (\Omega R)^2 R}$
C_{Lm}	magnus force coefficient of centerbody, $C_{Lm} = \frac{L_m}{\frac{1}{2} \rho V^2 \pi R_0^2}$
C_M	pitching moment coefficient, $C_M = \frac{M}{\rho \pi R^2 (\Omega R)^2 R}$
C_T	thrust coefficient, $C_T = \frac{T}{\rho \pi R^2 (\Omega R)^2}$
F_B	buoyant force, lbs
F_B	rotor inplane force, body axis system, positive to the rear, lb
H_u, M_u	stability derivatives divided by m' and I' respectively
I'	moment of inertia of vehicle including apparent mass contribution
I_0	vehicle moment of inertia about X and Y axes, slug ft ²
I_z	vehicle moment of inertia about Z axis, slug ft ²
J	proportionality constant between harmonic inflow and rotor aerodynamic moment

\bar{K}_a	attitude feedback gain, in general a complex number, rad/rad/ or deg/deg
\bar{K}_r	rate feedback gain, in general a complex number, rad/rad/sec
L_s	rolling moment, body axes, positive right side down, ft-lb
L_h	rotor hub moment in roll, body axes, ft-lb
m'	sum of mass of vehicle and apparent mass, slugs
m_A	apparent mass of vehicle, calculated for centerbody only, slugs
m_o	vehicle mass, slugs
M_s	pitching moment, body axes, positive nose up, ft-lb
M_h	rotor hub moment in pitch, body axes, ft-lb
p	vehicle roll rate, positive right side down, rad/sec
q	vehicle pitch rate, positive nose up, rad/sec
\bar{q}, \bar{p}	dimensionless pitch and roll rate, $\bar{q} = \frac{q}{\Omega}$, $\bar{p} = \frac{p}{\Omega}$
r_o	distance between center of buoyancy and center of gravity, positive for center of gravity below center of buoyancy, ft
R	radius of rotor, ft
R_b	radius of centerbody, ft
S	frontal area of centerbody, ft ² , Laplace operator
t	time
T_s	rotor thrust, along shaft, positive up, lbs
u	longitudinal velocity, positive for forward motion, ft/sec
\bar{u}, \bar{v}	dimensionless translational velocities, $\bar{u} = \frac{u}{\Omega R}$, $\bar{v} = \frac{v}{\Omega R}$
v	lateral velocity, positive moving to right, ft/sec
V	volume of centerbody, ft ³

w	complex translational velocity, $w = u - i v$, fps
W	weight of vehicle, lbs
X_b	longitudinal force, body axes, positive forward, lb
Y_b	lateral force, body axes, positive to right, lb
\bar{z}	complex translational displacement of center of gravity of vehicle, $\bar{z} = x - i y$
α_{BE}	blade element angle of attack
δ	complex control input, $\delta = A_{1s} - B_{1s}$, rad; blade profile drag coefficient
η	complex angular displacement, $\eta = \theta + i \phi$, rad
θ	blade pitch angle with respect to shaft axis system $\theta = \theta_0 - A_{1s} \cos \psi - B_{1s} \sin \psi$
θ	vehicle pitch angle, positive nose up, rad
θ_0	rotor collective pitch, rad
λ	rotor inflow ratio, positive for flow up through rotor
λ_s	cosine component of dimensionless induced velocity due to blow back, $\lambda_s = \lambda_1 x$
λ_m, λ_t	harmonic inflow components due to rotor aerodynamic pitching and rolling moments, $\lambda_m = j \frac{2C_m}{a\sigma}$, $\lambda_t = - j \frac{2C_L}{a\sigma}$
λ_1	rate of change of cosine component dimensionless of induced velocity with radius due to "blow back"
μ	rotor advance ratio
v	constant part of induced velocity non-dimensionalized by ΩR

ρ	density of air, slugs/ft ³
σ	rotor solidity $\sigma = \frac{bc}{\pi R}$
ϕ	rotor blade inflow angle
ϕ	vehicle roll angle, positive right side down, rad
ψ	blade azimuth angle, measured from downwind, positive in direction of rotation
ω_c	nutation frequency, $\omega_c = \frac{I_z}{I'} \Omega$, rad/sec
ω_p^2	square of pendulous frequency, $\omega_p^2 = \frac{F_B r_o}{I'}$, rad ² /sec ²
Ω	rotor/centerbody angular velocity, RPM or rad/sec
Ω_N	natural frequency of vehicle motion
λ	fractional radius to root of blade $\lambda = \frac{R_s}{R}$
$\arg P$	argument of complex distance from pole to characteristic root
$\arg Z$	argument of complex distance from zero to characteristic root
$(\)_{s,w}$	rotor forces and moments in a shaft/wind system. $H_{s,w}$ is parallel to the relative wind vector and positive in ⁸ direction opposite to the vehicle motion. $Y_{s,w}$ is perpendicular to the relative wind vector and positive to the right. $M_{s,w}$ represented as a vector is positive to the right and $L_{s,w}$ is positive in the direction of motion.
(*)	differentiation with respect to time
$\frac{\partial M_H}{\partial V}$, etc	rotor aerodynamic stability derivatives

INTRODUCTION

This report presents the results of an experimental and theoretical investigation of the hovering dynamics of the AEROCRANE hybrid heavy lift vehicle.

There has been considerable interest in recent years in developing a very heavy lift vehicle capable of hovering and slow translational flight such that, it would be capable of moving payloads of the order of 50 tons, that is, well in excess of the capability of existing helicopters. If such a vehicle could be developed it would find many applications in both the military and commercial spheres, ranging from offloading ships to logging. One particularly attractive concept for achieving this objective is the AEROCRANE, a unique concept proposed by the All American Engineering Company.⁽¹⁾ It consists of a spherical centerbody filled with lifting gas. Four rotating wings are mounted on the equator of the sphere and the entire assembly is rotated by propulsion systems mounted near the tips of the wings. Below the sphere, is mounted a gondola or pilots station which is yaw stabilized and does not rotate with the rest of the vehicle. The vehicle is configured such that the lifting gas provides a buoyant force equal to empty weight of the vehicle plus one half of the weight of the maximum payload. Vertical equilibrium is achieved through the thrust of the rotating wings obtained by means of a collective pitch control. Translation is obtained by cyclic pitch.

The success of this vehicle will depend to a large extent on the ability to hover and maneuver precisely at low speeds. This report describes an experimental and theoretical investigation to determine the hovering dynamic characteristics of such a vehicle using a Froude Scaled Dynamic Model of a proposed 50 ton payload vehicle.

A 0.107 Froude Scaled dynamic model of a proposed full scale AEROGRANE vehicle was designed and constructed by Princeton University. Hovering flight experiments were conducted to evaluate the control and dynamic response characteristics and a theoretical model was developed for comparison with the experimental results. The research program as originally planned included forward flight experiments as well. However, as described in this report owing to the nature of the dynamic characteristics of the vehicle in hovering, a more extensive hovering investigation was required. In addition, owing to the presence of a mild hovering instability in hovering flight a more extensive theoretical investigation was considered to be desirable in order to fully understand the hovering dynamics before proceeding to undertake forward flight experiments. In addition, it is considered highly desirable, as a result of the hovering flight experiments, to develop a theoretical model for the forward flight dynamics and to examine the estimated vehicle characteristics on an analog computer prior to proceeding with forward flight.

For a number of reasons a series of experiments with a Froude Scaled dynamic model was selected as the most efficient and cost effective means of determining the control characteristics of an AEROGRANE type vehicle rather than conducting a more conventional wind tunnel test. The primary reason for selecting an experimental investigation using a fully instrumented dynamic model was the unique configuration of the proposed vehicle. It appeared highly probable that a wind tunnel investigation based on conventional practice might not include measurement of the significant aerodynamic characteristics which determine the hovering dynamics. A

second reason of equal importance is the fact that since the proposed vehicle is designed for lifting, moving, and positioning precisely heavy payloads determination of the control and stability characteristics in hovering flight are of primary importance to the success of the vehicle. These characteristics are directly measured using a free flight model rather than being indirectly inferred from wind tunnel experiments. Further, since hovering flight is of major importance for this concept, very low speed experiments are required. Difficulties are encountered in obtaining experimental results in a wind tunnel at very low speeds owing to problems associated with maintaining a smooth uniform flow field without recirculation effects. It can be seen later in the report that one of the primary quantities determining the character of the hovering dynamics is the rate of change of pitching moment with translational velocity for velocities near hover, a quantity that would be difficult to measure in a wind tunnel but can be directly evaluated from a free flight model. The last factor of importance was the interest in achieving as large a Reynolds Number as possible on the centerbody. It was considered that a Froude Scaled free flight model with an overall diameter of approximately 30 feet would meet the Reynolds Number objective in a more cost effective manner than a wind tunnel model with comparable Reynolds Number.

This report presents a description of the model and the flight test program which was conducted. Experimental data obtained from the flight test program are presented along with a theoretical approach to predicting the dynamic stability characteristics in hovering flight.

EXPERIMENTAL APPARATUS

Model

The model employed for the experiments described in this report is a 0.107 Froude Scale model of a proposed 50 ton payload AEROGRANE vehicle. Photographs of the model are shown in Figures 1 and 2 and a general arrangement drawing indicating principal dimensions is shown in Figure 3. Table I presents a list of the important model inertial and aerodynamic characteristics.

Although it had been the original intent of the program to modify an existing uninstrumented 0.1 scale AEROGRANE model for use in the experimental investigation, detailed design studies indicated that this would not be desirable. The additional weight of the instrumentation package required for model control and data acquisition, even with a larger diameter gas envelope, would result in an average blade lift coefficient approximately 30% higher than the proposed full scale value. Thus a completely new model was required in order to maintain proper aerodynamic scaling.

It should also be noted that while a proposed full scale vehicle would have considerable excess buoyancy with no payload, it is not possible to achieve this condition on a small scale model owing to the increased specific weight of many of the components such as the power plants in addition to the fact that an instrumentation package was installed.

Model Structure

The internal structure of the model spherical centerbody consists of four mutually perpendicular radial members in the equatorial plane and a

TABLE I
MODEL GEOMETRIC AND INERTIAL CHARACTERISTICS

Nominal Configuration	
ROTOR DIAMETER	37.3 ft
SPHERE DIAMETER	16.0 ft
GROSS WEIGHT	191.7 lb
CENTER OF GRAVITY	3.82 ft below equator
$I_{\text{pitch \& roll about cg}}$	337.4 slug-ft ²
I_{polar}	481.5 slug-ft ²
THRUST	54 lb
BUOYANT LIFT	137.2 lb
VIRTUAL MASS	2.65 slugs
VIRTUAL INERTIA	38.7 slugs-ft ²
UMBILICAL WEIGHT	0.61 lb/ft

NOTE: All values listed are for nominal operating altitude and include sling load and umbilical contributions.

south pole member. These members, fabricated of 3" O.D. thin-wall aluminum tubing, are joined together at the center of the sphere by means of an aluminum weldment into which the radials and south pole are inserted and secured. The center joints are gas-tight thus allowing the instrumentation, control and power cabling to pass up through the south pole and out the radials to which the wings are attached. Gas-tight pass-throughs are provided in the gas-containing envelope to allow the radials and south pole to protrude through. A photograph of the internal structure assembly is shown in Figure 4.

The envelope itself, fabricated by ILC Corporation, is manufactured of Mylar impregnated Dacron sail cloth and in addition to the structure pass-throughs, the envelope is provided with a gas-tight access zipper, filling nozzle, and pressure measurement port. Eight load patches on the surface of the envelope are provided for attachment of the 1/16 in steel cable wing supports.

Wing Assemblies

The rotating wings or blades shown in a photograph in Figure 5, are constructed of balsa wood covered with a thin film of adhesive-backed plastic (Trade name "Mono-cote") with plywood and aluminum reinforcement at the load points. The root ends are provided with machined fittings for attachment of the wing-pitch servo actuators and the ball joint used to attach the wings to the tips of the radial tubes of the internal structure. A photograph showing the detail of this assembly, including the radial tube tip fittings, is shown in Figure 6.

The wing-support-cable tie-in fixtures are permanently assembled in

the wings as shown in the photograph in Figure 7. These fixtures are welded of aluminum tubing and are attached to the wing structure by means of a ball joint. Thus, the wing is simply supported with ball joints at either support; the lead-lag and flapping constraints are provided by the support cables and feathering constraint by the servo-actuators.

The propulsion system nacelle, including motor air cooling ducts, is constructed of plywood as an integral part of the wing structure and can be seen in the photograph in Figure 7.

Propulsion System Assembly

There are four propulsion system assemblies. Each consists of two permanent-magnet d.c. motors coupled to a propeller shaft through a 2.67:1 reduction provided by toothed timing belts and plastic sprockets. The 30 x 15 propeller is driven at a nominal speed of 2600 RPM. A brief wind tunnel test was conducted on a propulsion system assembly. The experimental results indicated a nominal operating condition of approximately 0.6 thrust horsepower and a propulsive efficiency of 75%. The motor-belt-box system will produce 1 horsepower continuously and can be run intermittently at 1.5 horsepower. A photograph of propulsion system assembly is shown in Figure 8.

Wing Pitch Actuators

A detail photograph of a wing pitch actuator assembly is shown in Figure 9. These units consist of a permanent magnet d.c. motor driving a ball-screw actuator through a spur gear pass. A 10-turn conductive

plastic follow-up potentiometer is provided to measure the actuator position (which corresponds to wing pitch angle) for the positioning loop closure and data recording purposes. It should be noted that the wing feathering actuation is done in the rotating system and hence no mechanical swashplate is required. Instead, first harmonic feathering (cyclic pitch) commands are electrically provided by means of a sine-cosine potentiometer mounted in the non-rotating system. The required computational electronics are provided in the ground-based controller system to allow first harmonic cyclic and collective commands.

The closed-loop positioning system consisting of the actuator assemblies driving the wing has a one half maximum amplitude bandwidth of approximately 5 Hz. The physical characteristic of this system is such that its response is acceleration limited. At the normal operating frequency of .5 Hz (30 RPM) it can be considered to have a transfer function equal to unity.

Gondola System

The non-rotating gondola is supported at the lower end of the south pole by a pair of large bore ball bearings which transmit the payload loads into the rotating structure. The gondola, attached to the south pole, can be seen in Figure 2, and a detail photograph of the gondola assembly is shown in Figure 10.

The gondola is positioned in azimuth by means of retrograde drive motor driving through a spur gear pass visible in Figure 10. The azimuth positioning control is accomplished by a closed loop positioning servo-mechanism driving the retrograde motor and utilizing integrated yaw - rate

gyro signals to maintain the heading hold. A back-up rate command loop is also provided which utilizes the yaw rate gyro signal directly. Damping and RPM sensing are provided by a d.c. tachometer.

Instrumentation and control signals and propulsive system power are carried from the non-rotating gondola to the rotating system by means of two slip ring systems, a Michigan Scientific instrumentation-quality 20-ring unit and a National Carbon high-current 8-ring unit, respectively.

The gondola carries the balance of the airborne instrumentation and control systems including the 3-axis gyro package and its electronic package, the air data boom and its electronics, propulsion power rectification and motor reversing equipment, first harmonic feathering sine-cosine potentiometer and the ballast support package. The balance of the instrumentation, control and power systems are mounted in the ground-based control system and connected to the model by a multiple conductor umbilical cable.

Ground Base

The ground based controller, which is mounted on a flat bed truck, provides all the necessary power, signal conditioning and controls to operate the model and record the data signals. It consists of the following sub-systems:

- 1.) a gasoline engine-driven 5 KVA, 120 v, 60 Hz, single phase, a.c. generator;
- 2.) a gasoline-driven 10 KVA, 200 v, 400 Hz, 3 ϕ alternator with a solid-state controller;
- 3.) power amplifier systems for the closed loop model control actuators;

- 4.) pilot's control console;
- 5.) flight engineer's console;
- 6.) data acquisition, signal conditioning and computational electronics and data recording equipment.

The entire controller, excluding the 60 Hz generator, is mounted on an 8' x 10' wooden pallet along with seating provisions for the pilot, flight engineer and test engineer; the pallet is in turn secured to the truck bed. Also mounted on the truck bed is a boom 47 ft. long fabricated of welded aluminum pipe and guyed to the truck with steel cables. The boom, shown in Figure 11, serves to support the ground based end of the umbilical cable in a position that will permit the lowest point of the umbilical catenary to clear ground obstructions and allow the model to be flown in a position relative to the truck where the pilot can observe both pitch and roll motions.

60 Hz Generator

The 5 KVA, 60 Hz generator is a commercial gasoline engine driven unit that provides all necessary power for the ground base with the exception of model main propulsion power.

400 Hz Alternator

The 10 KVA, 3 ϕ , 400 Hz gasoline engine driven alternator system was designed and assembled specifically to provide model propulsion power. It consists of a government surplus 400 Hz, 3 ϕ alternator belt driven by a 30 H Wisconsin gasoline engine with a clutch coupling. Alternator voltage output is controlled by a separately-excited solid-state field

control power supply. The power supply has provisions for automatic control of model RPM by use of the d.c. tachometer signal on the model gondola. Selection of manual or automatic control is provided at the flight engineer's console and a back-up self-excited field control provision allows model RPM control by the test engineer in the event of a power supply failure. The a.c. output is transmitted through the umbilical to the model where it is rectified to d.c.

Servo Power Amplifiers

The five d.c. power amplifiers used to provide loop closures and power amplification for the four wing pitch actuators and the retrograde drive motor are rack mounted in a cabinet at the flight engineer's position. The amplifiers are capable of operation at a continuous output of 100 watts with a bandwidth of d.c. to 10 KHz and contain signal summing, equalization and error detection circuits.

Pilot's Control Console

A photograph of the pilot's control console is shown in Figure 12. The console contains the centrally-mounted control stick with longitudinal and lateral cyclic commands and a top-mounted twist knob for heading command (or azimuth rate command in the back-up mode). Collective commands as well as longitudinal and lateral cyclic trim commands are provided by means of thumb-wheels arranged around the control stick. Three ten-turn digital dial potentiometers are provided for adjustment of cyclic stick and thumb-wheel collective command authorities. A galvanometric voltmeter displays flight path angle generated from angle of attack and pitch angle signals.

Flight Engineer's Console

The flight engineer's console, shown in a photograph in Figure 13, contains monitoring and control provisions for most of the model-controller system functions. Included are galvanometric meters for displaying propulsion systems current and voltage, model RPM, automatic RPM control loop error, truck velocity and the three-axis rate gyro outputs. Digital voltmeters are provided to display selectively control commands, model angular rates or model attitudes and heading.

Signal Conditioning, Computation and Recording

All of the signal conditioning and control computational electronics are rack mounted in the cabinet housing the servo power amplifiers. Data signals to be recorded are carried to the data cabinet by an interconnecting cable.

The data recording system, consisting of signal patching boards, oscillograph recorders and magnetic tape recorder was supplied by the sub-contractor and was not developed as part of the model-controller system.

Instrumentation

The instrumentation system includes measurements of model controls, air data, three axis rate gyro information, model RPM and truck speed.

Model Controls

The model control positions are measured by means of the follow-up potentiometers on the wing pitch servo actuators. Since these potentiometers measure the actual blade feathering in the rotating system, they are inconvenient for data reduction purposes and the model collective and cyclic commands in the non-rotating system are also measured and recorded.

Air Data

The air data instrumentation consists of vanes to measure angle of attack and sideslip using low-friction potentiometers and a low airspeed transducer. These instruments are mounted on the end of a 6' boom attached to the gondola as shown in Figure 4.

The aerodynamic vanes shown in Figure 14 have canard surfaces to provide aerodynamic damping. The low airspeed transducer is manufactured by J-Tek Corporation and measures airspeed by the correspondence between the airspeed and the shed frequency of the vortex behind a right circular cylinder perpendicular to the flow.

3-Axis Gyro Package

The model angular rates are measured by means of three mutually orthogonal rate integrating gyros carried in the model gondola. These gyros, obtained from government surplus, are of inertial platform quality and have extremely low drift and hysteresis characteristics. It is therefore possible to integrate their rate outputs to obtain accurate attitude information. The integrations are performed in the ground-based computation and both rate and attitude signals are displayed and recorded.

Truck Velocity

The truck velocity measurements are obtained from a "fifth-wheel" type transducer mounted on the rear of the truck. This system, which was rented for use in the subject experiments, provides a d.c. voltage proportional to truck speed and is recorded and displayed on the

engineer's console.

Other data signals that are measured are model RPM, rotating system azimuth relative to the gondola, model propulsion system voltage and current and a 1 Hz time standard.

EXPERIMENTAL PROGRAM

The experimental test program was conducted in Hangar # 1 at the Lakehurst Naval Air Station, Lakehurst, New Jersey after a complete model checkout in the aircraft hangar at the Forrestal Campus of Princeton University.

The planned test program included measurements of the model trim conditions and control input response time histories through the forward flight envelope of the model. Initial hovering flights indicated, however, significant difficulties in controlling the lightly-damped dynamic mode and all flight testing was confined to hovering flight with a stationary ground base.

Preliminary Hovering Tests

Prior to the data acquisition flight experiments, hovering flight tests were performed to familiarize the pilot and test personnel with the model behavior. These tests were conducted without the gyro package and with the retrograde drive system disengaged; the gondola was positioned in heading by means of light lines connected to a boom attached to the gondola and tended by ground personnel. In this condition, without the gyro package, ballast and power and instrumentation cabling, the model was 3.5 lb buoyant; the umbilical providing power and instrumentation signals, without gyro cables weighed 0.38 lb/ft.

Hovering flights were performed with 12 lb and 25 lb sling loads suspended from the gondola on approximately 10 ft of line and thus the model was approximately neutrally buoyant at the height at which the sling load was engaged. In general, the model was well behaved,

although sluggish in translation due to the low thrust levels, at the lower altitudes where the combination of sling load and supported umbilical weight required thrust levels less than approximately 30 lb. At higher altitudes where the supported umbilical weight was greater, particularly with the heavier sling load, the thrust levels were high enough that the retrograde precessional mode (discussed elsewhere in this report) became unstable and produced serious difficulties in controlling the model motions.

At the higher thrust levels, the model behavior was characterized by a slow growth of the retrograde mode that, with very careful concentration, the pilot could reduce in amplitude by means of discrete pulse control inputs. Eventually the retrograde motion would increase in amplitude again, however, it was difficult during the initial flights to determine if this mode of motion was characteristically unstable or a lightly damped mode forced by inputs from the heading control lines or recirculation. There was also qualitative indication that the severity of the model motions was influenced by initiation of descent. Although the preliminary hover flights were performed without the instrumentation package, photographic coverage was provided. Review of these movie films indicated that during some of these flights, particularly after descent from altitude was initiated, the amplitude of the model pitch and roll motions grew to as much as $\pm 25^\circ$ and combined measures of thrust reduction, pilot control inputs and ground crew action were required to arrest the motions.

The preliminary hover flights were accomplished without serious incident due in a large part to the fact that at lower altitudes, with much of the umbilical weight not model-supported, the thrust was low and the level flight dynamics were probably stable. Also, the umbilical was not supported from the truck tower but went directly to the floor where it was attended by ground crew. In subsequent flights, the umbilical was mounted on the tower. This arrangement contributed to an incident that damaged the model and terminated the test program.

Fully-Instrumented Hover

Following the preliminary hovering flights, the full instrumentation package was installed, the retrograde heading-hold loop checked out and the lines removed from the air data boom previously used for heading control. It appeared that extraneous inputs from these lines were strong contributors to the observed model motions and their removal might well improve the hovering flying qualities.

Owing to the combination of higher ambient air temperature and the addition of the gyro instrumentation package, the model without umbilical, was 12 lbs heavy; the complete umbilical weighed 0.61 lbs/ft.

One hovering flight, of approximately 30 minutes duration, was accomplished with the instrumented model carrying a 12 lb sling load, and with the ground end of the umbilical suspended from the truck tower. The first half of the flight was flown at fairly low altitudes and corresponding thrust levels of approximately 40 lbs. During this portion of the flight the model and all systems were well behaved with the exception that the yaw rate gyro integrator, used to maintain the heading-hold loop, showed

a drift of approximately 2° /min. This drift had not been encountered in the laboratory check out of the system and was apparently caused by the unfavorable environmental conditions at Lakehurst.

The latter half of the flight was flown at higher altitude to permit more maneuvering flight experience. The thrust level for this portion of flight was estimated to be approximately 55 lb at which point the precessional motion began to develop, indicative of a characteristically unstable mode. The recorded data indicate that the retrograde mode grew until it reached an amplitude corresponding to approximately $\pm 2^{\circ}$ of pitch and roll attitude excursion with a period of 11.4 seconds. The period and magnitude of this motion was approximately constant for nearly 5 minutes, indicating a limit-cycle type of dynamic motion. During this time, the integrator drift had increased until almost two-thirds of the available offset command had been used to compensate and maintain a constant gondola heading and the test engineer elected to terminate the flight. Upon initiating the descent, the precessional motion began to increase in amplitude and in six periods had tripled in amplitude at constant frequency. At this time, owing to the large model motions and resulting torque inputs due to sling load and umbilical motions, the heading-hold retrograde loop failed and the back-up rate mode was activated. For approximately 45 seconds the model was operated in this mode although complete control following the transient was never established and the model precessional motion attained amplitudes as high as $\pm 15^{\circ}$ in pitch and roll attitude. At approximately 20 ft of altitude the rate-control

retrograde loop failed, again due to excessive torque inputs, and the model was out of control. Simultaneously, the ground crew hauled the model down by means of the umbilical and the flight engineer began to reduce the RPM. The model rotation had not been arrested by the time the gondola was in the hands of the gound crew and the rotating model struck the end of the umbilical suspended from the truck tower resulting in damage to the model.

EQUATIONS OF MOTION

The linearized equations of motion describing the dynamic motions of the AEROCRANE near hovering flight are developed in this section.

A body axis is used with the origin at the vehicle's center of gravity as shown in Figure 15. The X-axis points forward, the Y-axis to the right and the Z-axis downward. Note that the angular velocity of the centerbody and blades is in a clockwise direction when viewed from the top, i.e., opposite to that of a conventional helicopter. A four-degree-of-freedom model is employed since the linearization assumption will decouple the vertical translation and yawing degrees-of freedom. Thus, the four equations of motion are

$$\begin{aligned} I_o \ddot{\phi} + I_z \Omega \dot{q} &= L_s \\ I_o \ddot{\theta} - I_z \Omega \dot{p} &= M_s \\ m_o \ddot{u} &= X_s \\ m_o \ddot{v} &= Y_s \end{aligned} \tag{1}$$

It is assumed that the center of gravity of the vehicle lies on the shaft. The external forces and moments, denoted in equation (1) by L_s , M_s , X_s , Y_s , arise from the following sources:

- a.) The buoyancy force as a result of the helium filled centerbody.
- b.) The apparent mass effects⁽²⁾, that is, the aerodynamic forces acting on the centerbody as a result of acceleration.
- c.) The aerodynamic force and moments acting on the rotating blades.

d.) Centerbody drag and magnus forces.

e.) Gravity.

The contributions of each of these effects will now be developed. In equilibrium hovering flight the equation expressing the summation of vertical forces is:

$$W - F_B - T_B = 0 \quad (2)$$

If the vehicle is perturbed through a small pitch angle θ , and a small roll angle ϕ , the forces along the body axes arising from the gravity and buoyancy forces are:

$$\begin{aligned}\Delta X_B &= - (W - F_B) \theta \\ \Delta Y_B &= (W - F_B) \phi\end{aligned} \quad (3)$$

The buoyant force will also produce restoring moments. Denoting r_o as the distance the center of gravity of the vehicle is below the center of buoyancy, the moments arising from the buoyant force are:

$$\begin{aligned}\Delta L_B &= - F_B r_o \phi \\ \Delta M_B &= - F_B r_o \theta\end{aligned} \quad (4)$$

The apparent mass effects arise from the fact that a sphere accelerating through a fluid, experiences a force proportional to acceleration⁽²⁾. The constant of proportionality for a sphere is one-half the volume times the density of the fluid through which it is moving, and the force acts at the centroid of the sphere (center of buoyancy) and acts opposite in direction to the acceleration. Since the origin of the axis system is a distance r_o below the center of buoyancy, moments as well as forces are produced. In addition, the acceleration of the center of buoyancy must be expressed in terms of the center of gravity motion. The X and Y components of the

acceleration of the center of buoyancy are:

$$\begin{aligned} a_{x_{cb}} &= \dot{u} - r_o \dot{\phi} \\ a_{y_{cb}} &= \dot{v} + r_o \dot{\phi} \end{aligned} \quad (5)$$

Denoting the apparent mass of the sphere as

$$m_A = \frac{1}{2} \rho \Psi \quad (6)$$

The forces due to the apparent mass effects are:

$$\Delta X_0 = -m_A (\dot{u} - r_o \dot{\phi}) \quad (7)$$

$$\Delta Y_0 = -m_A (\dot{v} + r_o \dot{\phi})$$

These forces act a distance r_o above the center of gravity and therefore give rise to the moments,

$$\Delta L_0 = -r_o m_A (\dot{v} + r_o \dot{\phi}) \quad (8)$$

$$\Delta M_0 = r_o m_A (\dot{u} - r_o \dot{\phi})$$

The center body will experience a drag force and a magnus force as a result of translation. Although these are non-linear terms they will be retained in the analysis since the drag coefficient of the spherical centerbody is large. The forces arising from drag and magnus forces are expressed as follows:

$$\Delta X_0 = -\frac{1}{2} \rho S C_d u |u| - \frac{1}{2} \rho S C_m v |v| \quad (9)$$

$$\Delta Y_0 = -\frac{1}{2} \rho S C_d v |v| + \frac{1}{2} \rho S C_m u |u|$$

There is a lack of data as to the value of the magnus force lift coefficient C_m since the data available in the literature⁽³⁾ generally is concerned with the case in which the ratio of the peripheral velocity to the forward velocity is small. Here, the interest is in the case where the inverse

of this ratio is small. Experimental data for spheres indicate a limiting value of the lift coefficient as the ratio of the peripheral velocity to forward velocity is increased⁽³⁾. Therefore, for large values of the ratio, C_{LH} becomes independent of this ratio and is consequently the form of the dependence assumed above. These terms also produce moments due to the center of gravity, center of buoyancy spacing.

The rotating blades give rise to hub moments and in-plane forces. Analytical expressions for these terms are developed in Appendix A, assuming that the blades are infinitely stiff in flapping. With the exception of the rotor thrust, the equilibrium values of these forces and moments are zero.

The following linearized terms are present:

$$\Delta X = - \left\{ \frac{\partial H_s}{\partial u} u + \frac{\partial H_s}{\partial v} v + \frac{\partial H_s}{\partial p} p + \frac{\partial H_s}{\partial B_{1s}} B_{1s} \right\} \quad (10)$$

$$\Delta Y = \left\{ \frac{\partial Y_s}{\partial u} u + \frac{\partial Y_s}{\partial v} v + \frac{\partial Y_s}{\partial q} q + \frac{\partial Y_s}{\partial A_{1s}} A_{1s} \right\}$$

$$\Delta L = \Delta L_H + r_o \Delta Y_s \quad (11)$$

$$\Delta M = \Delta M_H - r_o \Delta X_s$$

where

$$\Delta L_H = \frac{\partial L_H}{\partial u} u + \frac{\partial L_H}{\partial v} v + \frac{\partial L_H}{\partial p} p + \frac{\partial L_H}{\partial B_{1s}} B_{1s} \quad (12)$$

$$\Delta M_H = \frac{\partial M_H}{\partial u} u + \frac{\partial M_H}{\partial v} v + \frac{\partial M_H}{\partial q} q + \frac{\partial M_H}{\partial A_{1s}} A_{1s} .$$

Owing to the symmetry of the vehicle in hovering it may be noted that the following relationships exist among the various aerodynamic derivatives

arising from the rotor.

$$\frac{\partial M_H}{\partial u} = - \frac{\partial L_H}{\partial v}$$

$$\frac{\partial H_s}{\partial u} = - \frac{\partial Y_s}{\partial v}$$

$$\frac{\partial M_H}{\partial v} = \frac{\partial L_H}{\partial u}$$

$$\frac{\partial H_s}{\partial v} = \frac{\partial Y_s}{\partial u}$$

$$\frac{\partial M_H}{\partial q} = \frac{\partial L_H}{\partial p}$$

$$\frac{\partial H_s}{\partial p} = - \frac{\partial Y_s}{\partial q}$$

$$\frac{\partial M_H}{\partial A_{1s}} = - \frac{\partial L_H}{\partial B_{1s}}$$

$$\frac{\partial H_s}{\partial B_{1s}} = \frac{\partial Y_s}{\partial A_{1s}}$$

As a consequence, in the following, for simplicity we replace the rolling moment derivatives with the pitching moment derivatives and the side force derivatives with the longitudinal force derivatives. The complete equations of motion are obtained by adding the contributions given by equations (3), (4), (7), (8), (9), (10) and (12) to equation (1), to yield

$$\begin{aligned}
 I_o \ddot{\phi} + I_z \Omega q &= - F_o r_o \phi - r_o m_a (\dot{v} + r_o \dot{\phi}) \\
 &+ r_o (- \frac{1}{2} \rho s C_{LH} v |v| + \frac{1}{2} \rho s C_{LH} u |u|) + (\frac{\partial L_H}{\partial u} + r_o \frac{\partial Y_s}{\partial u}) u \\
 &+ (\frac{\partial L_H}{\partial v} + r_o \frac{\partial Y_s}{\partial v}) v + \frac{\partial L_H}{\partial p} p + r_o \frac{\partial Y_s}{\partial q} q + \frac{\partial L_H}{\partial B_{1s}} B_{1s} \\
 &+ r_o \frac{\partial Y_s}{\partial A_{1s}} A_{1s}
 \end{aligned} \tag{14}$$

$$\begin{aligned}
 I_o \dot{\theta} - I_z \Omega p &= - F_a r_o \theta + r_o m_a (\dot{u} - r_o \dot{\theta}) \\
 &- r_o (-\frac{1}{2} \rho S C_0 u|u| - \frac{1}{2} \rho S C_L v|v|) + (\frac{\partial M_H}{\partial u} + r_o \frac{\partial H_0}{\partial u}) u \\
 &+ (\frac{\partial M_H}{\partial v} + r_o \frac{\partial H_0}{\partial v}) v + \frac{\partial M_H}{\partial q} q + r_o \frac{\partial H_0}{\partial p} p + \frac{\partial M_H}{\partial A_{1s}} A_{1s} \\
 &+ r_o \frac{\partial H_0}{\partial B_{1s}} B_{1s}
 \end{aligned}$$

$$\begin{aligned}
 m_o \dot{u} &= - (W - F_a) \theta - m_a (\dot{u} - r_o \dot{\theta}) - \frac{1}{2} \rho S C_0 u|u| \\
 &- \frac{1}{2} \rho S C_L v|v| - \frac{\partial H_0}{\partial v} v - \frac{\partial H_0}{\partial u} u - \frac{\partial H_0}{\partial p} p - \frac{\partial H_0}{\partial B_{1s}} B_{1s}
 \end{aligned}$$

$$\begin{aligned}
 m_o \dot{v} &= (W - F_a) \theta - m_a (\dot{v} + r_o \dot{p}) - \frac{1}{2} \rho S C_0 v|v| \\
 &+ \frac{1}{2} \rho S C_L u|u| + \frac{\partial Y_0}{\partial u} u + \frac{\partial Y_0}{\partial v} v + \frac{\partial Y_0}{\partial q} q + \frac{\partial Y_0}{\partial A_{1s}} A_{1s}
 \end{aligned}$$

Equations (14) are the linearized equations for the hovering dynamics and control of the AEROCRANE. They can be written in a more compact fashion by defining

$$\begin{aligned}
 m' &= m_o + m_a && \text{mass of vehicle including apparent mass} \\
 I' &= I_o + m_a r_o^2 && \text{moment of inertia including apparent mass contribution} \\
 \sigma_c &= \frac{I_z}{I'} \Omega && \text{nutation frequency} \\
 \omega_p^2 &= \frac{F_a r_o}{I'} && \text{pendulous frequency squared}
 \end{aligned}$$

$$\frac{1}{m'} \frac{\partial H_u}{\partial u} \equiv H_u$$

$$\frac{1}{I'} \left(\frac{\partial M_u}{\partial u} + r_o \frac{\partial H_u}{\partial u} \right) \equiv M_u$$

etc. And using the symmetry relationships given by (13), the equations of motion are expressed as:

$$\begin{aligned} \dot{p} + (w_c + M_p) q &= -\omega_p^2 \phi - \frac{r_o m a}{I'} \dot{v} \\ &+ \frac{1}{2} \frac{\rho S r_o}{m'} (-C_D v|v| + C_L M u|u|) + M_v u \\ &- M_u v + M_q p - M_{A_{13}} B_{13} + M_{B_{13}} A_{13} \end{aligned} \quad (15)$$

$$\begin{aligned} \dot{q} - (u_b + M_p) p &= -\omega_p^2 \theta + \frac{r_o m a}{I'} \dot{u} \\ &+ \frac{1}{2} \frac{\rho S r_o}{m'} (C_D u|u| + C_L M v|v|) + M_u u \\ &+ M_v v + M_q q + M_{A_{13}} A_{13} + M_{B_{13}} B_{13} \end{aligned}$$

$$\begin{aligned} \dot{u} &= -\frac{T}{m'} \theta + \frac{m a r_o}{m'} \dot{q} - \frac{1}{2} \rho \frac{S}{m'} (C_D u|u| + C_L M v|v|) \\ &- H_v v - H_u u - H_p p - H_{B_{13}} B_{13} \\ \dot{v} &= \frac{T}{m'} \phi - \frac{m a r_o}{m'} \dot{p} - \frac{1}{2} \rho \frac{S}{m'} (C_D v|v| - C_L M u|u|) \\ &+ H_v u - H_u v - H_p q + H_{B_{13}} A_{13} \end{aligned}$$

These are the complete equations of motion for hover flight. For small angles $\dot{\theta} = q$; $\dot{\phi} = p$. Some of the aerodynamic terms from the rotor were neglected in the analog computer investigations since they are small. This is noted in the section where the aerodynamic forces and moments due to the rotor are developed.

For some complementary analytical studies described in another section, the non-linear terms due to the sphere drag and magnus forces were neglected so that some insight could be obtained into the nature of the dynamics.

For these studies it is possible because of the symmetry of the vehicle, to collapse these four equations into two using complex coordinates⁽⁴⁾.

Define

$$\begin{aligned}\eta &= \theta + i\phi \\ w &= u - iv \\ \delta &= A_{1s} - i B_{1s}\end{aligned}\tag{16}$$

Multiply the first equation by i and add to the second equation.

Multiply the fourth equation by i and subtract it from the third equation. This results in the following equations with the definitions given by (16).

$$\begin{aligned}\ddot{\eta} + (-M_q + i(M_u + M_v))\dot{\eta} + \omega^2\eta - \frac{r_m}{I'}\dot{w} \\ - (M_u + iM_v)w = (M_{A_{1s}} + iM_{B_{1s}})\delta \\ - \left(\frac{m_r}{I'} - H_s i\right)\dot{\eta} - \frac{T}{I'}\dot{\eta} + \dot{w}(H_u + iH_v)w = iH_{B_{1s}}\delta\end{aligned}\tag{16}$$

Equations (16) are quite convenient for analytical studies as they are now of third order rather than sixth order. The fact that this reduction in order can be made implies that the dynamic motions of the vehicle will essentially be circular motions with the radius of the circle either increasing or decreasing with time depending upon the stability. That is, if there is a characteristic root of the system described by (16) which is imaginary, then there will be a solution of the form

$$\eta = c e^{i\Omega_n t}$$

η can be interpreted as a vector rotating at an angular velocity Ω_n ⁽⁴⁾ and thus neutral stability will consist of a circular or whirling motion. Note also that the characteristic equation of this dynamic system expressed in terms of complex coordinates will have coefficients with complex coefficients so that the roots will not in general appear in complex pairs. The sign of the imaginary part of the root will directly indicate whether the circling or whirling mode is in the same direction as the rotor's angular velocity (a negative imaginary part), or is in the opposite direction (a positive imaginary part). The modes are referred to as forward modes if they are in the same direction as the rotation of the rotor and retrograde modes if they are in the opposite direction.

DYNAMIC STABILITY

The stability boundaries in hovering flight are examined in this section using a simplified form of equations (16). It is shown in Appendix A that the in-plane force terms are small and can be neglected in examining the stability boundaries. The influence of the nonlinear drag and magnus force terms on the stability are discussed in the section on analog computer simulation.

Thus neglecting the terms in equations (16) which arise from the rotor in-plane forces, equations (16) become after taking the Laplace Transform and dropping the input terms since only the characteristic modes and stability are of interest,

$$(s^2 + (-M_q + i\omega_e)s + \omega_e^2)\eta + (-\frac{r_0 m}{I'}s - (M_u + iM_v))w = 0 \quad (17)$$
$$(-\frac{m a r_0}{m'}s^2 + \frac{T}{m'})\eta + s w = 0$$

The characteristic equation is

$$(1 - \frac{m a r_0^2}{I'} \frac{m}{m'})s^3 + (-M_q - \frac{m a r_0}{m'}M_u + i(\omega_e - \frac{m a r_0}{m'}M_v))s^2 \quad (18)$$
$$+ (\omega_e^2 + \frac{r_0 m}{I'} \frac{T}{m'})s + \frac{T}{m'}(M_u + iM_v) = 0$$

In order to see the essential features of the dynamic motion all of the terms in which r_0 appears explicitly may be dropped in equation (18). The simplified characteristic equation is therefore

$$s^3 + (-M_q + i\omega_e)s^2 + \omega_e^2s + \frac{T}{m'}(M_u + iM_v) = 0 \quad (19)$$

To obtain some insight into the dynamics of this vehicle first consider some simple cases. If the aerodynamic derivatives are set to zero and the center of gravity is coincident with the center of buoyancy, so that $\omega_p^2 = 0$, the characteristic equation is

$$s^2 (s + i \omega_n) = 0$$

There is one whirling mode given by

$$s = -i \omega_n$$

This corresponds to a forward whirling since it is negative and its frequency is the order of the rotor RPM.

$$\omega_n = \frac{I}{I' z} \Omega$$

since

$$\frac{I}{I' z} = 1.43$$

This frequency is classically referred to as the nutation frequency of a top⁽⁵⁾.

Still with no aerodynamics, but with the center of gravity below the center of buoyancy such that ω_p^2 is non zero, the characteristic equation is

$$s (s^2 + i \omega_n s + \omega_p^2) = 0 \quad (20)$$

The roots of this equation are

$$s_{1,2} = i \left(-\frac{\omega_n}{2} \pm \sqrt{\left(\frac{\omega_n}{2}\right)^2 + \omega_p^2} \right) \quad (21)$$

There are now two natural or whirling modes: a comparatively large negative root; the nutation frequency, and a relatively small positive root corresponding

to a retrograde whirl. This low frequency is classically referred to as the precession frequency. It is usually thought of as a forward whirling in the case of a top since the weight of the top provides the precession torque. Here it is the upward buoyant force which provides the precession torque and therefore the precession is in a backward direction.

For the AEROCRANE dynamic model, in its flight test condition, the two frequencies ω_n , and ω_p , were

$$\omega_n = 4.48 \text{ rad/sec}$$

$$\omega_p = 1.25 \text{ rad/sec}$$

The roots given by expression (21) give a nutation period of 1.3 sec and a precession period of 19.3 sec.

Examining further the characteristic equation given by (19) adding the angular damping M_q the characteristic equation is

$$S^3 + (-M_q + i\omega_n) S^2 + \omega_p^2 S = 0 \quad (22)$$

Now the characteristic roots are damped owing to the presence of aero-dynamic damping. There is a fast well damped motion corresponding to the nutation mode and a slow well damped mode corresponding to the precession mode. The roots corresponding to these various simplified characteristic equations are shown in Figure 16.

To determine the stability boundaries of this dynamic system consider equation (19). For neutral stability a root of this equation must be purely imaginary let $S = \pm i\Omega_N$. Substituting into equation (19), the conditions for neutral stability are

$$\Omega_N^2 = -\frac{T}{m'} \frac{M_u}{M_q} \quad (23)$$

$$\pm \Omega_N^2 - \omega_n \Omega_N^2 \pm \omega_p^2 \Omega_N = +\frac{T}{m'} M_v$$

Thus if the motion is neutrally stable, the frequency is given by

$$\Omega_N = \sqrt{-\frac{T}{m'} \frac{M_u}{M_q}} \quad (24)$$

The upper sign in the second equation corresponds to a neutrally stable retrograde whirling mode and the lower sign corresponds to a neutrally stable advancing mode.

The stability boundaries are shown in Figure 17 for various values of ω_p^2 . It is interesting to note that large values of $\frac{M_u}{M_q}$, give rise to a retrograde mode instability and small values give rise to an advancing mode instability. If the pendulous frequency $\omega_p = 0$ then the dynamic motion is unstable for all values of the aerodynamic derivatives. A physical picture of this motion can be obtained by returning to the equation of motion and determining the mode ratio between the attitude and the translational displacement. Using the simplified form of the force balance equation

$$\frac{T}{m'} \eta + \dot{\omega} = 0 \quad (25)$$

For neutral stability, the angular displacement is

$$\eta = c_\eta e^{i \Omega_N t}$$

The translational displacement is

$$z = c_x e^{i \Omega_N t}$$

and

$$\dot{\omega} = -c_x \Omega_N^2 e^{i \Omega_N t}$$

Substituting and solving for the ratio of c_x to c_η

$$\frac{c_x}{c_\eta} = \frac{T}{m'} \frac{1}{\Omega_N^2} = - \frac{M_q}{M_u}$$

Thus, the mode shape is

$$\tilde{z} = - \frac{M_q}{M_u} \eta$$

Since $\frac{M_q}{M_u}$ is negative, the vehicle is tilted inward towards the center of rotation as shown in the sketch in Figure 18, and rotating about a point above the centerbody which is equal to the total blade radius since the theoretical value of $\frac{M_q}{M_u} = R$. It is also interesting to note that this relationship gives a very simple result for frequency of the motion in the neutrally stable case as

$$\Omega_N = \sqrt{\frac{T}{m' R}} \quad (26)$$

A physical picture of the neutrally stable retrograde motion is shown in Figure 18.

The precession torques causing the retrograde motion arise from the moment of the buoyant force and the coupling derivative M_v acting in the same direction, thus increasing the precession frequency. About the axis perpendicular to the translational motion, the speed stability M_u and M_q produce torques. A perturbation in u results in M_u causing a greater inward roll and thus a larger diameter circle leading to instability. M_q on the other hand is a stabilizing torque tending to reduce the diameter of the circle. Figure 19 shows the physical picture in the advancing mode where the precession is produced by the coupling term M_v acting in an opposite direction to the buoyant torque. Similarly

M_q tends to destabilize the motion by producing an inward roll and consequently a larger circle, while M_u acts in a stabilizing sense. This is the physical explanation of the shape of the stability boundaries discussed above.

A transient response to a longitudinal control step is shown in terms of a plot of pitch attitude and roll attitude in Figure 20. There is an initial well damped rapid response corresponding to the nutation mode and then a slow retrograde circling motion which is slightly unstable for the case shown. The phase of the initial rate response lags the azimuth of the control input direction or direction of initial angular acceleration by about 30° .

The stability boundaries presented in dimensional form in Figure 17 can also be shown in dimensionless form to give a better insight into the manner in which the geometric characteristics of the vehicle, and the operating condition (the thrust coefficient) influence the stability. This curve is shown in Figure 21 along with the variation in the stability derivatives predicted by the theory of Appendix A. It can be seen that in general, given a center of gravity/center of buoyancy spacing there is some value of thrust coefficient (collective pitch) at which the vehicle is unstable. Owing to the nondimensionalization, the rotor RPM does not appear on the axes (C_T is a function of collective pitch only) but only in reducing the dimensionless pendulous frequency. Again it may be seen that at any operating thrust coefficient increasing the RPM will result in instability. For the geometry of the model the relationship between thrust coefficient and $\bar{\omega}$, which produces neutral

stability is shown in Figure 22. For a given vehicle geometry, increasing blade angle moves the operating condition upward into the unstable region and increasing RPM moves the operating condition to the left into the unstable region. Also shown on Figure 22 is the influence of using different combinations of RPM and collective pitch to achieve 54 lbs of thrust indicating that at the thrust level and center of buoyancy/center of gravity spacing of the model, stability cannot be obtained by interchanging collective pitch and RPM.

It generally appears from the results of this section that for any significant thrust level the AEROCRANE will tend to have a mildly unstable retrograde mode of motion in hovering if the configuration is generally geometrically similar to the model constructed in this program. The only real design parameter available to produce inherent stability is the spacing between the center of gravity and the center of buoyancy. Increasing this distance will ultimately result in a stable vehicle as indicated by the curve given in Figure 22. Details of the configuration such as number of blades, coning, chord, etc do not appear to exact a significant influence on the stability.

FEEDBACK EFFECTS

Since the AEROCRANE model was found to be unstable in hovering flight, in this section the influence of rate and attitude feedback are examined. Again the simplified model is used with the solutions of the complete equations examined on the analog computer.

Using the simplified form of the equations of motion given by equations (17) and neglecting the effect of the rotor in-plane force due to control, the transfer function for attitude to control is

$$\frac{\eta}{\delta} = \frac{M_{A_{1s}} S}{S^3 + AS^2 + BS + C} \quad (27)$$

Since in general A, B, and C are complex numbers, the root locus sketches will not be symmetric about the real axis, however, all of the conventional root locus rules still apply. First attitude feedback is considered. In this case

$$\delta = -\bar{K}_A \eta \quad (28)$$

In general \bar{K}_A can be a complex number representing different azimuth phase feedbacks. If \bar{K}_A is a real number, K_A , then the feedback law in real coordinates is

$$A_{1s} = -K_A \theta$$

$$B_{1s} = -K_A \phi$$

which represents equal gain attitude feedback about both axes. As will be shown below the most effective attitude feedback in the sense of damping the transient motion is given by

$$\bar{K}_A = -\frac{K_{4s} e^{45^\circ} i}{\sqrt{2}} \quad (29)$$

In real coordinates, this corresponds to

$$A_{13} = -K_{45}(\theta - \phi) \quad (29a)$$

$$B_{13} = K_{45}(\theta + \phi)$$

The root locus equation giving the modification of the dynamics as a result of attitude feedback is

$$\frac{\bar{K}_A M_{A_{13}} S}{S^3 + AS^2 + BS + C} = 1 \quad (30)$$

Since $M_{A_{13}}$ is positive, a 180° locus shows the effect of attitude feedback. If \bar{K}_A is a complex number then the angle condition is given by

$$\arg K_A + \sum \arg Z - \sum \arg P = 180^\circ \quad (31)$$

since it is conventional on a root locus diagram to measure angles from the poles and subtract angles from zeros, equation (31) may be rewritten as

$$\sum \arg P - \sum \arg Z = \arg K_A - 180^\circ \quad (32)$$

adding 360° to the right hand side

$$\sum \arg P - \sum \arg Z = 180^\circ + \arg \bar{K}_A \quad (33)$$

Thus, if \bar{K}_A is chosen to be given by equation (29) then equation (33) would indicate that a 225° locus is desired. Again the usual root locus rules apply for this or any other angle condition which might be desired. Root locus sketches are shown in Figure 23 for these two angle conditions. It can be seen that the 225° angle condition provides the greatest increase in damping for small gains and looks like a simple and effective

way to eliminate the dynamic instability of the vehicle.

Rate feedback was also examined. In this case the feedback law is

$$\delta = - \bar{K}_r S \eta \quad (34)$$

The root locus equation for determining the influence of this feedback on the dynamic motion is

$$\frac{M_{A_{1s}} \bar{K}_r S^2}{S^3 + AS^2 + BS + C} = -1 \quad (35)$$

As would be expected there is an additional zero at the origin. A real value of \bar{K}_r , with a root locus condition of 180° corresponds to rate feedback with equal gain about each axis. As can be seen in Figure 24, while the retrograde mode is stabilized the advancing mode is destabilized. This is not unexpected in view of the earlier discussion of the physics of the neutrally stable motion where it was noted that the pitch damping, M_q , tended to destabilize the advancing mode. Examining other azimuth phasing for the rate feedbacks indicates that any phase tends to stabilize one of the modes while destabilizing the other. Also shown on the Figure is a cross rate feedback which would act in opposition to the gyroscopic terms (ω_g) and corresponds to a value of

$$\bar{K}_r = K_r e^{270^\circ i}$$

giving in real coordinates

$$A_{1s} = - K_r \dot{\phi}$$

$$B_{1s} = - K_r \dot{\theta}$$

From equation (33) it can be seen that this corresponds to a 90° locus.

The influence of this feedback on the dynamics is also shown in Figure 23.

Thus, while rate feedback is seen to be undesirable, the vehicle can be stabilized in hovering flight with a comparatively simple feedback law given by equation (29a). In the section on analog computer simulation there is further discussion of the effect of this feedback on the dynamic motion.

ANALOG SIMULATION

Prior to the experimental test program, an analog computer simulation of the linearized four-degrees-of-freedom hovering dynamics had been conducted as reported in Reference 6. These simulations indicated the existence of a retrograde precessional mode of motion that was reasonably-well damped. A complete analysis of this motion was not possible, however, due to the lack of certainty with which some of the important aerodynamic derivatives could be predicted. In part, the experimental test program results were intended better to quantify these derivative predictions.

With experimentally measured data from the free flight scale model, it was possible to verify the theoretical predictions of the aerodynamic stability derivatives used in the computer simulation. In particular, as shown in the sections of this report on the analytical prediction of the vehicle dynamics, the period of the precessional motion, at neutral stability for a given thrust-to-mass ratio, is uniquely determined by the ratio of the velocity stability (M_u) and angular damping (M_q). In addition, the non-linear nature of the observed model motions, as evidenced by the limit-cycle behavior, led to the inclusion in the analog simulation of the representation of the centerbody drag aerodynamics by means of an $\gamma \propto u|u|$ relationship. The importance of this drag force representation is not only that it produces a limit cycle behavior in the transient motion but also essentially eliminates the dependence of modal frequency on X_u that was observed using a linearized drag representation in Reference 6.

The final configuration of the analog simulation of the hovering dynamics is shown in the circuit schematic of Figure 25 and the "nominal configuration which was determined to be the best representation of the experimentally-measured model dynamics is characterized by the derivative

values listed in Table B-II. The values listed in Table B-II are determined from the nondimensional values listed in Table B-II and the model geometric and inertial characteristics listed in Table I. In addition to the "nominal" configuration, variations in the important derivatives as well as various feedback stabilization loops were explored and their predominant influences are here summarized.

Nominal Configuration

A time-history of the "nominal" configuration simulated initial transient response is shown in Figure 26. The unstable characteristic motion is the retrograde precessional mode which, when fully developed in the limit cycle, has a period of approximately 12 seconds. This period is approximately 5% longer than the experimentally-measured period of 11.4 seconds and is obtained by using the theoretically-predicted stability derivative values listed in Table B-II. It should be noted that the simulation is representative of the small amplitude motions of the vehicle. The larger amplitude motions observed in the experimental program during descent and after retrograde failure may not be adequately represented by the small perturbation level flight analysis.

The agreement between experiment and theory for the "nominal" configuration is considered to be excellent as shown in Figure 27, and well within the accuracy of the experimental measurements of model thrust and inertial characteristics. The frequency of the simulation motion is time dependent until the limit cycle is fully developed and the amplitude of the simulation limit-cycle is dependent upon the character of the input but in general is

larger in amplitude than that observed experimentally except in the descent portion of the flight. With the exception of drag coefficient, adjustment of the simulation parameters to shorten the period of the retrograde oscillation for exact agreement with experiment tends always to increase the amplitude of the simulation limit-cycle. Owing to the uncertainty of the theoretical representation of the drag forces and the rather large adjustment of drag coefficient required for simulation matching of both period and limit-cycle amplitude it was considered possibly misleading to employ the drag coefficient as a model matching parameter.

Velocity Stability and Angular Damping

The velocity stability and angular damping derivatives were varied simultaneously, maintaining a constant ratio of the two, from one-half their nominal values to twice their nominal values. Over this range only small changes in modal period (approximately $\pm 4\%$) and negligible changes in small-amplitude-motion damping were observed, correlating with the simplified theoretical prediction. This is one of the most important results of the analog simulation in that the ratio of these two derivatives is strongly dependent upon the "blow-back" effect for which only limited experimental data exist. The result that the modal period of the experimentally-observed model motions can be approximately matched in the simulation only with a unique combination of those two derivatives implies a strong corroboration of the empirically determined magnitude of the "blow-back" effect.

Increasing the velocity stability derivative alone or decreasing the

angular damping derivative alone produces a predictable change in the period of the oscillatory motion and decreases the modal damping for small amplitudes in a similar fashion. The amplitude of the simulation limit-cycle is also increased by either of these derivative changes in the direction described.

Drag Coefficient

The non-linear representation of the sphere aerodynamic drag is responsible for the limit-cycle behavior of the analog simulation. For the "nominal" configuration an advance-ratio-independent value of $C_D = 0.6$ was assumed, which corresponds to those data available and discussed in Reference 3. Increasing the simulation value of C_D tends to decrease the oscillatory mode period slightly while also decreasing the amplitude of the simulation limit-cycle for a constant input. The amplitude of the limit-cycle, for a constant step cyclic input, was found to be approximately proportional to the C_D value assumed.

Feedback Stabilization

Various types of feedback stabilization were examined in the analog simulation and all had predictable influences on the characteristic motion of the simulated model. As discussed in the analytical section of this report, the stabilization loop that appears to have a favorable influence on all the important dynamic characteristics employs a crossed-attitude feedback as given by the expressions

$$A_{10} = K_A (\phi - \theta)$$

and

$$B_{10} = K_A (\phi + \theta)$$

Physically, this loop closure provides attitude stabilization phased to lead the characteristic retrograde oscillatory motions by a 45° phase shift.

Various magnitudes of the feedback gains, K_A , were examined in the simulation study and it was determined that a value of $K_A = 0.2\%$ would critically damp the retrograde oscillatory mode and a value of $K_A = 0.1\%$ significantly improved the pilot's ability to operate the simulated vehicle in hover. A time history of the simulated model motion for $K_A = 0.1\%$ is presented in Figure 28.

Piloted Simulation

An analog simulation was set up to accept inputs from the pilot's control console used to operate the model in the experimental flight test program. Various displays were examined from the standpoint of qualifying the fidelity of the analog simulation and determining requirements for piloting of the model. For the case of the unstabilized model it was determined that if the two model attitudes were displayed on a X - Y plotter the pilot felt that the simulation fairly well represented the model's flight characteristics and could be flown in hover with a high level of pilot attention and activity. Any lesser display, such as translational velocity and/or position was virtually uncontrollable. Addition of attitude rate displays, by means of analog meters, to the X - Y plotter attitude display, eased the piloting task somewhat.

With the crossed-attitude feedback stability augmentation, particularly at the critically-damped condition given by $K_A = 0.2\%$ it was possible for the pilot to operate the vehicle in hover using the translational position

display only. Performance of the task of translating from one position to another was considerably improved in this part of the simulation by phasing the pilot's primary controls, A_{1s} , and B_{1s} , so that the intermediate time (2 to 10 seconds) model translational response was in the direction of the pilot's stick inputs. A control input law given by

$$A_{1s} = A_{1p} + .5 B_{1p}$$

and

$$B_{1s} = B_{1p} - .5 A_{1p}$$

which represents a phasing angle of 26^0 , was determined to be quite acceptable to the pilot in performing the station keeping and changing task using translational position information only. As might be expected from control theory, if the pilot attempts to control the transient oscillation of the model (when it is not critically damped) using translational position information only he tends to destabilize the motion. At least in the simulation, particularly at $K_A = 0.2\%$ where the oscillation is nearly critically damped, no difficulties were experienced if the pilot attention was restricted to the longer-term motions.

CONCLUSIONS

Based upon the experimental and analytical results reported herein the following conclusions are determined:

- 1.) An operating model and control system has been developed,
- 2.) The dominant mode of motion of the AEROCRANE in hovering flight at any significant thrust level consists of mildly unstable retrograde precessional motion,
- 3.) Operator on ground encountered difficulty flying slightly unstable vehicle owing to the lack of motion cues,
- 4.) Analytical predictions of the model stability derivatives, when combined with the measured model inertial characteristics, can be used to simulate accurately the model motions,
- 5.) The good agreement between experimental observation and theory demonstrated in the analog simulation corroborates both the equation of motion representation and the stability derivative predictions,
- 6.) A comparatively simple feedback system utilizing crossed-attitude feedback can be employed to stabilize the simulator study and provide for easy pilot control of the model's position in hovering flight, and
- 7.) A fully buoyant model would have provided a desirable safety feature.

RECOMMENDATIONS

- 1.) An analytical model of the forward flight dynamics of the AEROCRANE should be developed and the dynamic response in forward flight examined prior to proceeding with forward flight experiments.
- 2.) For further hovering experiments an attitude feedback loop should be incorporated in the model.

REFERENCES

1. Perkins, R. G. and Doolittle, D.: "AEROCRANE - A Hybrid LTA Aircraft for Aerial Crane Applications". Proceedings of the Interagency Workshop on Lighter Than Air Vehicles, Monterey, California, September 1974.
2. Kochin, N. E., Kibel, I. a. and Roze, N. W.: "Theoretical Hydro-mechanics", Interscience 1964.
3. Goldstein, S.: Modern Developments in Fluid Dynamics, Vol. II.
4. Curtiss, H. C.: "Complex Coordinates in Near Hovering Rotor Dynamics", Journal of Aircraft, Vol. 10, No. 5, May 1973.
5. Goldstein, H.: Classical Mechanics, Addison-Wesley 1957.
6. Bowers, F. J., III: "Hovering Dynamics and Steady-State Forward Flight Characteristics of the AEROCRANE Hybrid Heavy Lift Vehicle", Princeton University Department of Aerospace and Mechanical Sciences Report 1275-T, May 1976.
7. Coleman, F. P., et. al.: "Evaluation of the Induced Velocity Field of an Idealized Helicopter Rotor", NACA Wartime Report ARR No. 15E10, June 1945.
8. Harris, F. D.: "Articulated Rotor Blade Flapping Motion at Low Advance Ratio", Journal of the American Helicopter Society, Vol. 17, No. 1, January 1972.
9. Vertol Division of the Boeing Company: "Experimental Programs Conducted Under the U. S. Army Cast Loan Agreement, Vol. I Static Tests on a Full Scale Boeing-Vertol 76 Rigid Propeller." Report No. R-339, June 1965.
10. Gessow, A. and Myers, G. C.: Aerodynamics of the Helicopter. The MacMillan Company, New York, 1952.
11. Miller, R. H.: "Rotor Blade Harmonic Air Loading", IAS Paper No. 62-82, Presented at IAS 30th Annual Meeting, New York, N. Y., January 22-24, 1962.
12. Payne, H. E., III: "Propeller Effects on Stability and Control of VTOL Aircraft", Aerospace Engineering, Vol. 19, No. 3, March 1960.

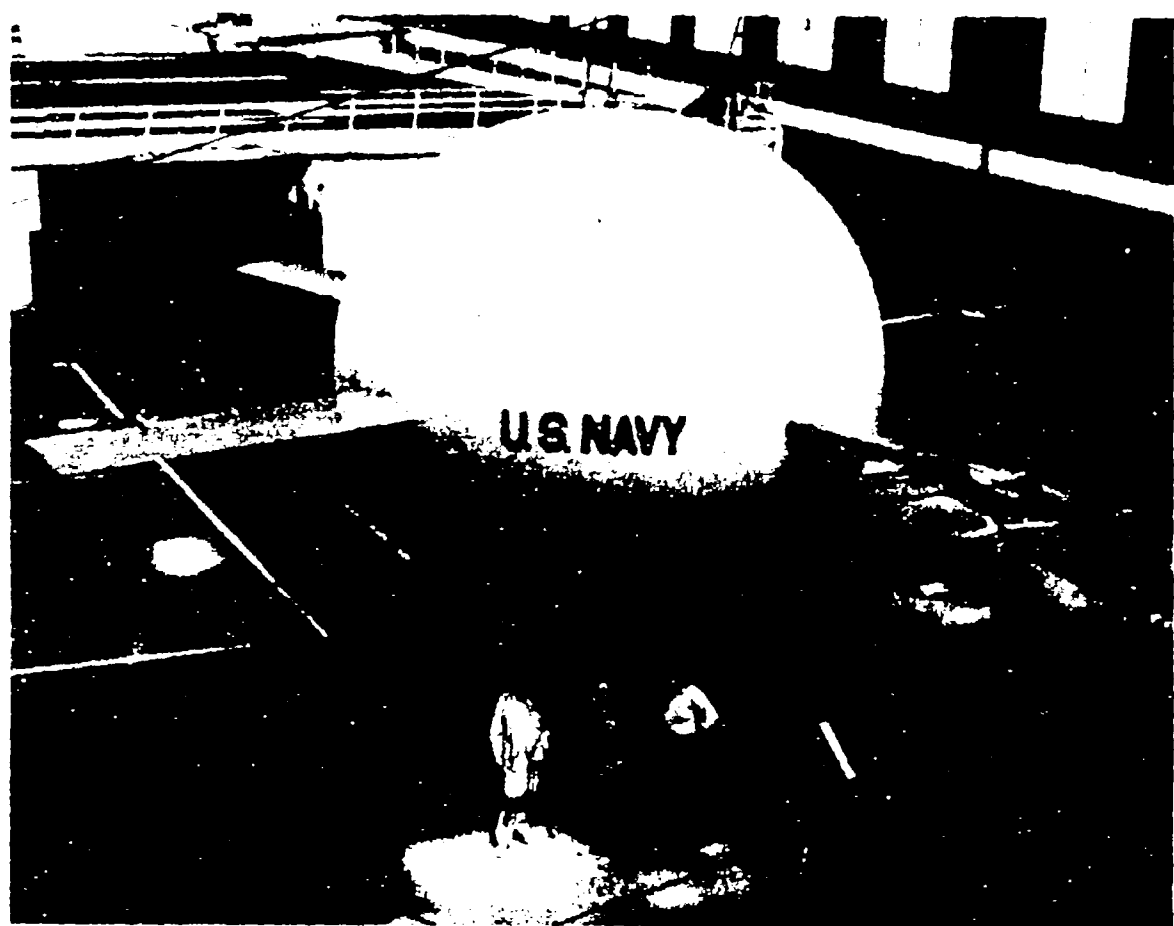


Figure 1. Overall View of Dynamic Model.

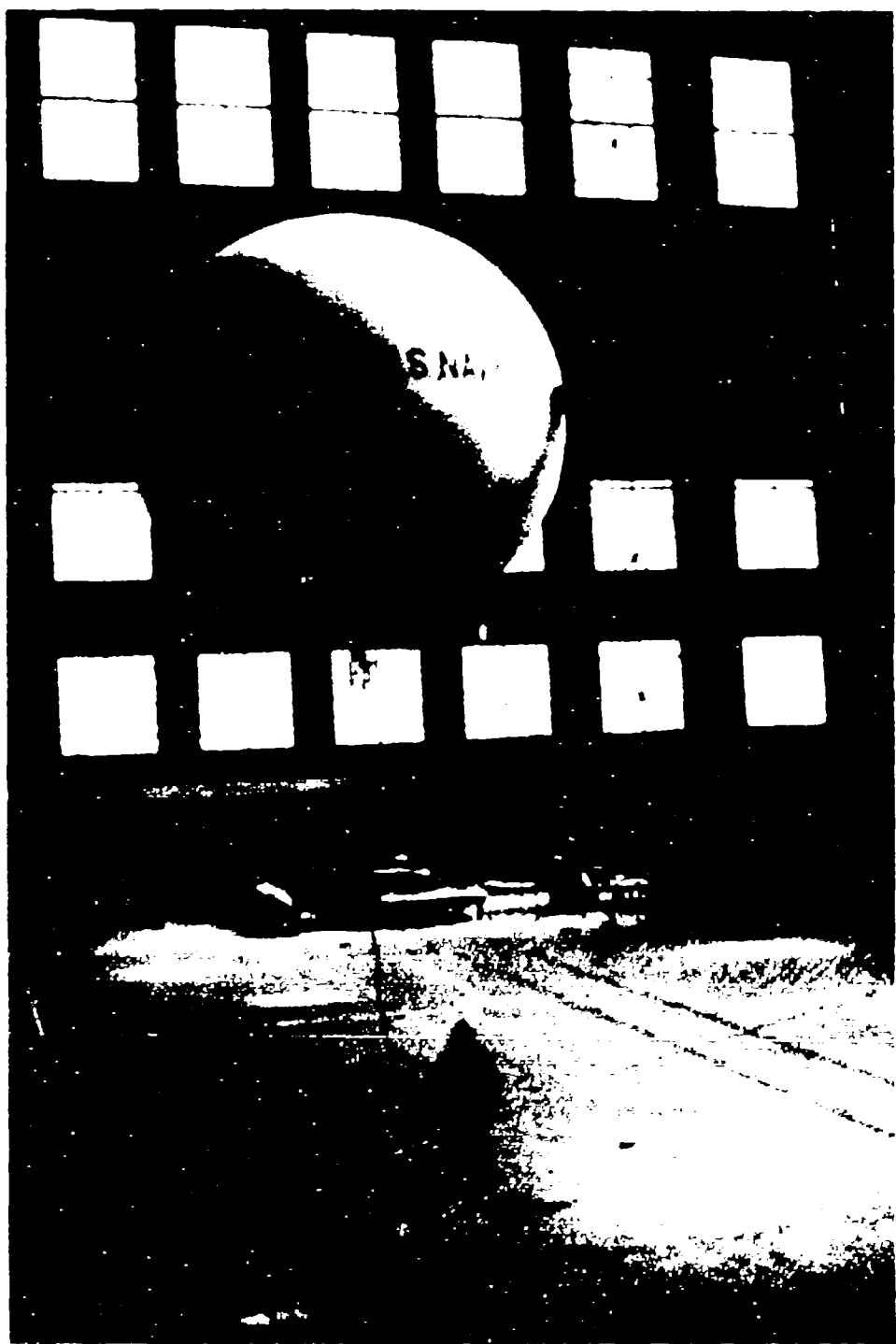


Figure 2. Dynamic Model in Hovering Flight.

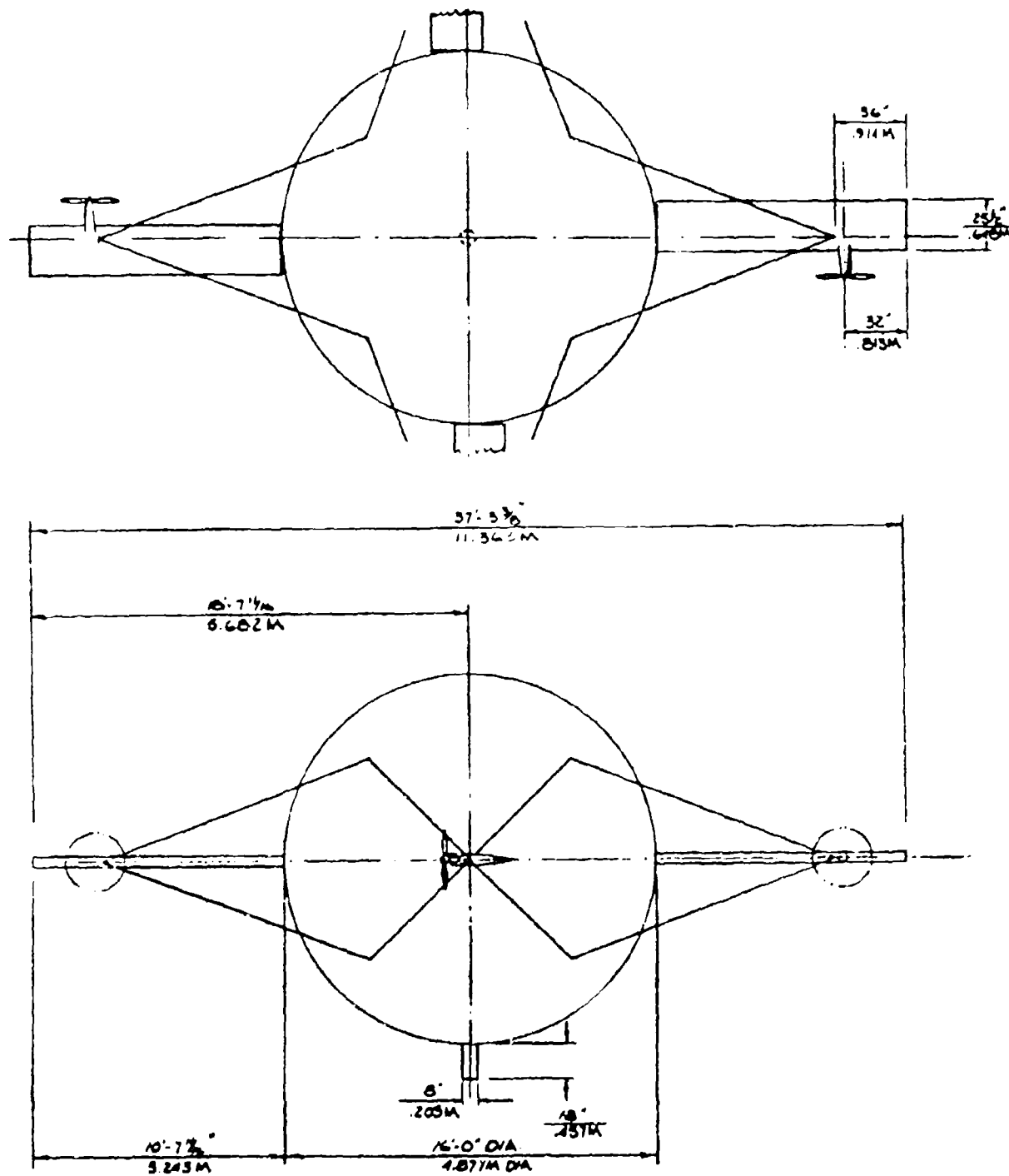


Figure 3. General Arrangement Drawing of Model

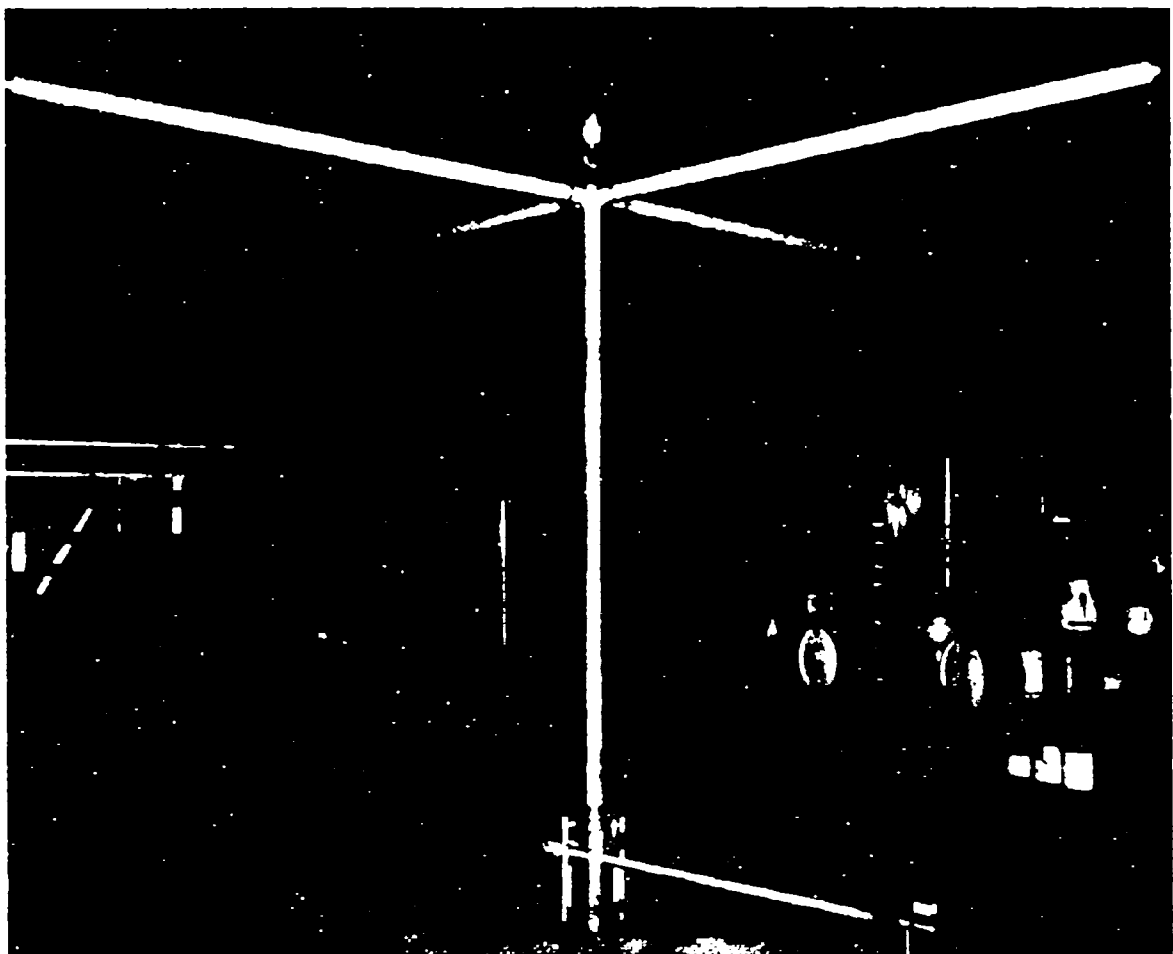


FIGURE 3. Internal Assembly Structure.



Figure 5. Rotating Wings of Model.

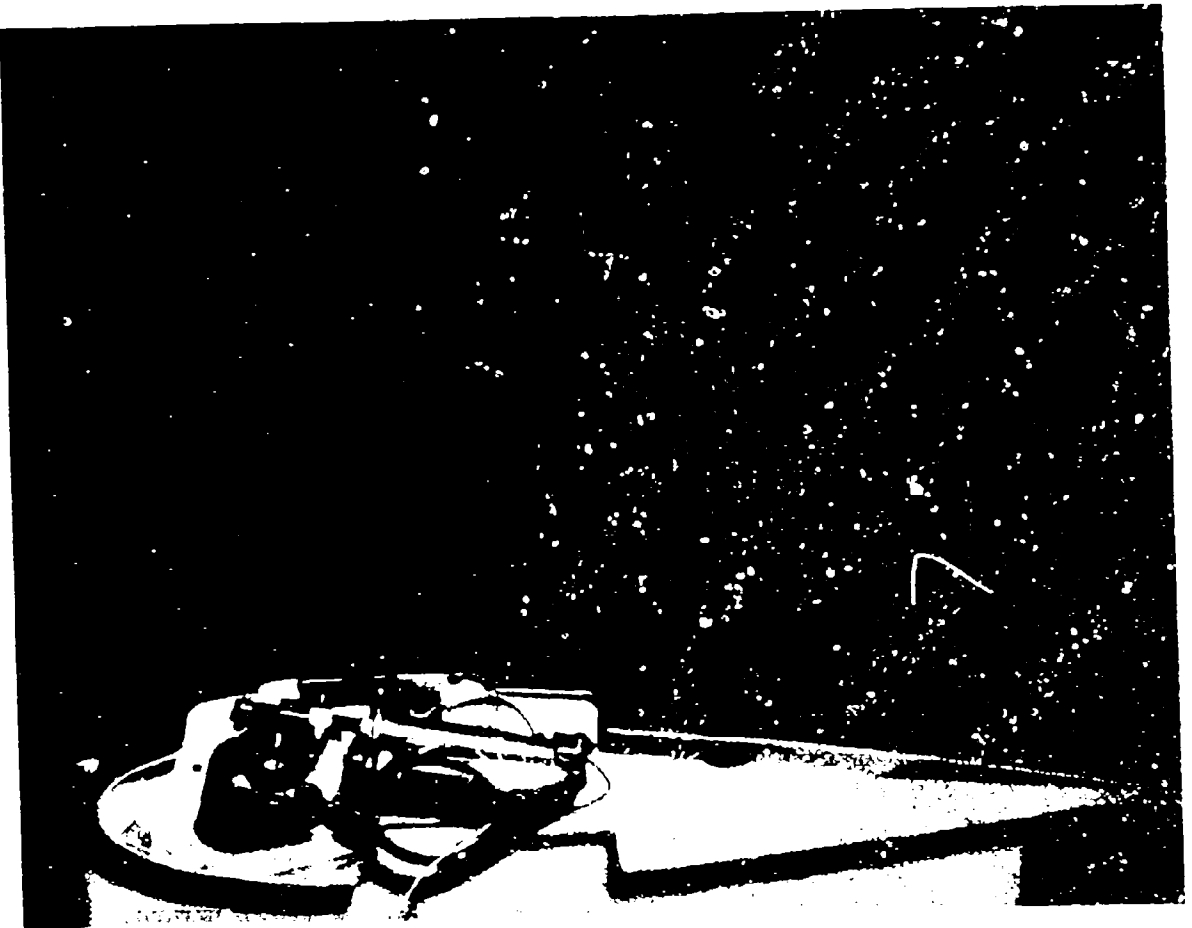


Figure 6. Rotating ring boot assembly.

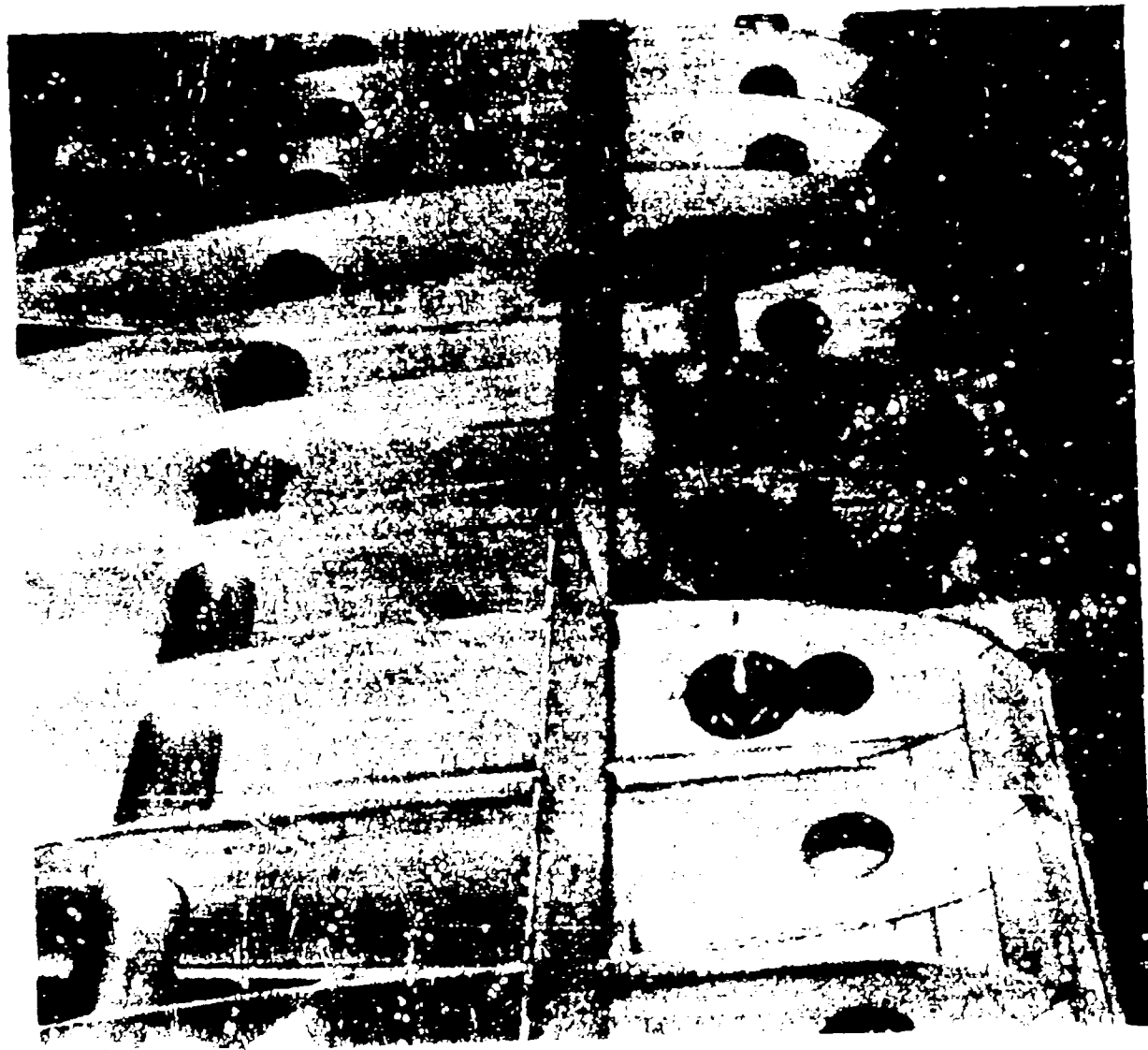


Figure 7. Rotating Wing Tip Assembly and Nacelle.

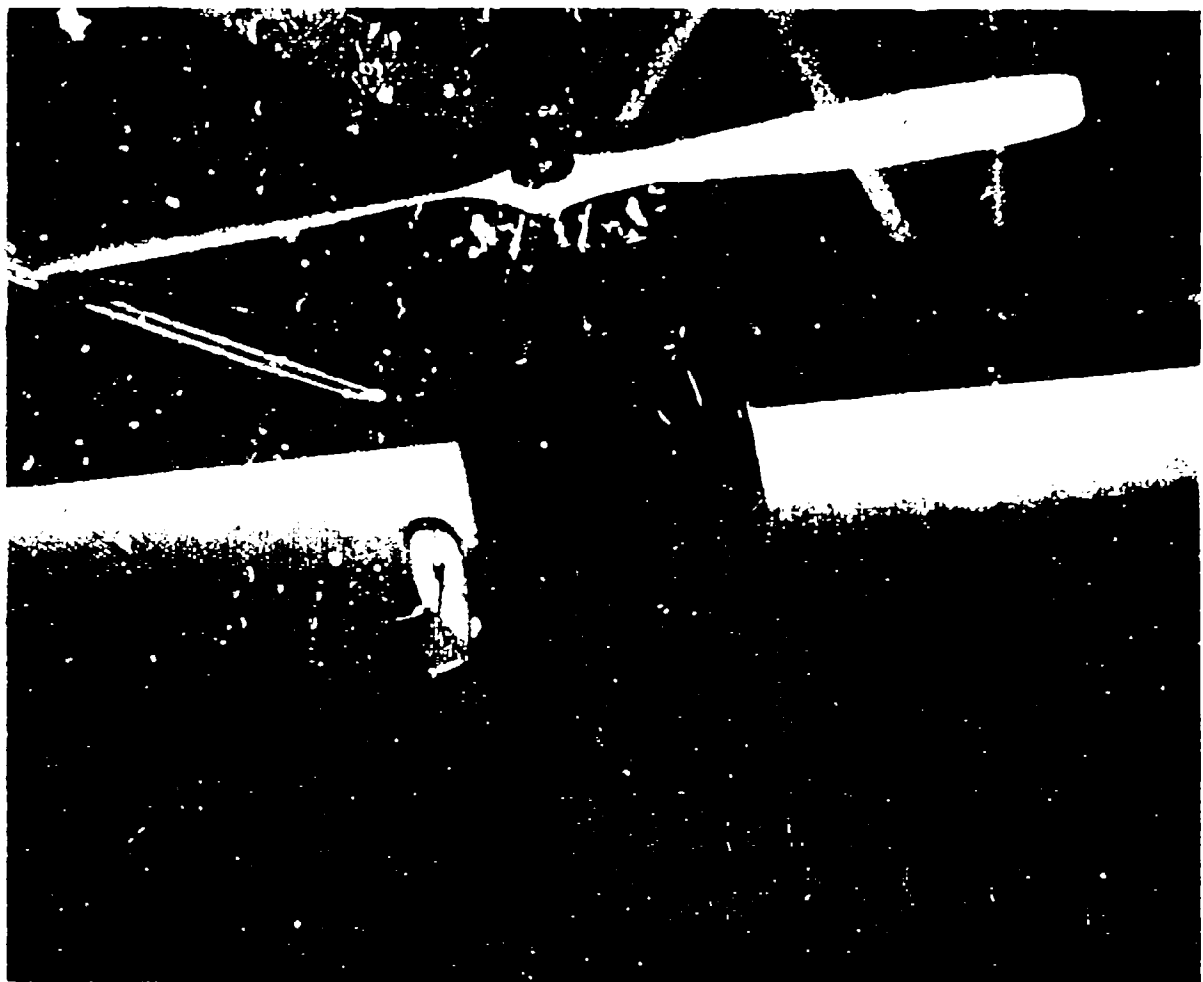


Figure 2. Propulsion System Assembly.

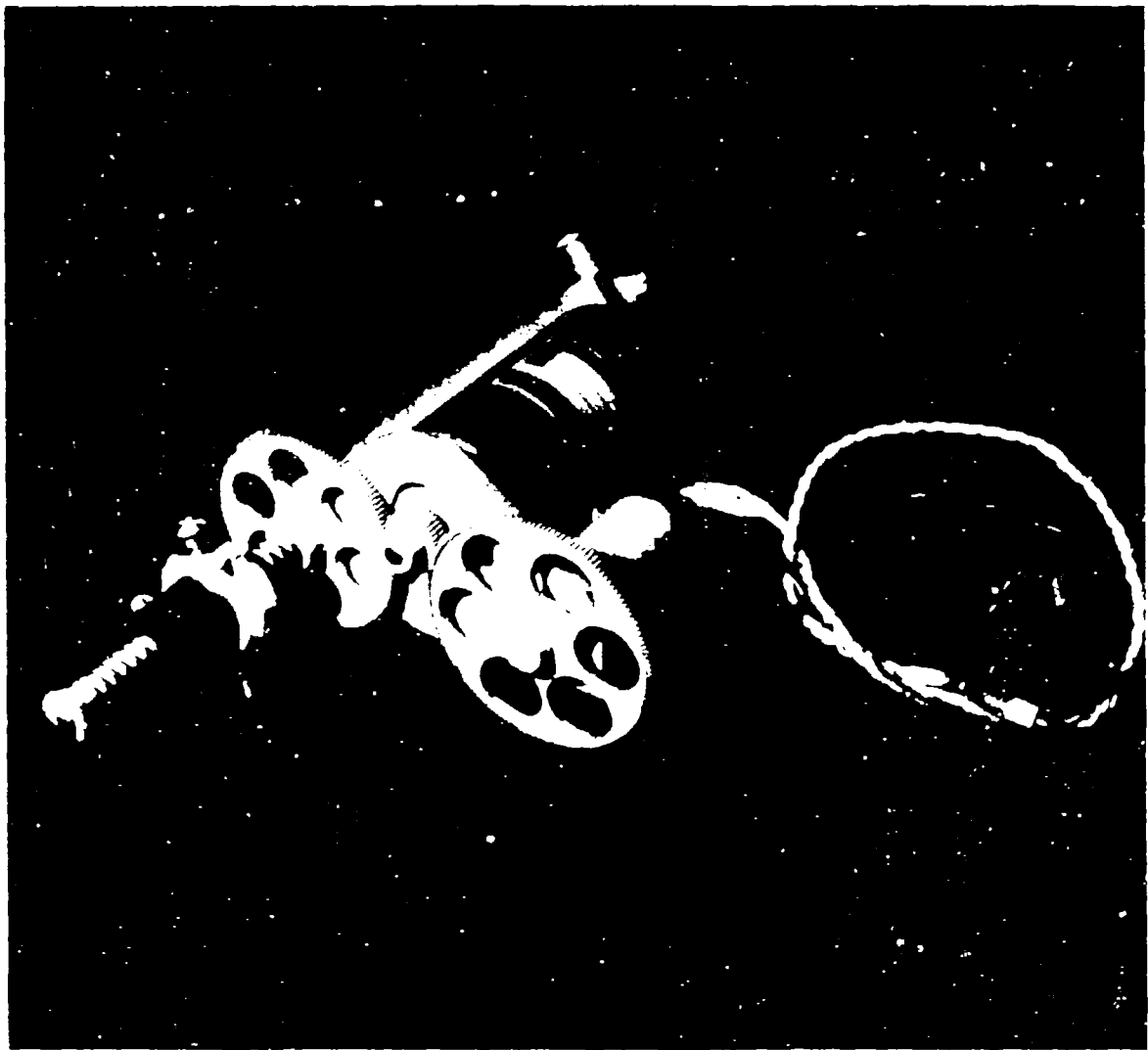


Figure 1. Starting Wind Vane - cutaway assembly.

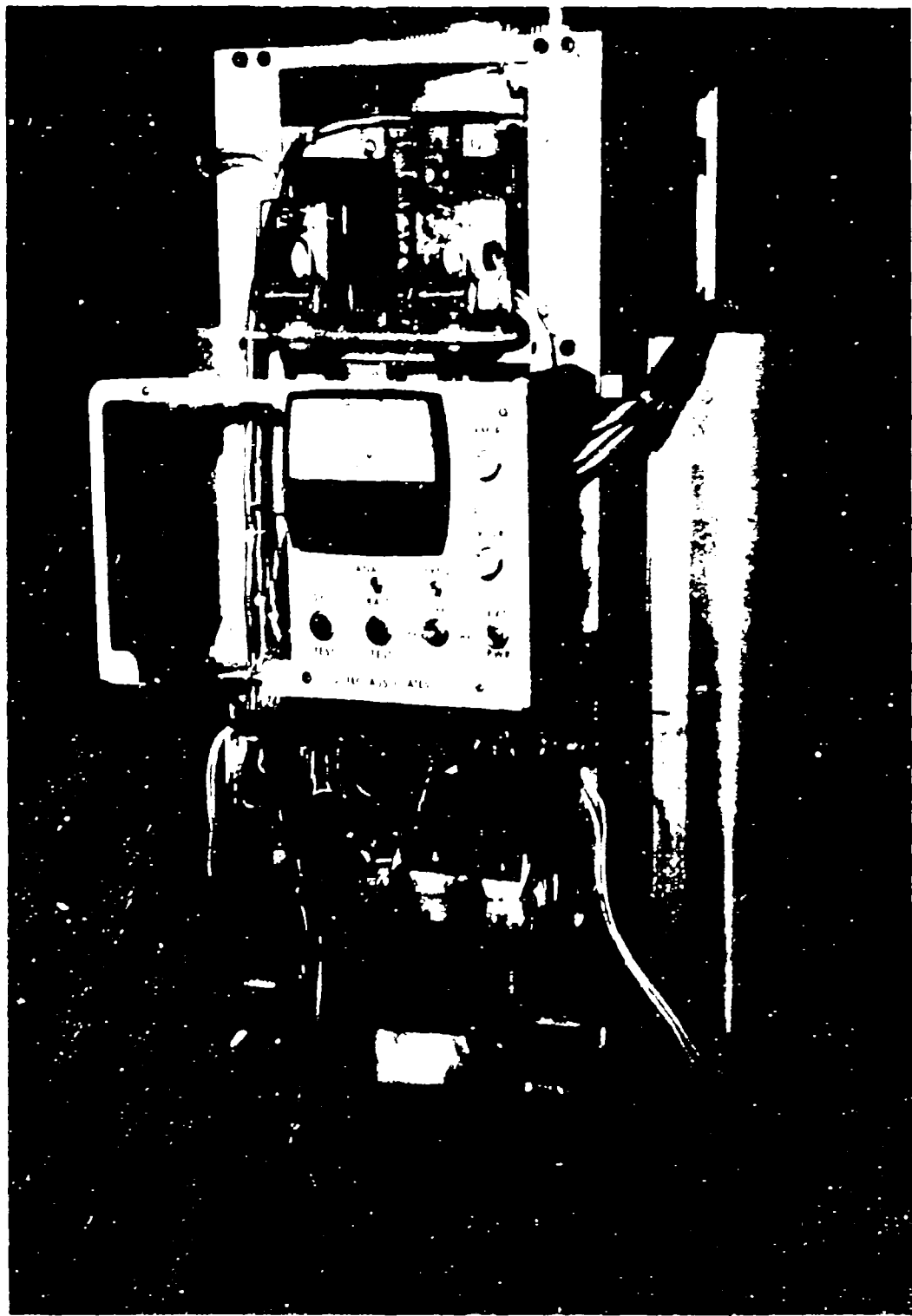


Figure 10. Ionics Assembly.

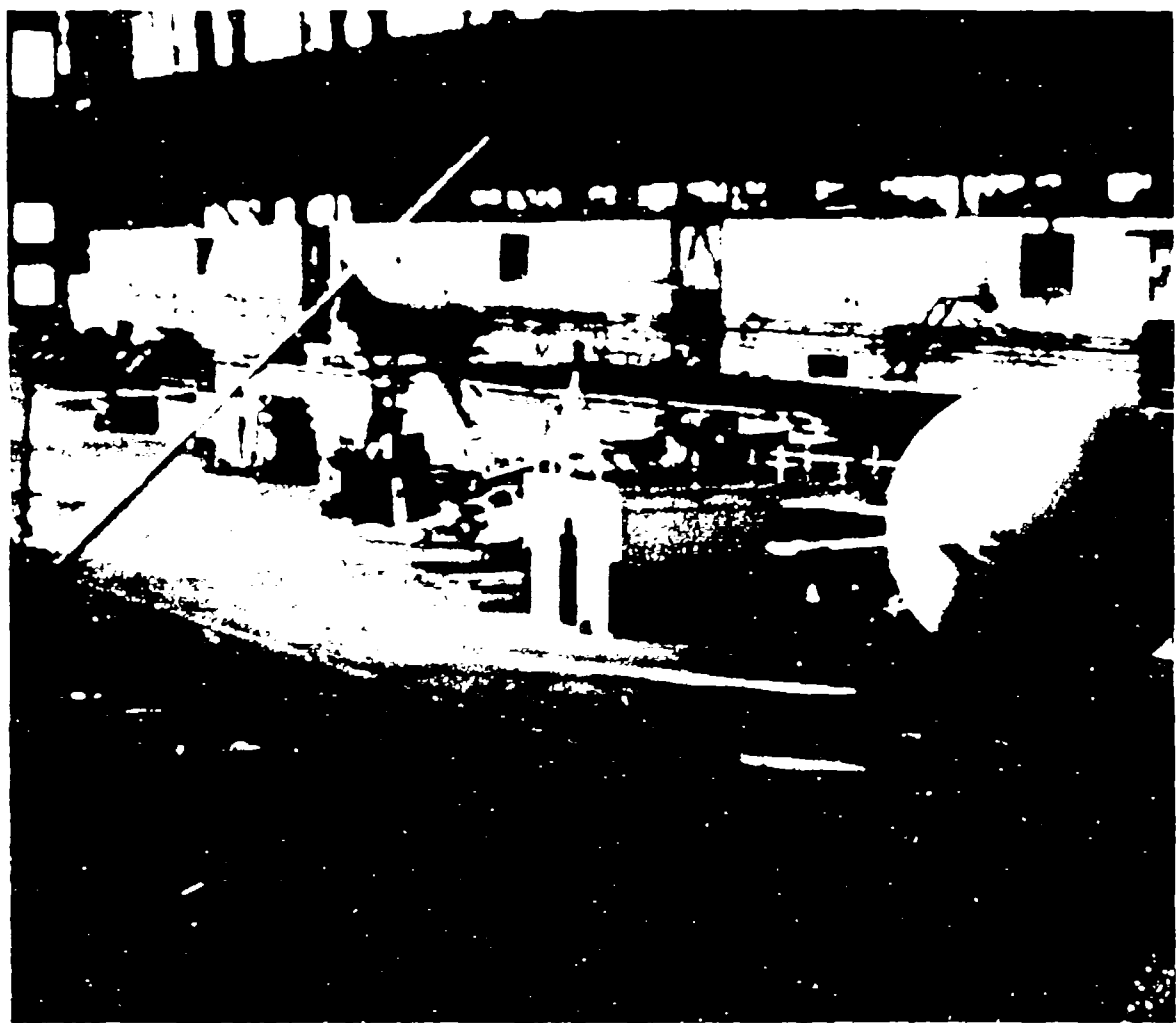


Figure 11. Umbilical Support Room.

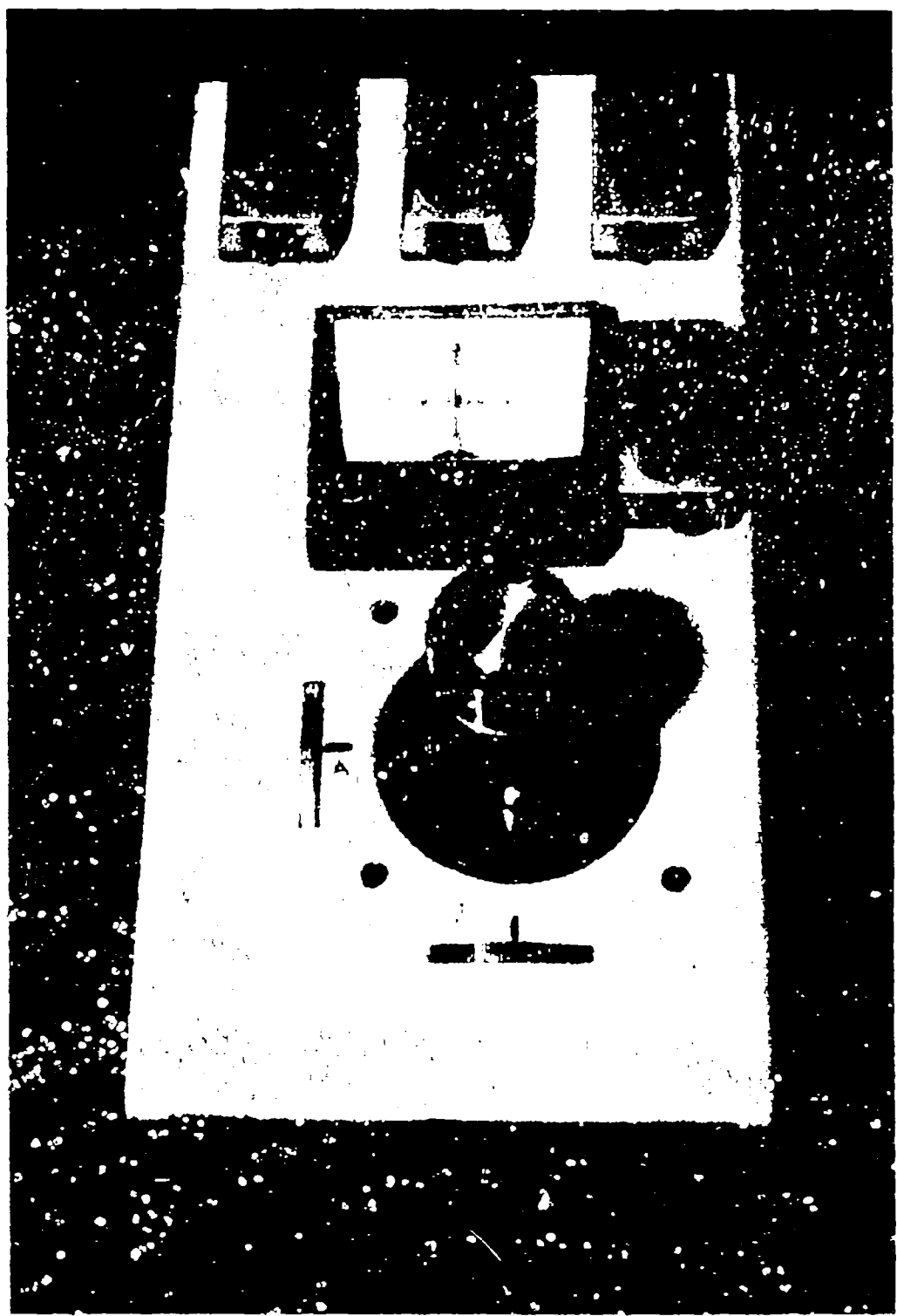


Figure 12. Pilot's Control Console.

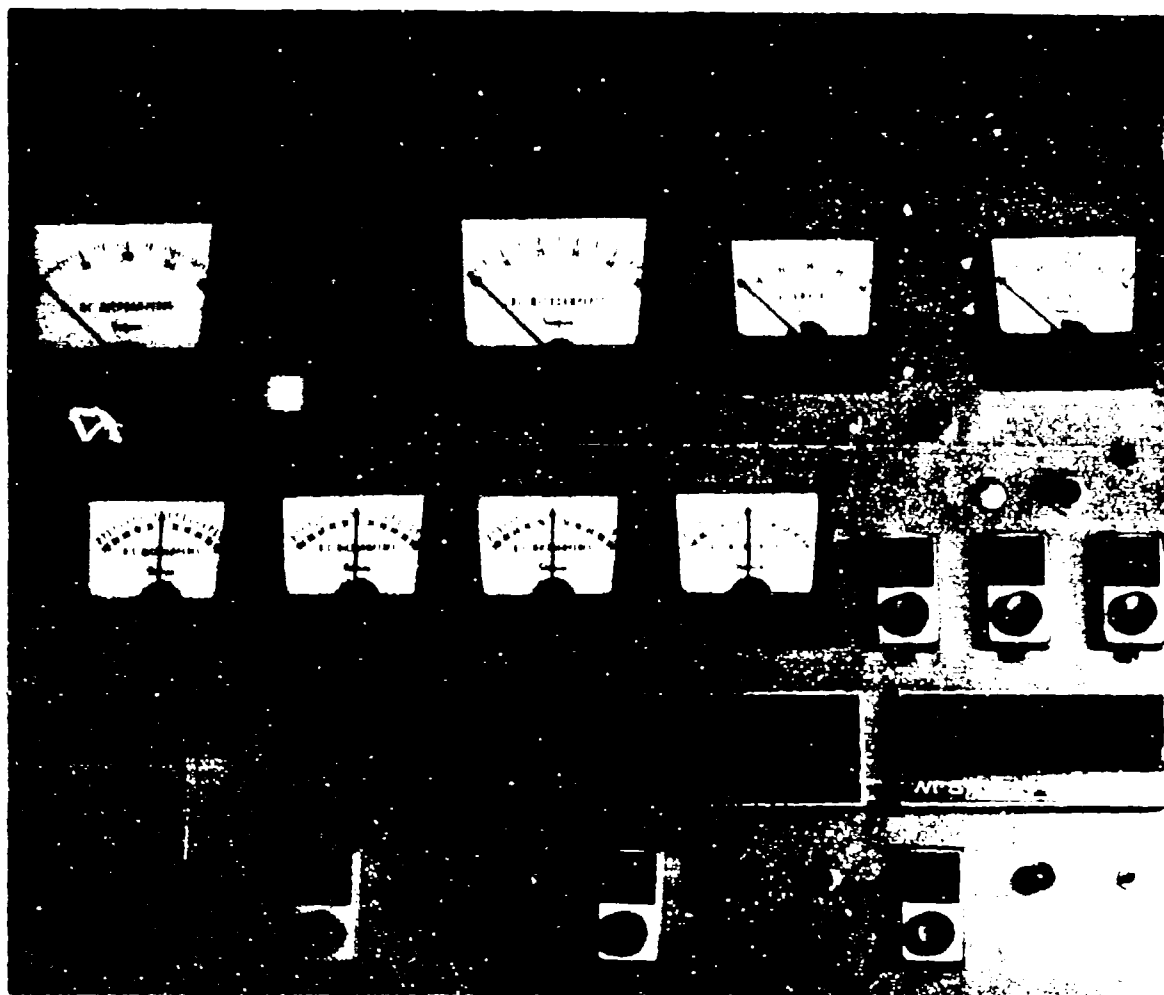


Figure 13. Engineer's Control Console.

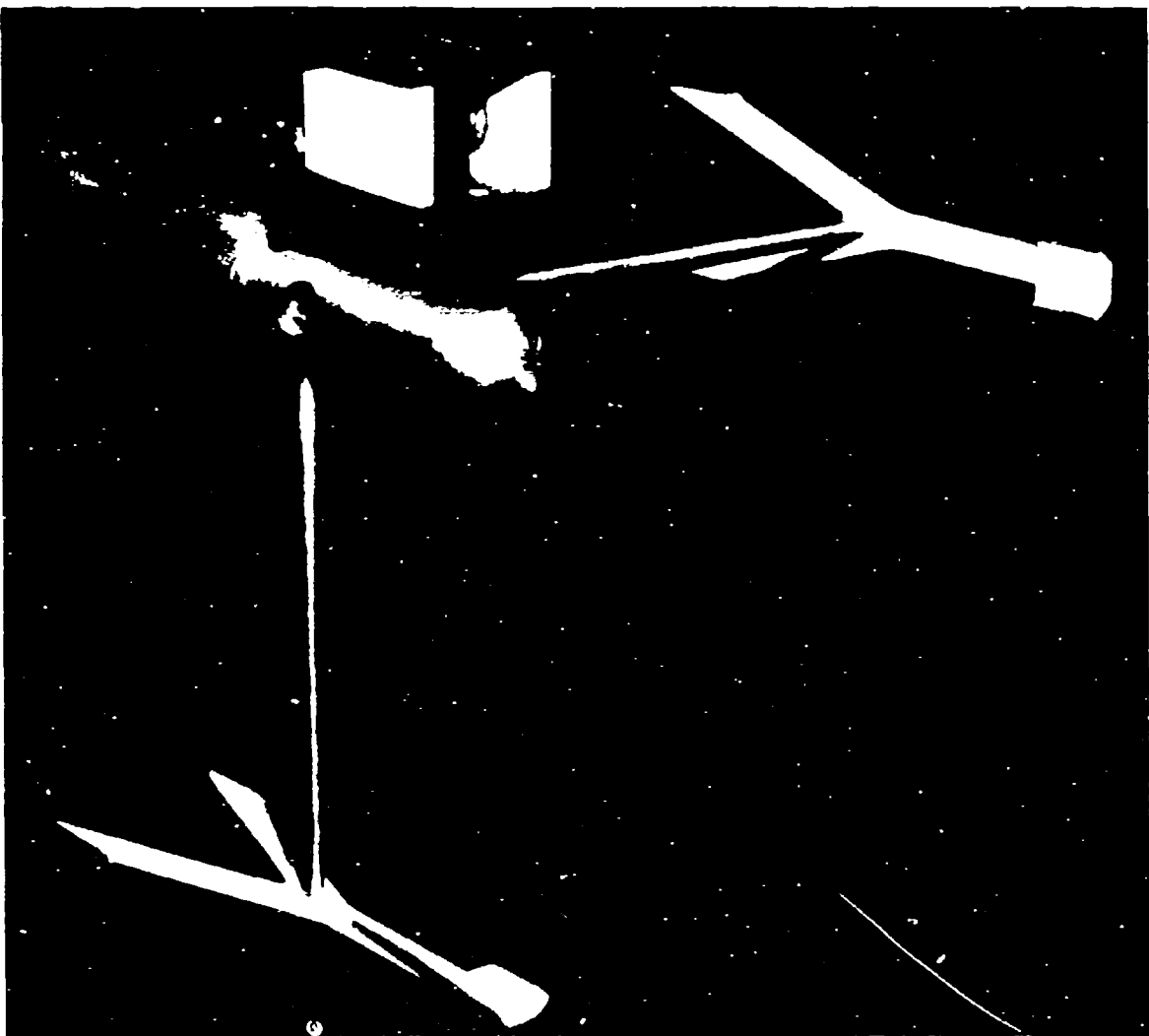


Figure 1^b. - mode of attachment of petiole bases.

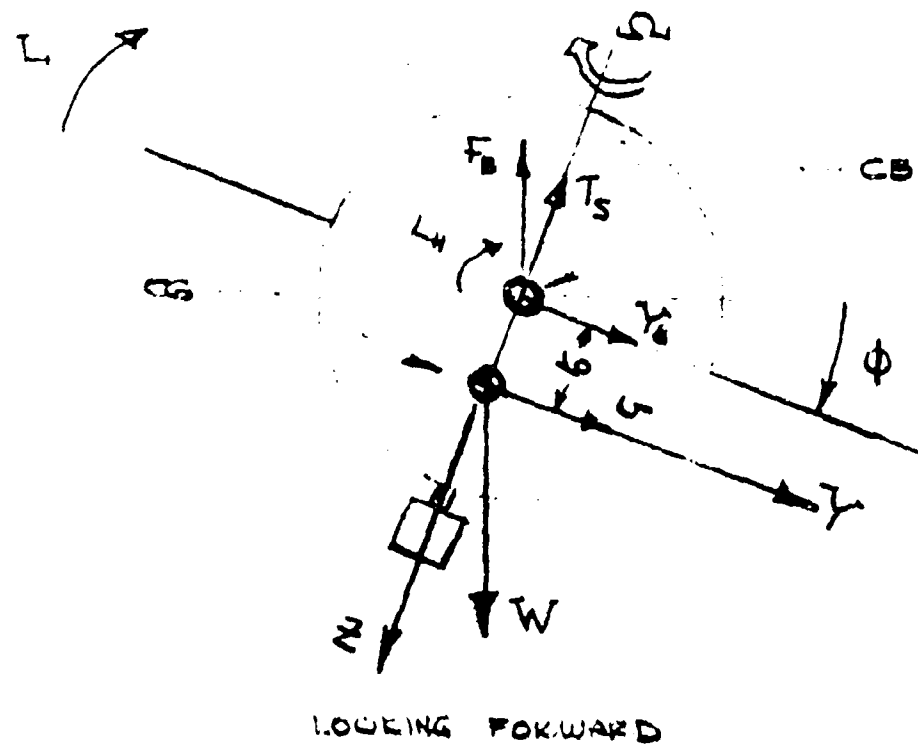
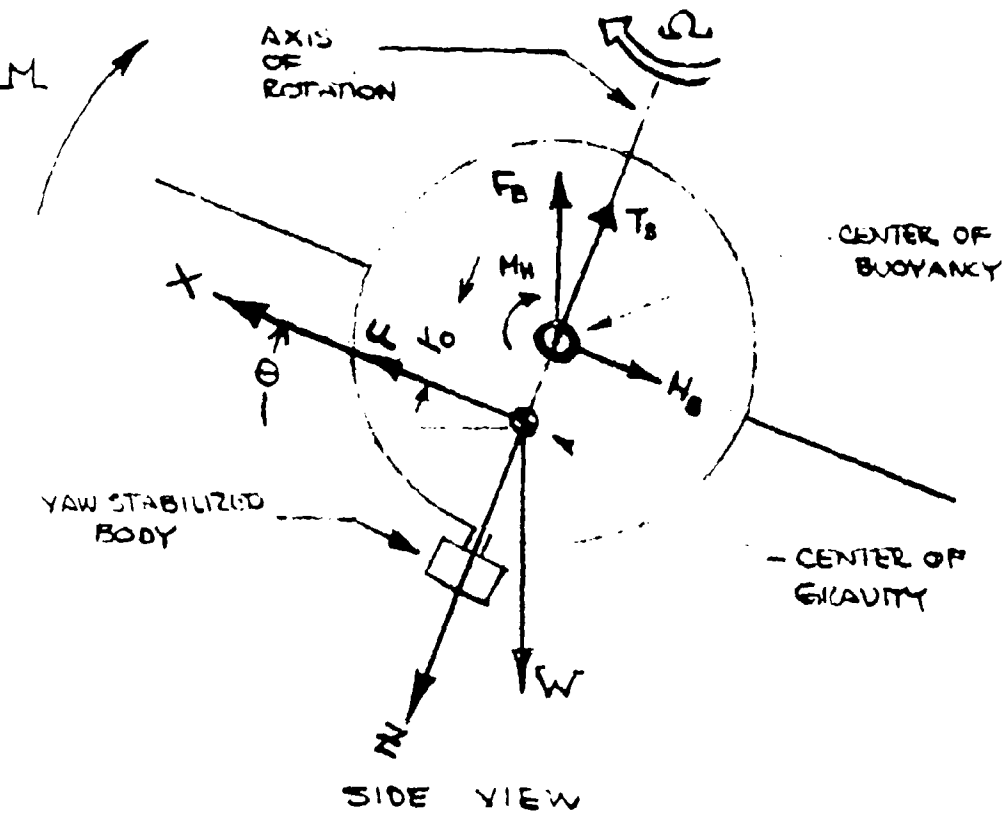


Figure 15. Axis System and Nomenclature.

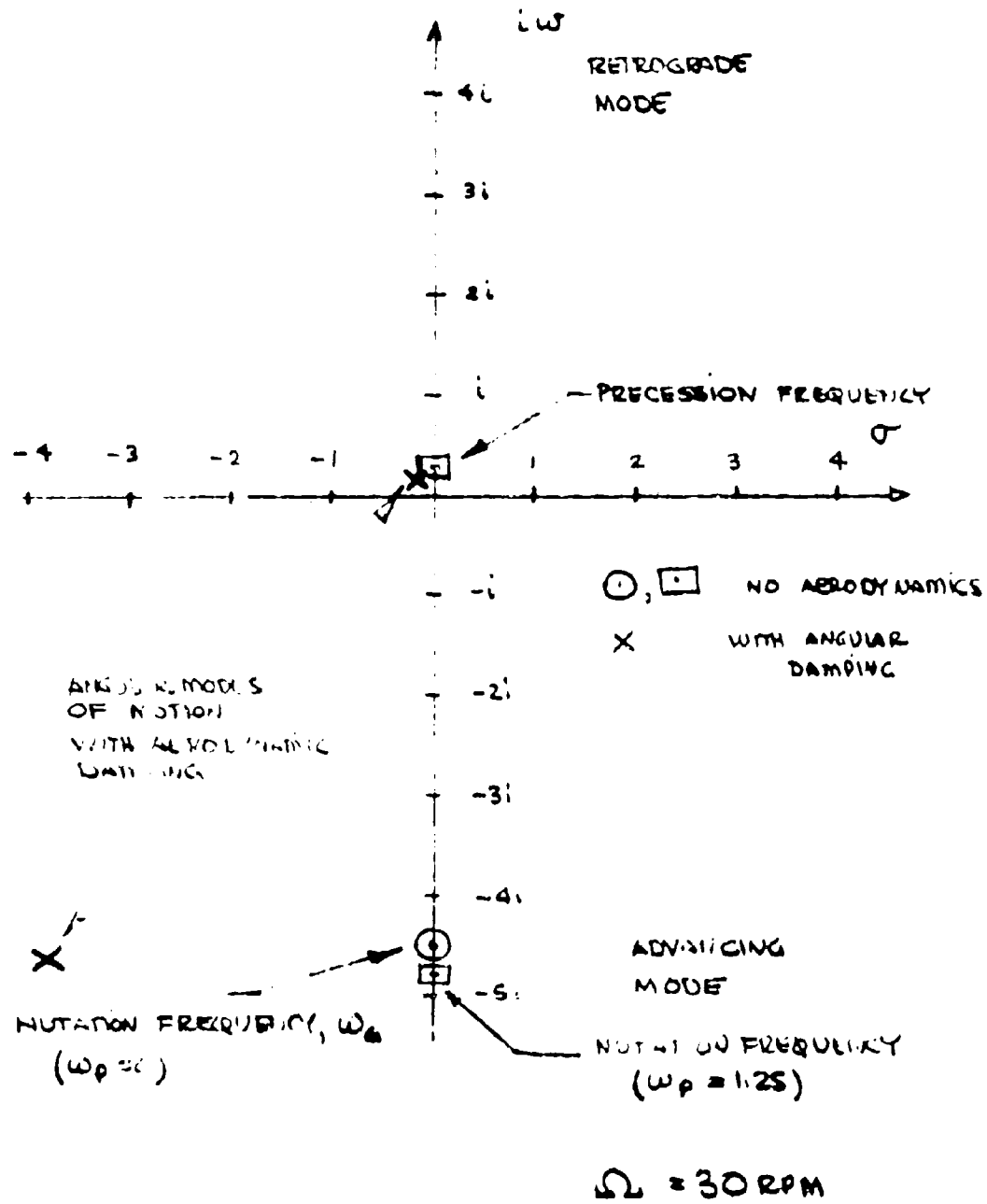


Figure 16. Angular Dynamic Modes of Motion of AEROCRANE.

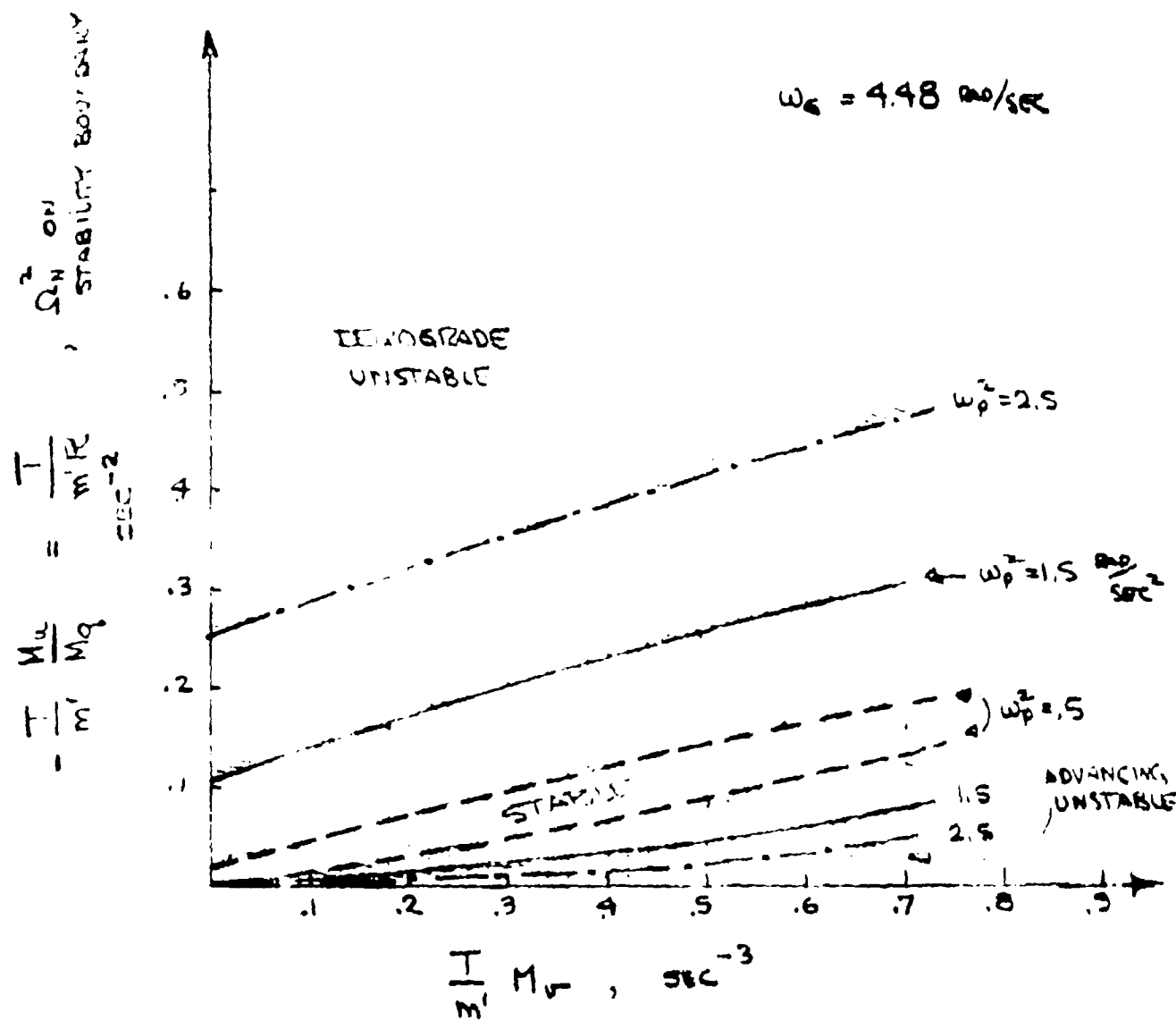


Figure 17. Stability Boundaries as a Function of Pendulous Mode Frequency.

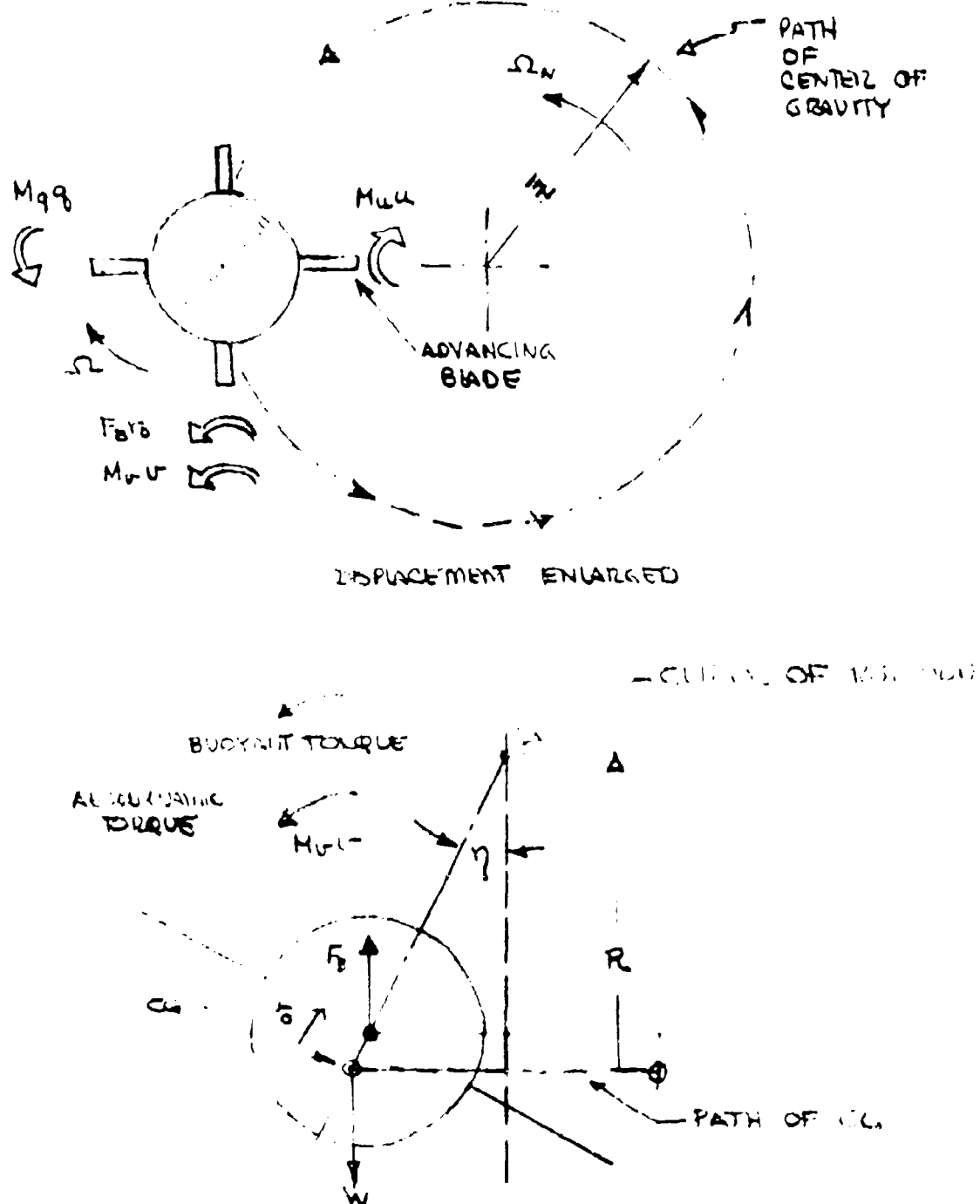


Figure 18. Physical Picture of Retrograde Mode Motion.

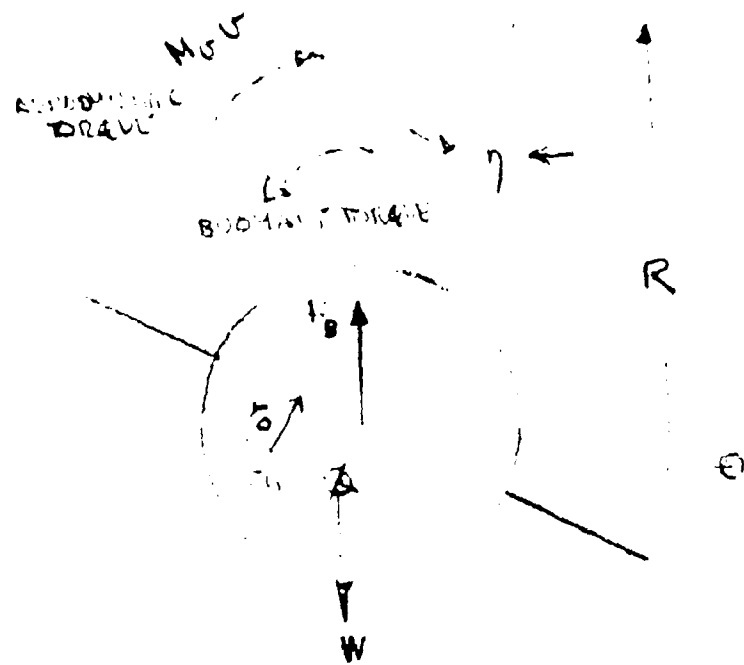
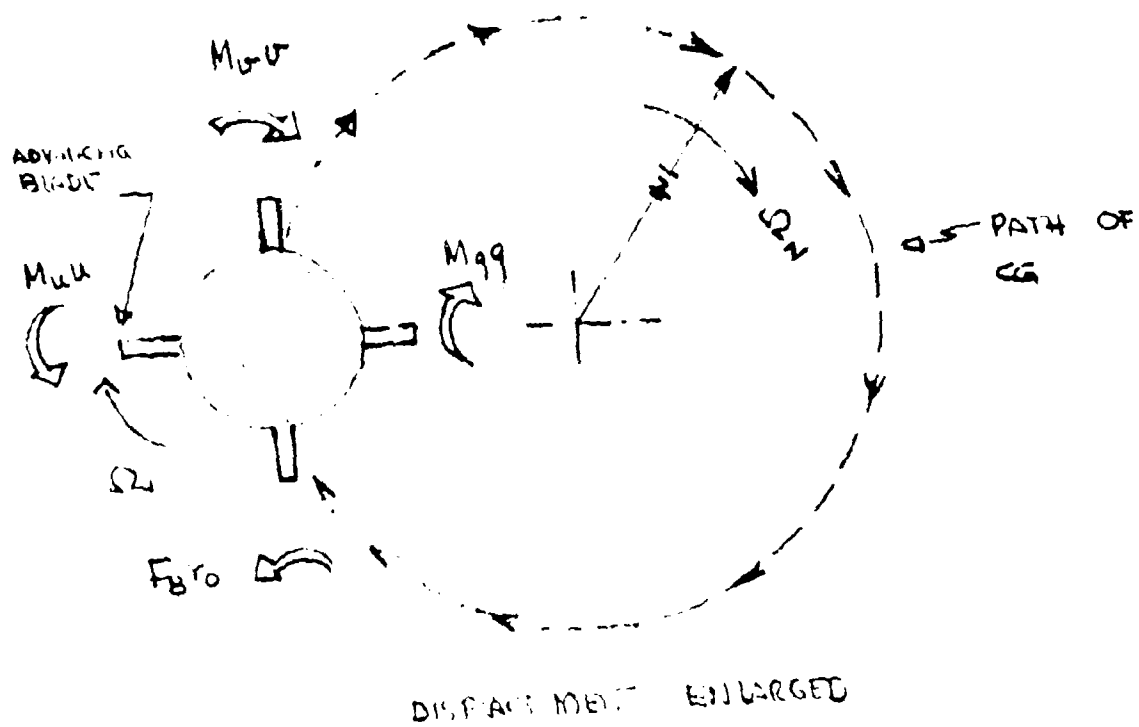


Figure 19. Physical Picture of Advancing Mode Motion.

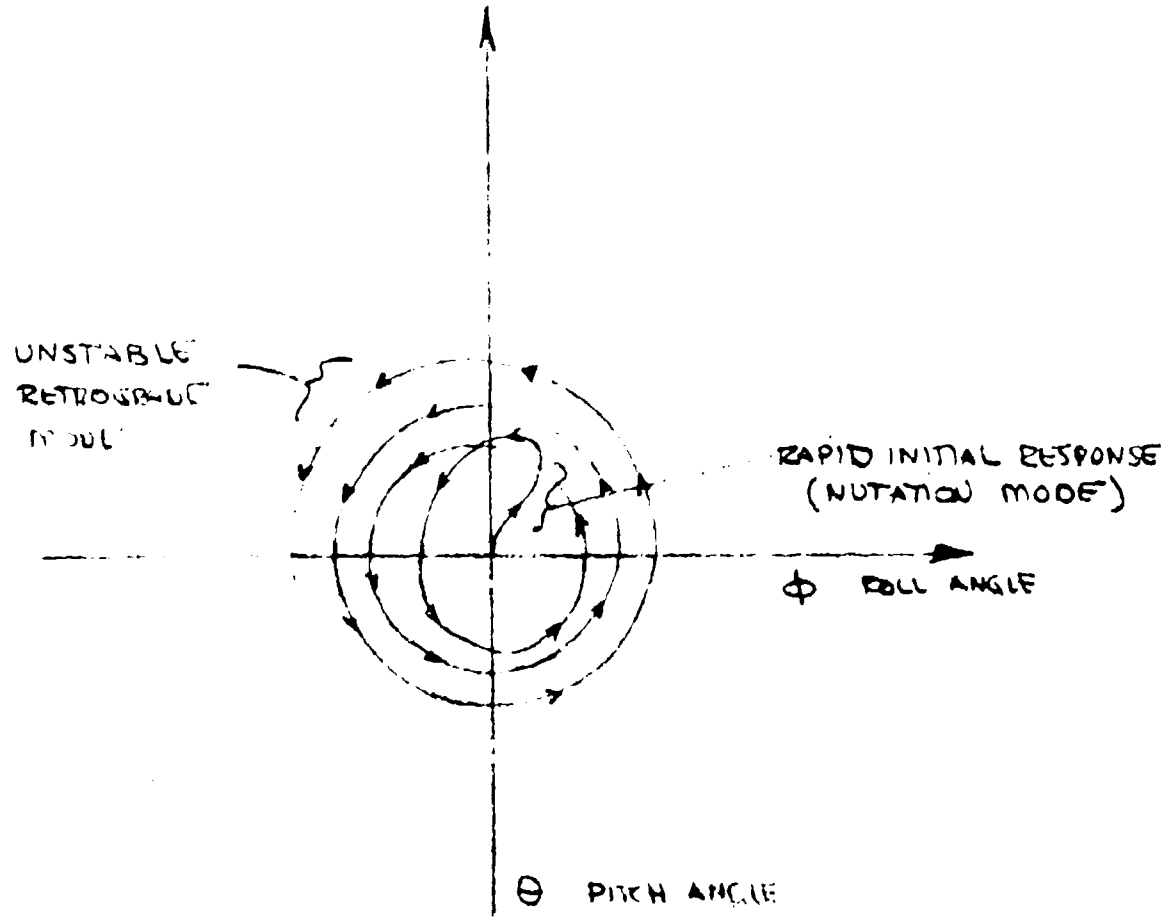


Figure 20. Typical Transient Response of AEROCRANE in Hovering Flight to Longitudinal Control Step Input.

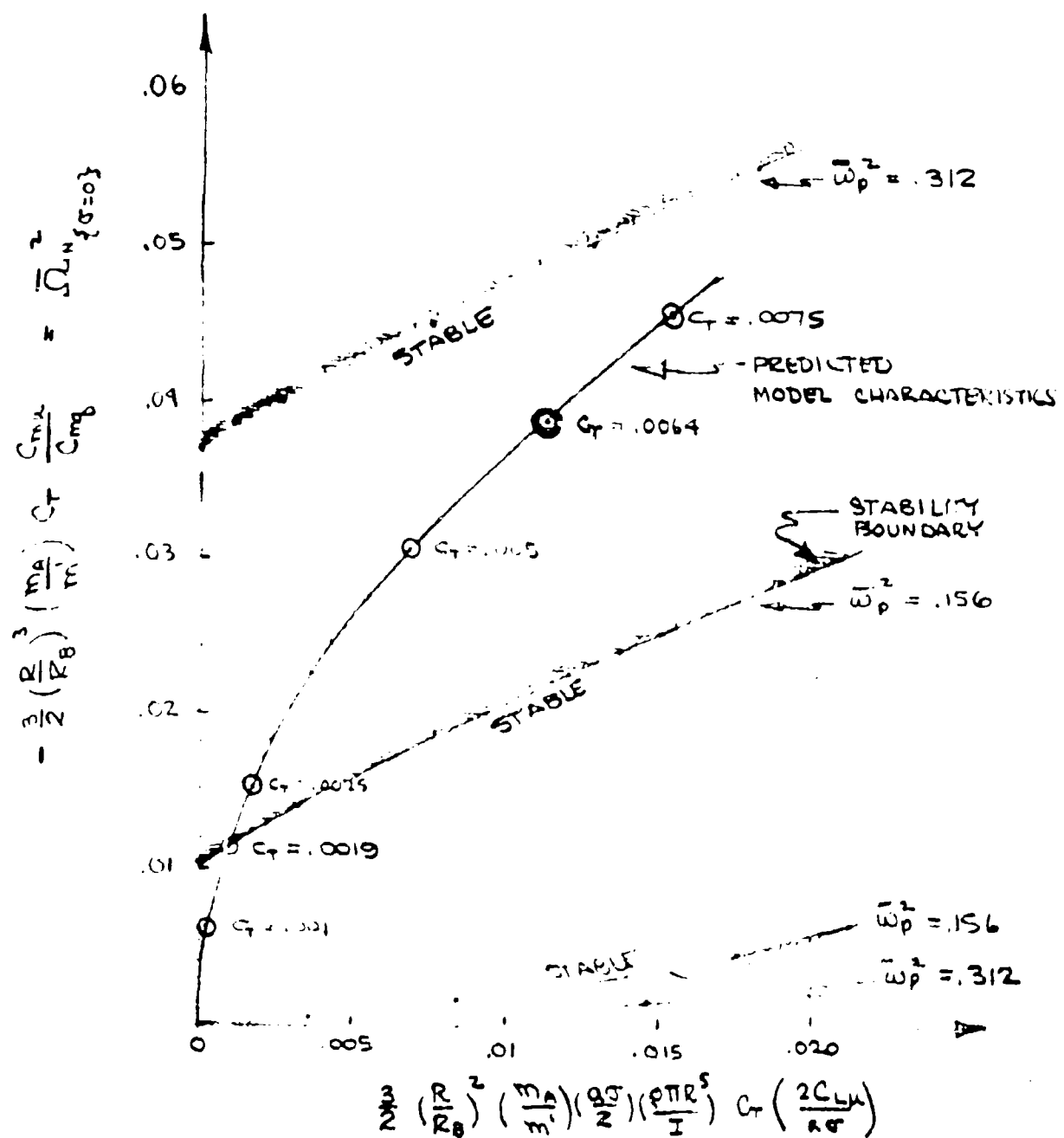


Figure 21. Stability Boundaries in Dimensionless Form Including Dependence of Model Characteristics on Thrust Coefficient.

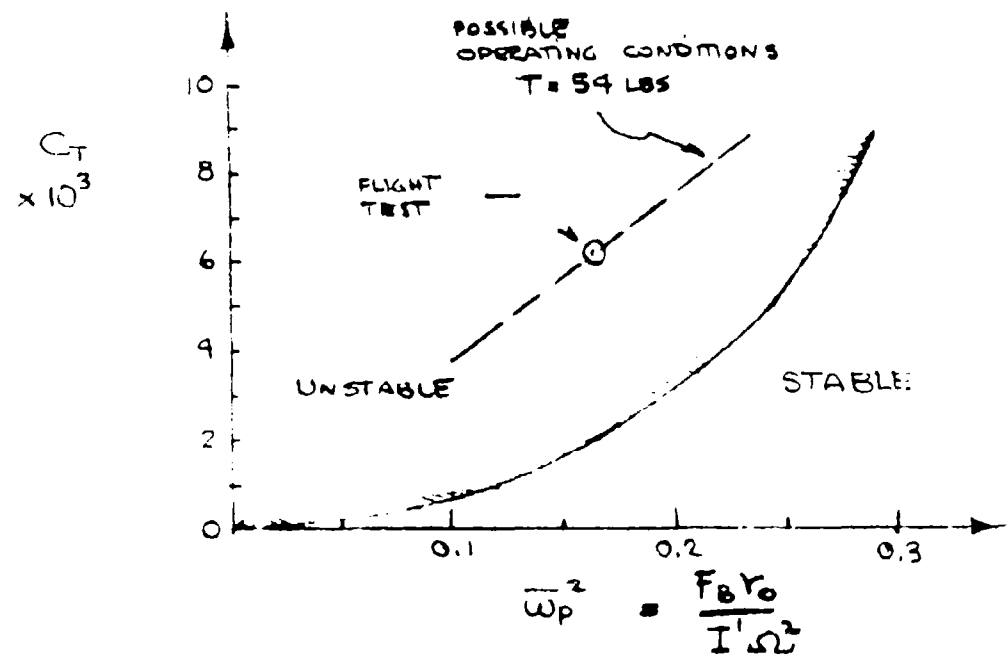


Figure 22. Dimensionless Stability Boundaries, Thrust Coefficient vs. Dimensionless Pendulous Frequency Squared.

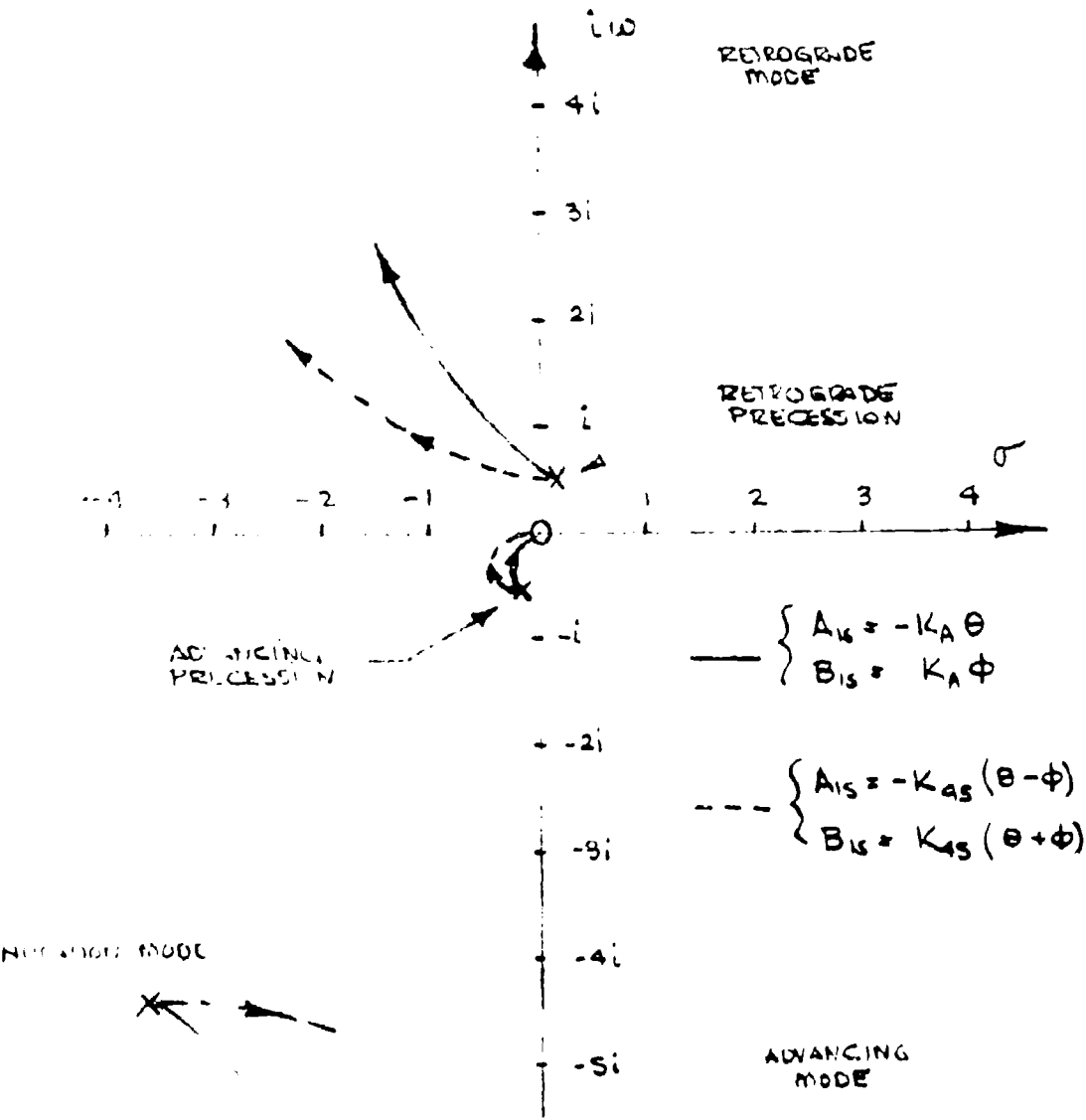


Figure 23. Root Locus, Dual Axis Attitude Feedback.

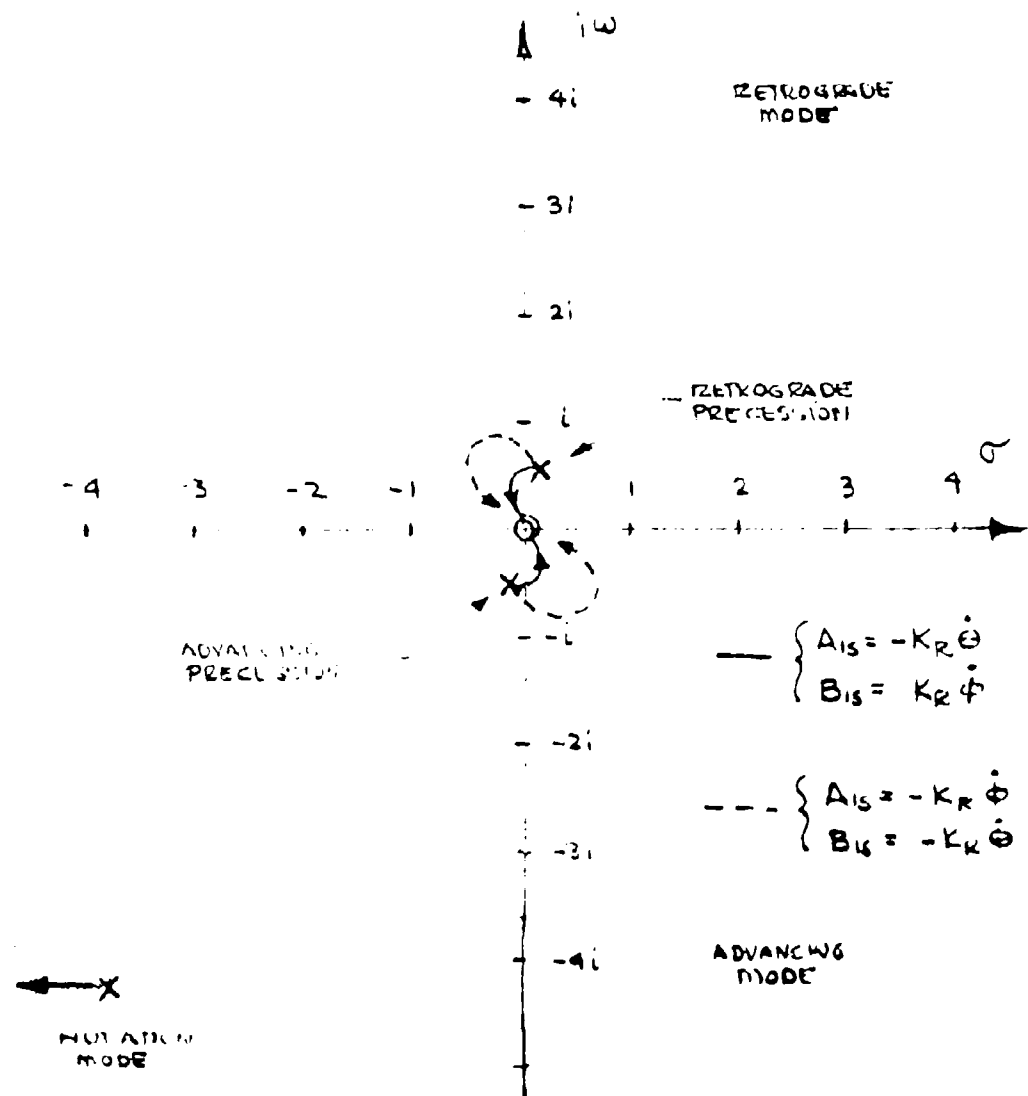


Figure 21. Root Locus, Dual Axis Rate Feedback.

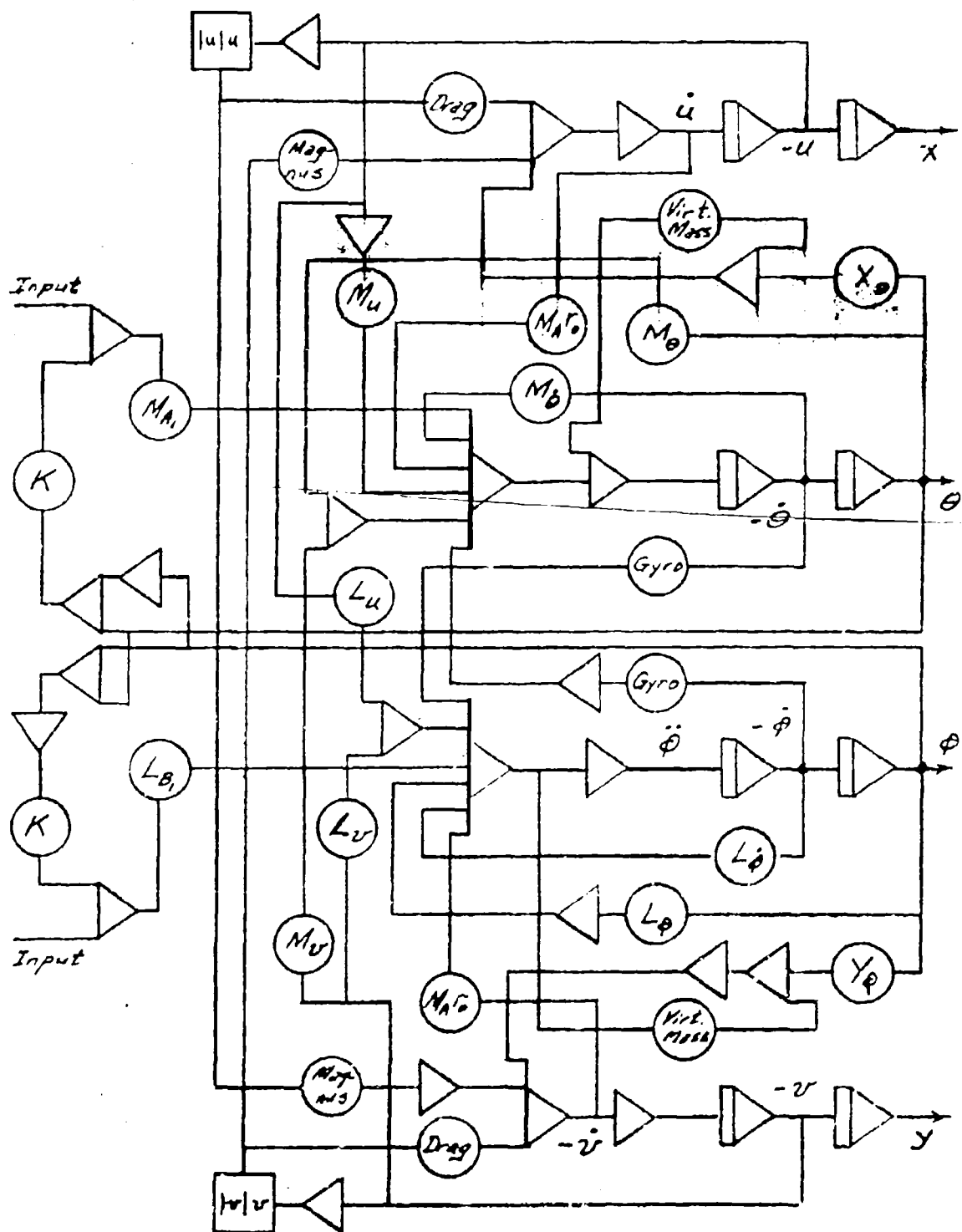


Figure 25. Analog Schematic

ANALOG SIMULATION OF UNSTABILIZED MODEL

Longitudinal 1.0-
Cyclic Pitch 0.5-

A_{1s} 0-

Degrees -0.5-
-1.0-

Pitch Rate 5.0-
2.5-

$\dot{\theta}$

Degrees / Sec. 0-
-2.5-
-5.0-

Pitch Attitude 10.0-
5.0-

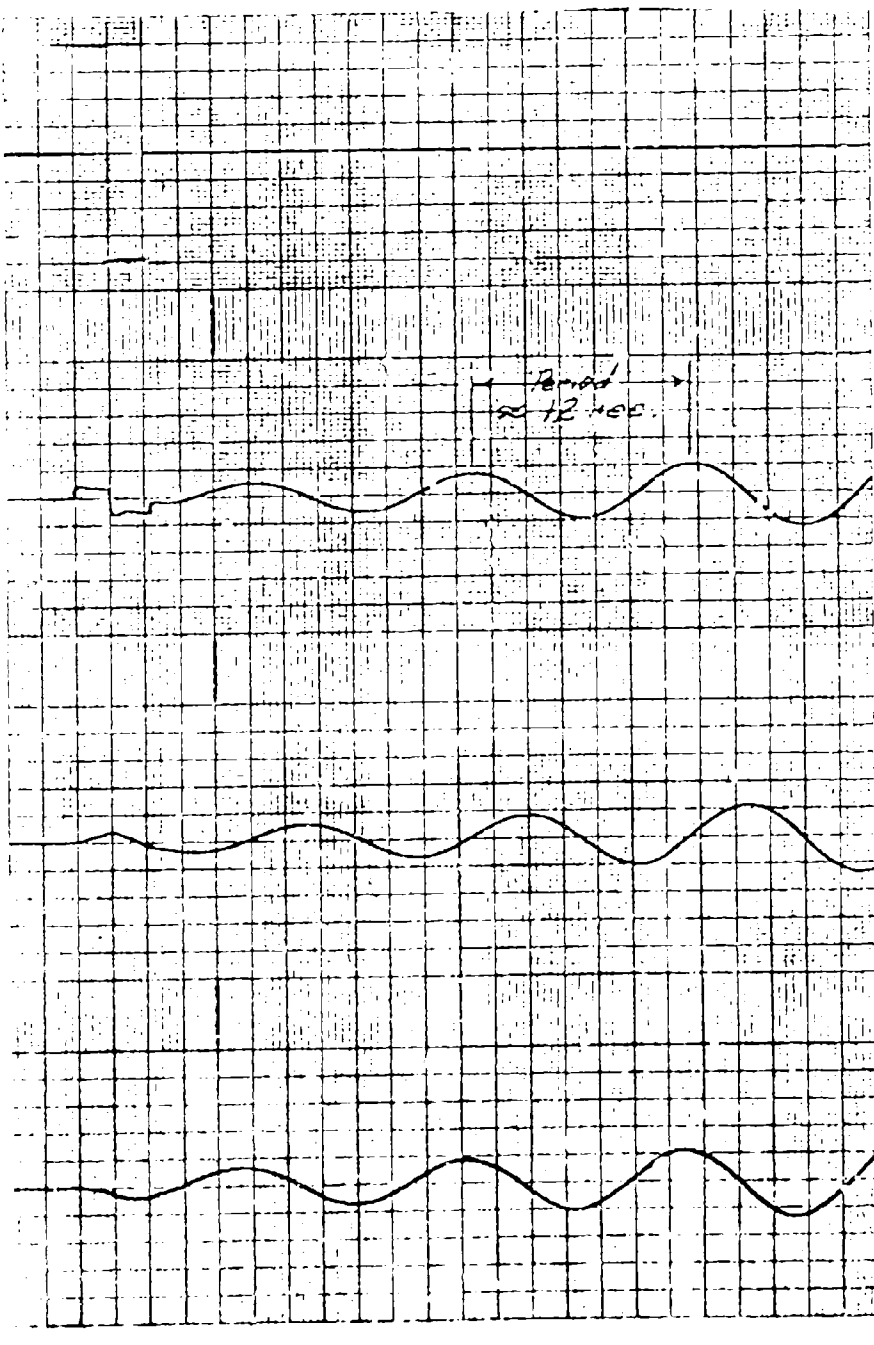
θ

Degrees 0-
-5.0-
-10.0-

Horizontal 2.0-
Velocity 1.0-

u

Ft. / Sec. 0-
-1.0-
-2.0-



Time, t , Sec.

10 Sec.

Figure 26. Time History - Nominal Configuration.

Comparison of
Analog Simulator
and Flight Data

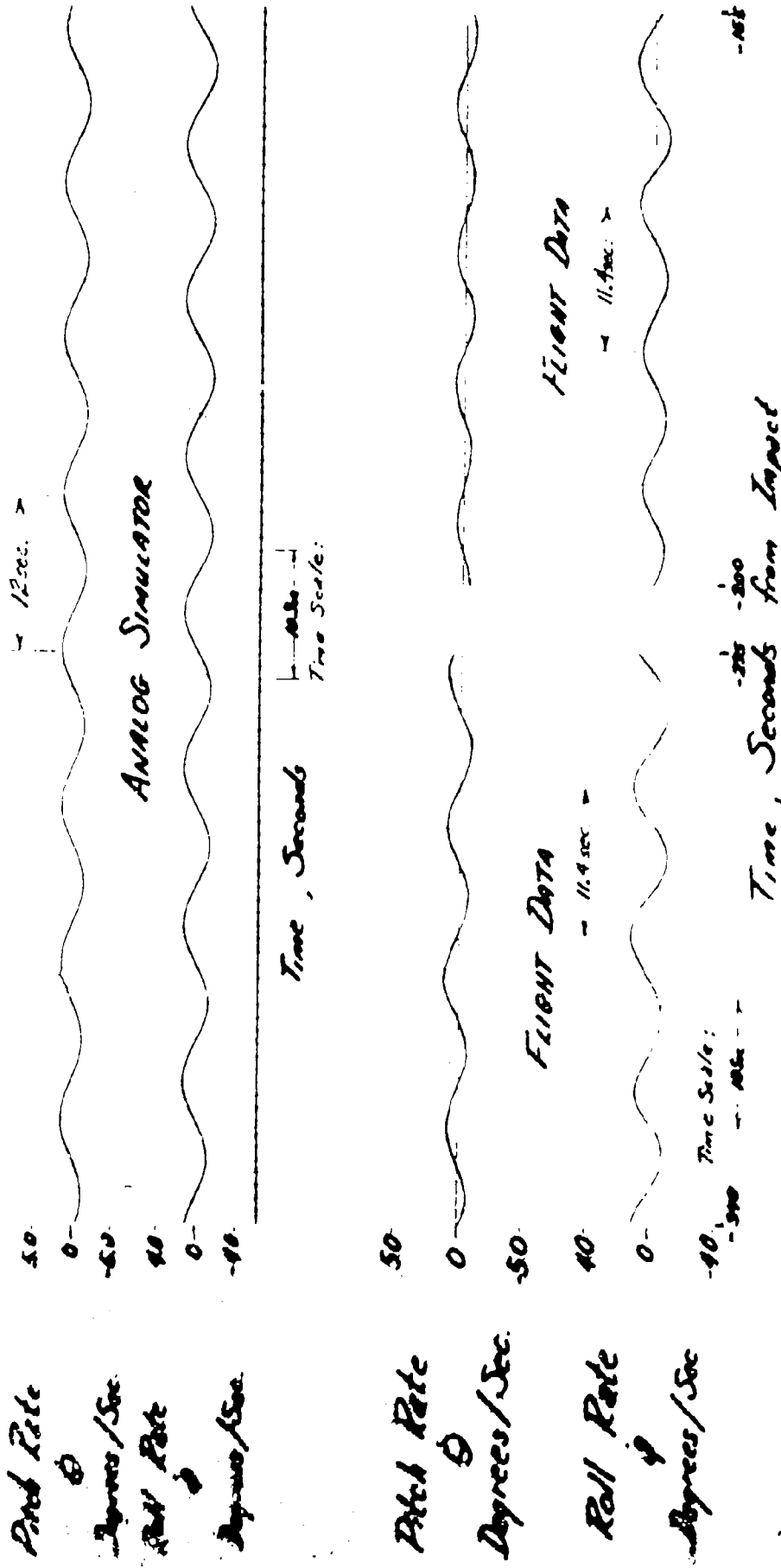


Figure 27. Time History - Nominal Configuration Limit Cycle as Compared to Flight Test Data

ANALOG SIMULATION OF
STABILIZED MODEL

$$A_{1s} = K(\phi - \theta), B_{1s} = K(\phi + \theta), K = 0.1\%$$

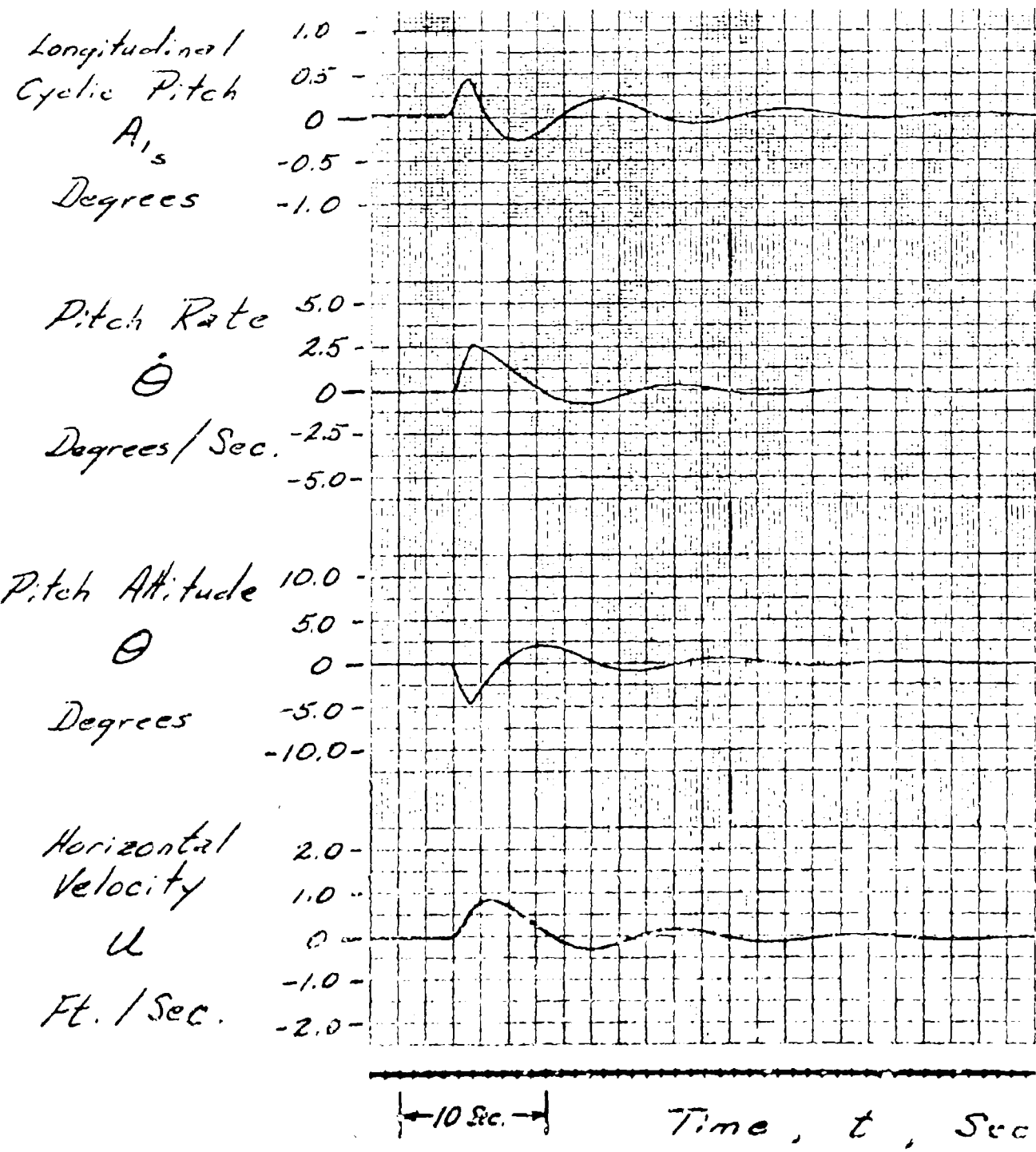


Figure 28. Time History - Crossed Attitude Feedback, $K_A = 0.1\%$.

APPENDIX A

ROTOR AERODYNAMICS

In this section the contributions of the rotor to the aerodynamics of the vehicle are developed. It is assumed in the following development that the rotor blades are infinitely stiff in flapping and have zero coning angle. It is also assumed that the blade element inflow angle is small and that the lift curve slope of the blades is constant. A shaft axis system is used as the reference frame for development of the rotor forces.

The only unusual feature as compared to conventional helicopter articulated rotor analysis is the inclusion of first harmonic components of the induced velocity. There are considered to be two sources of harmonic inflow.

The first arises from the fact that as the vehicle translates forward, the wake of trailing vorticity will be "blow back" causing a variation in induced velocity along the longitudinal axis of the rotor plane as pointed out by Coleman many years ago⁽⁷⁾. The importance of this effect is clearly shown for an articulated rotor in the experimental data presented by Harris⁽⁸⁾. This effect will be discussed at some length later in this section.

The second source of first harmonic induced velocity variation is a direct result of the fact that the rotor blades do not flap. Thus the effect of a change in any aerodynamic condition of the rotor (cyclic pitch, pitch rate) which produces a harmonic lift variation, rather than being

cancelled out by a flapping response as would be the case for an articulated rotor, remains. As a result it would be expected that a harmonic induced velocity variation would be produced. Limited experimental data⁽⁹⁾ on a rigid propeller have indicated that this effect is quite large and should be accounted for.

The blades employed on the model are untwisted and untapered and this is reflected in the aerodynamic model. For simplicity, the constant part of the induced velocity is assumed to be independent of radius although this would not, strictly speaking, be true for untwisted rotor blades in hovering⁽¹⁰⁾.

The rotor forces are developed using a shaft axis system with a relative wind orientation. That is, the longitudinal force $H_{s,w}$ is parallel to the relative wind and the side force $Y_{s,w}$ is perpendicular to the relative wind. Thus the following transformations must be considered to develop the velocity perturbation derivatives as shown in Figure A-1.

$$u = \sqrt{\bar{u}^2 + \bar{v}^2} \quad (A-1)$$

In coefficient form

$$C_{H_s} = C_{H_{s,w}} \frac{\bar{u}}{\sqrt{\bar{u}^2 + \bar{v}^2}} + C_{Y_{s,w}} \frac{\bar{v}}{\sqrt{\bar{u}^2 + \bar{v}^2}} \quad (A-2)$$

$$C_{Y_s} = C_{Y_{s,w}} \frac{\bar{u}}{\sqrt{\bar{u}^2 + \bar{v}^2}} - C_{H_{s,w}} \frac{\bar{v}}{\sqrt{\bar{u}^2 + \bar{v}^2}} \quad (A-2)$$

$$C_{M_s} = C_{M_{s,w}} \frac{\bar{u}}{\sqrt{\bar{u}^2 + \bar{v}^2}} + C_{L_{s,w}} \frac{\bar{v}}{\sqrt{\bar{u}^2 + \bar{v}^2}}$$

$$C_{L_s} = C_{L_{s,w}} \sqrt{\frac{\bar{u}}{u^2 + \bar{v}^2}} = C_{M_{s,w}} \sqrt{\frac{\bar{v}}{u^2 + \bar{v}^2}}$$

Owing to the wind axis formulation, the wind oriented forces and moments will be only a function of μ . Since hovering flight is of interest the equilibrium or trim values of all the forces and moments are zero as well as the initial values of the velocities \bar{v} and \bar{u} . Therefore, it can be seen that the following relationships hold for the translation derivatives in the body axis system.

$$\begin{aligned} \frac{\partial C_{H_s}}{\partial \bar{u}} &= \frac{\partial C_{H_{s,w}}}{\partial \mu} & \frac{\partial C_{H_s}}{\partial \bar{v}} &= \frac{\partial C_{Y_{s,w}}}{\partial \mu} \\ \frac{\partial C_{Y_s}}{\partial \bar{u}} &= \frac{\partial C_{Y_{s,w}}}{\partial \mu} & \frac{\partial C_{Y_s}}{\partial \bar{v}} &= -\frac{\partial C_{H_{s,w}}}{\partial \mu} \\ \frac{\partial C_{M_s}}{\partial \bar{u}} &= \frac{\partial C_{M_{s,w}}}{\partial \mu} & \frac{\partial C_{M_s}}{\partial \bar{v}} &= \frac{\partial C_{L_{s,w}}}{\partial \mu} \\ \frac{\partial C_{L_s}}{\partial \bar{u}} &= \frac{\partial C_{L_{s,w}}}{\partial \mu} & \frac{\partial C_{L_s}}{\partial \bar{v}} &= \frac{\partial C_{M_{s,w}}}{\partial \mu} \end{aligned} \quad (A-3)$$

These symmetry relationships are helpful in simplifying the dynamic analysis as shown elsewhere in this report.

Now the rotor forces and moments in the shaft/wind system are developed. Assuming that the inflow angle is small the expression for the average forces and moments expressed in terms of the lift and drag acting on a blade element are

$$\begin{aligned} T_{s,w} &= \frac{b}{2\pi} \int_0^{2\pi} \int_{R_s}^R dL \\ H_{s,w} &= \frac{b}{2\pi} \int_0^{2\pi} \int_{R_s}^R (dD - \phi dL) \sin \phi \end{aligned} \quad (A-4)$$

$$Y_{s,w} = \frac{b}{2\pi} \int_0^{2\pi} \int_{R_s}^R (dD - \phi dL) \cos \psi$$

$$M_{s,w} = -\frac{b}{2\pi} \int_0^{2\pi} \int_{R_s}^R r dL \cos \psi$$

$$L_{s,w} = \frac{b}{2\pi} \int_0^{2\pi} \int_{R_s}^R r dL \sin \psi$$

The lift and drag on the blade element can be expressed as

$$dL = \frac{1}{2} \rho (\Omega r)^2 c d r \sin \alpha_{st}$$

$$dD = \frac{1}{2} \rho (\Omega r)^2 c d r \delta \quad (A-5)$$

The angle of attack of the blade element is

$$\alpha_{st} = \theta + \phi$$

where

$$\theta = \theta_0 - A_{1s} \cos \psi - B_{1s} \sin \psi$$

and

$$\phi = \frac{\lambda_s + \Lambda_s \sin \psi + \Lambda_c \cos \psi}{x + u_s \sin \psi} \quad (A-6)$$

λ_s average inflow through the rotor and is defined as

$$\lambda_s = u_s \tan \alpha_s - v$$

The advance ratio

$$u_s = (\bar{u}^2 + \bar{v}^2)^{\frac{1}{2}} \cos \alpha_s \quad (A-7)$$

The harmonic inflow components represented by Λ_s and Λ_c arise due to pitch rate and roll rate and as a result of the harmonic inflow components discussed above. They may be expressed as:

$$\Lambda_s = (-\bar{p}x + \lambda_L) \quad (A-8)$$

$$\Lambda_c = (\bar{q}x + \lambda_m + \lambda_b)$$

where \bar{q} and \bar{p} are the pitch and roll rates non dimensionalized by rotor RPM, λ_b is the "blow back" effect and λ_L and λ_m represent the harmonic induced velocity components produced as a result of the harmonic lift variations.

Combining these expressions and performing the integrations indicated by equations (A-4) and nondimensionalizing the forces and moments, the force and moment coefficients are

$$\begin{aligned} \frac{2C_T}{\sigma} &= \theta_0 \left[\left(\frac{1-x^3}{3} \right) + \frac{\mu_s^2}{2} (1-x) \right] + (\lambda_s - u_s B_{1s}) \left(\frac{1-x^2}{2} \right) \\ &+ \frac{\mu_s}{2} \left(-\bar{p} \left(\frac{1-x^2}{2} \right) + \lambda_L (1-x) \right) \end{aligned} \quad (A-9)$$

$$\begin{aligned} \frac{2C_H}{\sigma} &= \frac{8\mu_s}{2\sigma} (1-x^2) - \frac{1}{2} \theta_0 \left[\lambda_L \left(\frac{1-x^2}{2} \right) - \bar{p} \left(\frac{1-x^3}{3} \right) + \mu_s \lambda_s \right] \\ &+ B_{1c} \left[\lambda_s \left(\frac{1-x^2}{4} \right) + \frac{3}{8} \mu_s (\lambda_L (1-x) - \bar{p} \left(\frac{1-x^2}{2} \right)) \right] \\ &+ \frac{\mu_s A_{1s}}{8} \left[\lambda_m (1-x) + \bar{q} \left(\frac{1-x^2}{2} \right) + \lambda_L \left(\frac{1-x^2}{2} \right) \right] \\ &- \lambda_s \left[\lambda_L (1-x) - \bar{p} \left(\frac{1-x^2}{2} \right) \right] \end{aligned}$$

$$\begin{aligned}
 \frac{2C_Y}{a\sigma} &= -\frac{6}{2} [\lambda_1 \left(\frac{1-x^3}{3}\right) + \lambda_m \left(\frac{1-x^2}{2}\right) + \bar{q} \left(\frac{1-x^3}{3}\right)] \\
 &\quad + A_{1s} \left[\lambda_s \left(\frac{1-x^2}{4}\right) + \frac{\mu_s}{2} (\lambda_1 (1-x) - \bar{r} \left(\frac{1-x^2}{2}\right))\right] \\
 &\quad + \frac{B_{1s} \mu_s^2}{8} [\lambda_m (1-x) + \bar{q} \left(\frac{1-x^2}{2}\right) + \lambda_1 \left(\frac{1-x^2}{2}\right)] \\
 &\quad - \lambda_s [\lambda_m (1-x) + \lambda_1 \left(\frac{1-x^2}{2}\right) + \bar{q} \left(\frac{1-x^2}{2}\right)]
 \end{aligned}$$

$$\begin{aligned}
 \frac{2C_M}{a\sigma} &= \frac{A_{1s}}{2} [(1-x^4) + \frac{\mu_s^2}{2} (1-x^2)] \\
 &\quad - \frac{1}{8} (3 + \lambda_1) (1-x^4) - \frac{1}{6} \lambda_m (1-x^3)
 \end{aligned}$$

$$\begin{aligned}
 \frac{2C_L}{a\sigma} &= -\frac{B_{1s}}{3} [(1-x^4) + \frac{3}{2} \mu_s^2 (1-x^2)] \\
 &\quad - \frac{1}{8} \bar{r} (1-x^4) + \frac{\lambda_1}{6} (1-x^3) \\
 &\quad + \mu_s [\frac{8}{3} (1-x^3) + \frac{\lambda_s}{4} (1-x^3)]
 \end{aligned}$$

x is the dimensionless location of the root of the rotor blade. The variation of the harmonic inflow components with radius has been taken as follows. The cosine component λ_s has been assumed to vary linearly with radius following Coleman, i.e., $\lambda_s = \lambda_1 x$. Since there is no simple theory to determine the variation of λ_m and λ_1 with radius, for simplicity they have been assumed to be independent of radius. Since their values are determined empirically by comparison with limited experimental data it is considered that this assumption is satisfactory.

Momentum theory is used to determine λ_s

$$\lambda_s = -\sqrt{\frac{C_T}{2(1-x^2)}} \quad (A-10)$$

Note that in the above all of the coefficients as well as the solidity are defined on total radius.

The harmonic inflow components λ_m and λ_L are determined by assuming that the magnitude of these components is proportional to the aerodynamic moment acting on the rotor⁽⁴⁾. Thus, it is assumed that

$$\lambda_m = j \frac{2C_M}{a\sigma} \quad \lambda_L = -j \frac{2C_L}{a\sigma} \quad (A-11)$$

where j is a constant of proportionality determined from experimental data. Reference 9 contains experimental data showing the moment produced by cyclic pitch application on a small rigid propeller and these data are used to determine the magnitude of j . Figure A-2 shows the experimental data.

Placing the first of the expressions above in the equation given above for $C_{M_{s,w}}$ and calculating the rate of change of pitching moment with cyclic, with $x = 0$, for a propeller,

$$\frac{2}{a\sigma} \frac{dC_{M_{s,w}}}{d\lambda_s} = \frac{\frac{1}{8}}{1 + \frac{1}{6}} \quad (A-12)$$

The experimental data present in Figure A-2 lies between values of j corresponding to rigid and non-rigid wake assumptions in Reference 11.

$$\frac{3}{4} \frac{a\sigma}{|\lambda_s|} < j < \frac{3}{8} \frac{a\sigma}{|\lambda_s|}$$

so the average of these two values is selected. Therefore,

$$J = \frac{1}{2} \frac{a\sigma}{\lambda_s} \quad (A-13)$$

Using this relationship, the expressions for the hub moments become

$$\frac{\partial C_{M_{s,w}}}{\partial \sigma} = \frac{1}{1 + \frac{a\sigma}{12\lambda_s} (1 - x^3)} \left\{ \frac{A_{1s}}{8} [(1 - x^4) + \frac{\mu_s^2}{2} (1 - x^2)] - \frac{1}{8} (\bar{q} + \lambda_1) (1 - x^4) \right\} \quad (A-14)$$

$$\frac{\partial C_{L_{s,w}}}{\partial \sigma} = \frac{1}{1 + \frac{a\sigma}{12\lambda_s} (1 - x^3)} \left\{ - \frac{B_{1s}}{8} [(1 - x^4) + \frac{3}{2} \mu_s^2 (1 - x^2)] - \frac{1}{8} \bar{p} (1 - x^4) + \mu_s [\frac{\theta}{3} (1 - x^3) + \frac{\lambda_s}{4} (1 - x^2)] \right\}$$

It can be seen that this effect reduces all the pitching moment derivatives by the same factor.

The remaining quantity to be predicted is λ_1 . The theoretical dependence obtained by Coleman is shown in Figure A-3. Since the interest here is near hovering flight the linear portion of the curve near hovering may be used. This can be approximated by

$$\lambda_1 \approx -\frac{\mu_s}{2} \quad (A-15)$$

Harris⁽⁸⁾ experimental data show that Coleman's result given in (A-15) as well as a number of other theories are in error by about a factor of two in predicting the lateral flapping of an articulated rotor at low advance ratios (see Figure 11 of Reference 8). This is in part no doubt due to the fact that Coleman assumes a linear distribution of λ_1 along the longitudinal axis such that

$$\lambda_0 = \lambda_1 x \quad (A-15)$$

and the lateral flapping depends upon the integral

$$\int \lambda_s x^2 dx \quad (A-16)$$

Similarly it may be shown that the hub moment on a rigid propeller produced by this effect depends on the same integral, and as a result is sensitive to the variation of λ_s near the tips. Data for the pitching moment acting on a rigid propeller are presented in Reference 12. Applying Coleman's theory to these data shows good agreement without adding the effect of the harmonic inflow due to the j factor. This effect is of course not present in Harris' data since a fully articulated rotor was employed. If the harmonic inflow effect is included in the prediction of the propeller hub moment, the prediction is in error by about a factor of two. Thus, good agreement with the magnitude of the "blow back" effect is obtained for both the articulated rotor and the rigid rotor if the value given by Coleman's theory is doubled and the j -factor determined from the experiments of Reference 9 is used. Therefore in the following

$$\lambda_1 = -\mu_s \quad (A-17)$$

The stability derivatives can now be calculated. Equation (A-17) gives

$$\frac{\lambda_1}{\delta \mu_s} = -1$$

The results are given for hovering flight although the expressions developed and presented in equations (A-9) are generally applicable to forward flight. The approximation given by (A-17) applies only near hovering as does the equation for the j -factor given by equation (A-13).

The thrust is found to be constant as a result of the linearization and as a consequence λ_s is constant, since α_s is defined as 0 for the hovering trim condition.

The stability derivatives are as follows. Interestingly all of the dimensionless pitching moment derivatives are equal with the exception of signs. That is

$$\frac{2}{a\sigma} \frac{\partial C_{M_{s,w}}}{\partial A_{1s}} = - \frac{2}{a\sigma} \frac{\partial C_{M_{s,w}}}{\partial \mu_s} = - \frac{2}{a\sigma} \frac{\partial C_{M_{s,w}}}{\partial q} = - \frac{2}{a\sigma} \frac{\partial C_{L_{s,w}}}{\partial B_{1s}} \quad (A-18)$$

The rolling moment derivatives are

$$\frac{2}{a\sigma} \frac{\partial C_{L_{s,w}}}{\partial B_{1s}} = - \frac{1}{8} \left(\frac{\frac{1 - x^4}{a\sigma}}{1 + \frac{a\sigma}{12\lambda_s} (1 - x^3)} \right) \quad (A-19)$$

$$\frac{2}{a\sigma} \frac{\partial C_{L_{s,w}}}{\partial p} = \frac{2}{a\sigma} \frac{\partial C_{L_{s,w}}}{\partial B_{1s}}$$

and

$$\frac{2}{a\sigma} \frac{\partial C_{L_{s,w}}}{\partial \mu_s} = \frac{1}{(1 + \frac{a\sigma}{12\lambda_s})} \left\{ \frac{\theta_0}{3} (1 - x^3) + \frac{\lambda}{4} (1 - x^2) \right\}$$

The body axis moment derivatives are given by relationships A-3

The force derivatives are as follows:

$$\begin{aligned} \frac{2}{a\sigma} \frac{\partial C_H}{\partial \mu_s} &= \frac{\delta}{2a} (1 - x^2) - \frac{1}{2} \theta_0 \lambda_s (1 - x) \\ &+ j [\theta_0 (\frac{1 - x^2}{4}) + \lambda_s (1 - x)] \frac{2}{a\sigma} \frac{\partial C_{L_{s,w}}}{\partial \mu_s} \end{aligned}$$

$$\frac{2}{a\sigma} \frac{\partial C_{H_{s,w}}}{\partial p} = \left(\frac{1}{6} \theta_0 (1 - x^3) + \frac{\lambda_s}{2} (1 - x^2) \right)$$

$$+ j [\theta_0 \left(\frac{1 - x^2}{4} \right) + \lambda_s (1 - x)] \frac{2}{a\sigma} \frac{\partial C_{L_{s,w}}}{\partial p}$$

$$\frac{2}{a\sigma} \frac{\partial C_{H_{s,w}}}{\partial B_{1s}} = \lambda_s \left(\frac{1 - x^2}{4} \right) + j [\theta_0 \left(\frac{1 - x^2}{4} \right) + \lambda_s (1 - x)] \frac{2}{a\sigma} \frac{\partial C_{L_{s,w}}}{\partial B_{1s}}$$

$$\frac{2}{a\sigma} \frac{\partial C_{Y_{s,w}}}{\partial \mu_s} = - [\theta_0 \left(\frac{1 - x^3}{6} \right) + \frac{\lambda_s}{2} (1 - x^2)] \frac{\partial \lambda_1}{\partial \mu} - j \left[\frac{\theta_0}{2} \left(\frac{1 - x^2}{2} \right) \right. \\ \left. + \lambda_s (1 - x) \right] \frac{2}{a\sigma} \frac{\partial C_{M_{s,w}}}{\partial \mu_s}$$

$$\frac{2}{a\sigma} \frac{\partial C_{Y_{s,w}}}{\partial \bar{q}} = - [\theta_0 \left(\frac{1 - x^2}{6} \right) + \lambda_s \left(\frac{1 - x^2}{2} \right)] \\ - j [\theta_0 \left(\frac{1 - x^2}{4} \right) + \lambda_s (1 - x)] \frac{2}{a\sigma} \frac{\partial C_{M_{s,w}}}{\partial \bar{q}}$$

$$\frac{2}{a\sigma} \frac{\partial C_{Y_{s,w}}}{\partial A_{1s}} = \lambda_s \left(\frac{1 - x^2}{4} \right) - j [\theta_0 \left(\frac{1 - x^2}{4} \right) + \lambda_s (1 - x)] \frac{2}{a\sigma} \frac{\partial C_{M_{s,w}}}{\partial A_{1s}}$$

For convenience in calculation note that the following equalities hold.

$$\frac{\partial C_{M_{s,w}}}{\partial A_{1s}} = - \frac{\partial C_{M_{s,w}}}{\partial \mu_s} = - \frac{\partial C_{M_{s,w}}}{\partial \bar{q}} = - \frac{\partial C_{L_{s,w}}}{\partial B_{1s}} = - \frac{\partial C_{L_{s,w}}}{\partial p}$$

$$\frac{\partial C_{H_{s,w}}}{\partial p} = - \frac{\partial C_{Y_{s,w}}}{\partial \bar{q}} = \frac{\partial C_{Y_{s,w}}}{\partial \mu_s}$$

$$\frac{\partial C_{H_{s,w}}}{\partial B_{1s}} = \frac{\partial C_{Y_{s,w}}}{\partial A_{1s}}$$

when

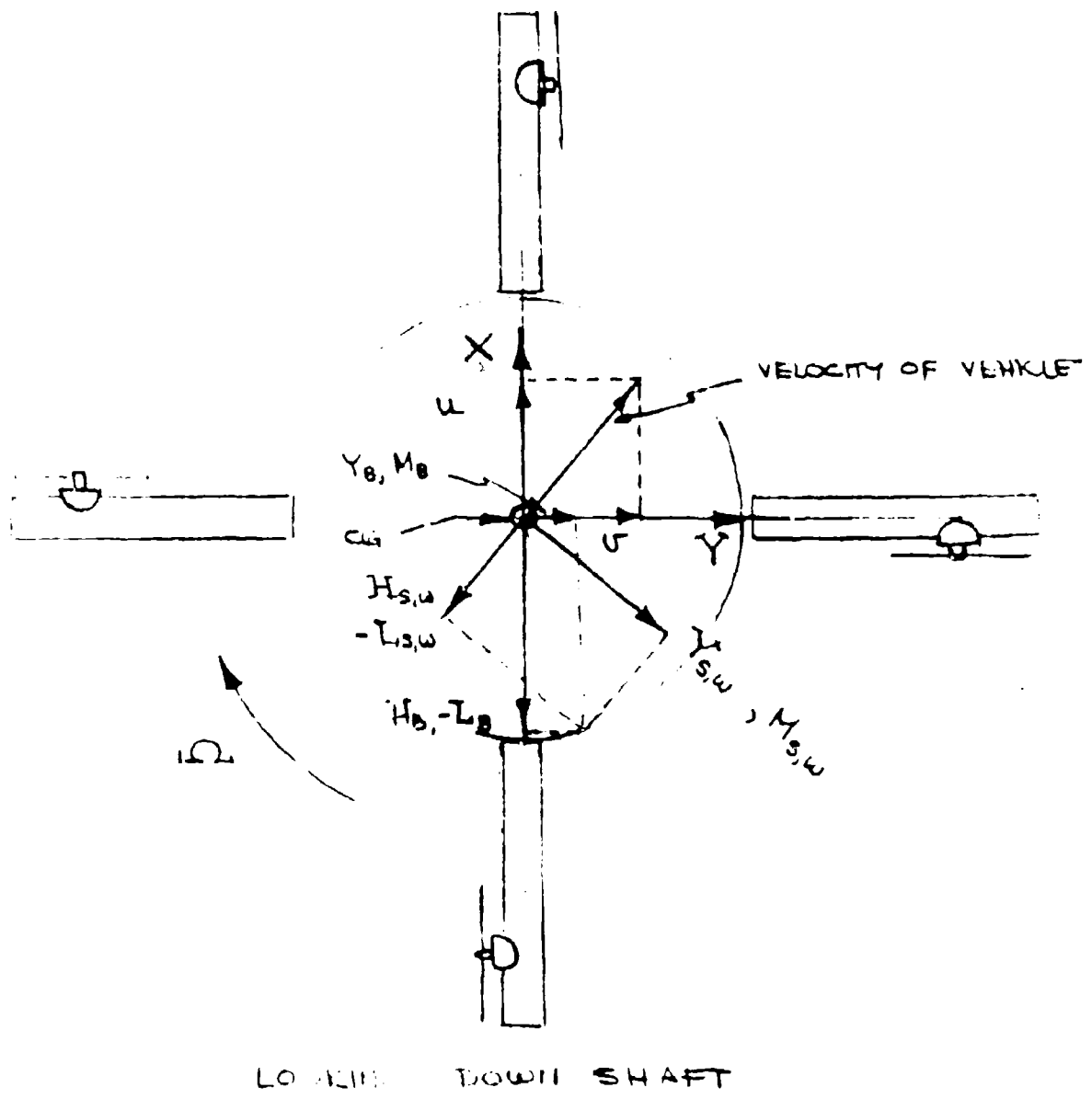
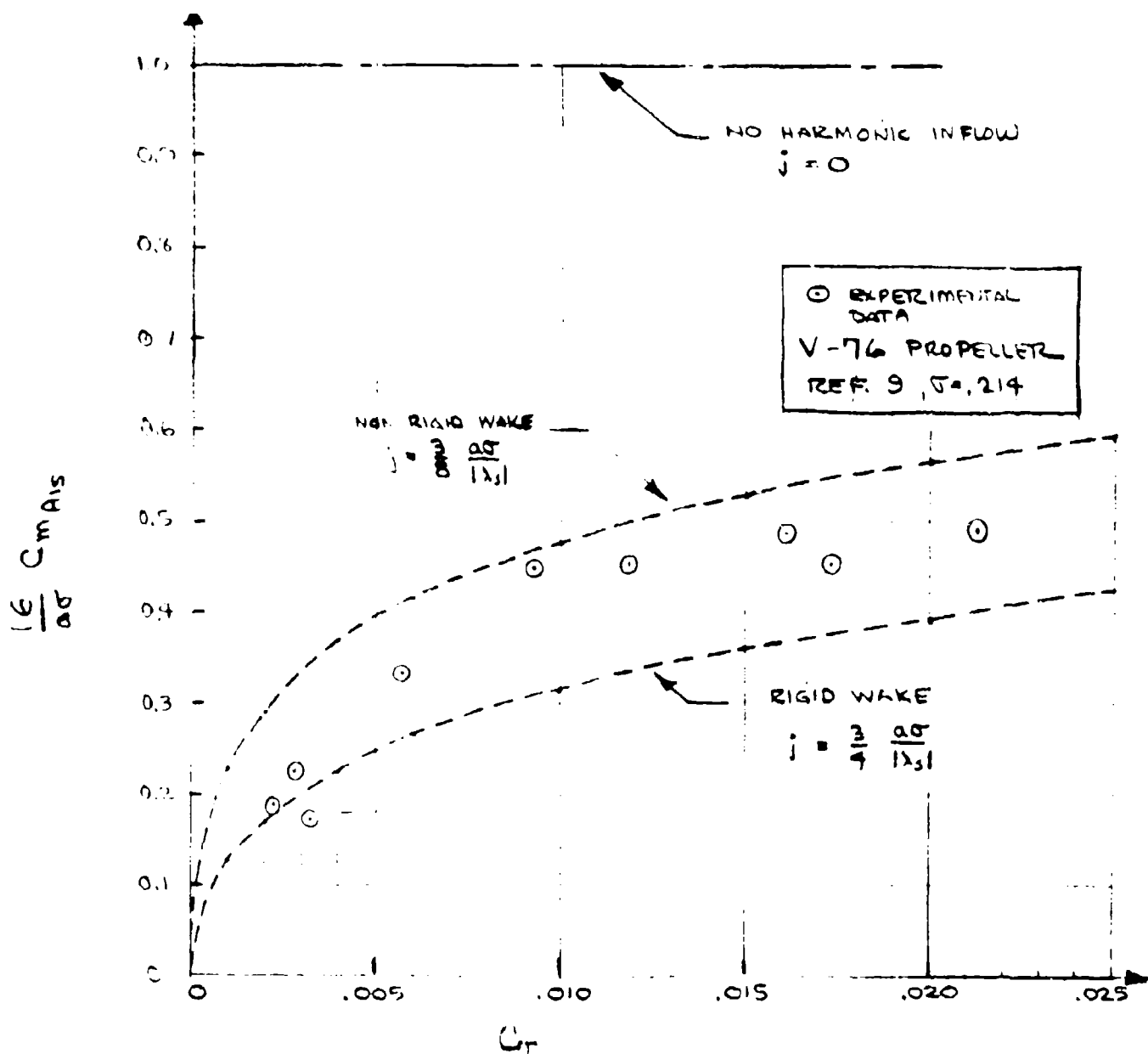


Figure A-1. Definition of Rotor Forces and Moments.



NOTE: THE CURVE IN REF. 9 HAS BEEN CONVERTED
TO THE COORDINATES OF THIS REPORT.

Figure A-2. Comparison of Theory and Experiment for Control Effectiveness of Rigid Propeller.

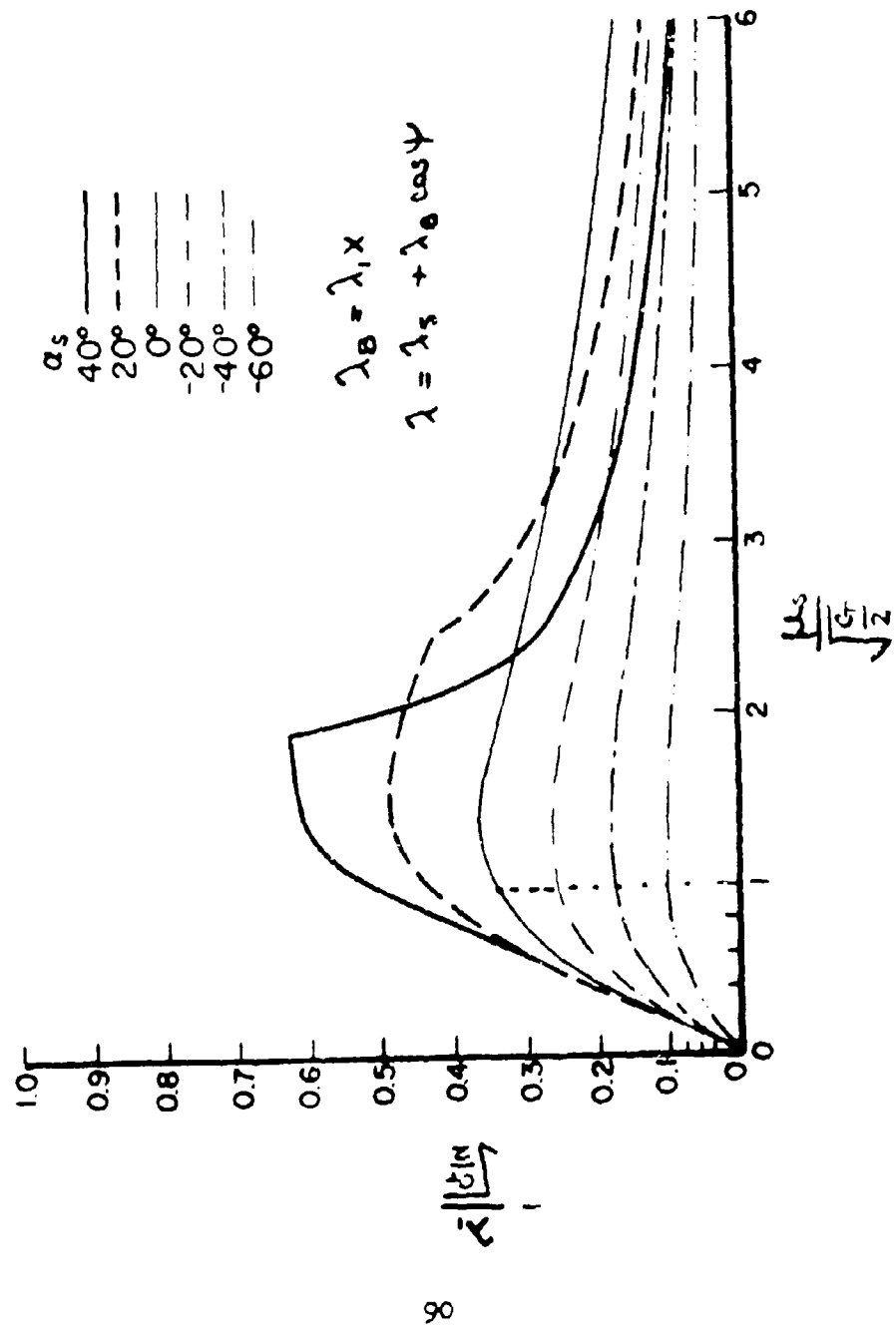


Figure A-3. Variation of cosine Component of induced velocity with Forward Speed and Angle of attack as Determined by Theory of Preference C.

APPENDIX B
Numerical Values for Stability Derivatives

The aerodynamic stability derivatives produced by the rotor were calculated based on the theory developed in Appendix A.

The pertinent model geometry and operating conditions are given below:

ρ = 34 lbs	m_0 = 5.95 slugs
ω = 30 RPM	m_1 = 2.65 slugs
r_0 = 3.62 ft	ρ = .00239 slugs/ft ³
h = 13.64 ft	I_0 = 337.4 slugs/ft ²
r_0 = 8 ft	c = 2.13 ft

In addition the value for the "blow back" effect as given by $\frac{\partial \lambda_1}{\partial u}$ was taken as twice the value given by the theory of Reference 7 as indicated by the experimental results of References 8 and 12.

Thus

$$\frac{\partial \lambda_1}{\partial u} = -1$$

The proportionality constant for the harmonic inflow effect j was based on the experimental data of Reference 9 as

$$j = \frac{a\sigma}{2\lambda_s}$$

The dimensionless stability derivatives are presented in Table B-I and the dimensional derivatives are presented in Table B-II.

The moment derivatives are the hub moments only since in all cases the moments due to the in-plane forces are less than two percent of

but greater. The moments due to the in-plane forces resulting from material inelasticity produce a small amount of control coupling (from \mathbf{C}_1 and \mathbf{C}_2). However, this represents less than a 2° shift in phase of the control and therefore was neglected in the computer analysis.

As a result of the small estimated magnitude of the control force derivatives they are neglected in the discussion on stability in other parts of this report.

TABLE D-1

DIMENSIONLESS STABILITY DERIVATIVES IN INVERTED POSITION

$$\frac{\partial}{\partial \sigma} C_T = .00540$$

$$\frac{\partial}{\partial \sigma} C_Y_{A_{15}} = .0599$$

$$\frac{\partial}{\partial \sigma} C_L_{B_{15}} = -.0599$$

$$\frac{\partial}{\partial \sigma} C_M_{\mu} = .0140$$

$$\frac{\partial}{\partial \sigma} C_L_{\mu} = .0140$$

$$\frac{\partial}{\partial \sigma} C_Y_{\bar{q}} = -.0599$$

$$\frac{\partial}{\partial \sigma} C_L_{\bar{p}} = -.0599$$

$$\frac{\partial}{\partial \sigma} C_I_{B_{15}} = -.0094$$

$$\frac{\partial}{\partial \sigma} C_I_{A_{15}} = -.0094$$

$$\frac{\partial}{\partial \sigma} C_H_{\bar{p}} = -.0017$$

$$\frac{\partial}{\partial \sigma} C_{\bar{q}} = .0017$$

$$\frac{\partial}{\partial \sigma} C_I_{\mu} = .0017$$

$$\frac{\partial}{\partial \sigma} C_L_{\mu} = .0027$$

TABLE B-11
INTERPOLATED STABILITY DERIVATIVES IN HOVERING (11)

$$M_{A_1} = -L_{n_{15}} = -12.24 \frac{\text{rad/sec}^2}{\text{rad}}$$

$$N_{\frac{1}{2}} = -L_{n} = -3.20 \frac{1}{\text{sec}}$$

$$M_u = -L_v = .200 \frac{1}{\text{ft-sec}}$$

$$L_u = M_v = .012 \frac{1}{\text{ft-sec}}$$

$$R_{B_1} = M_{A_{15}} = -1.05 \frac{\text{ft/sec}^2}{\text{rad}}$$

$$C_p = -C_q = -.23 \text{ ft/sec}^2$$

$$R_u = -C_v = .020 \frac{1}{\text{sec}}$$

$$R_v = -L_u = .013 \frac{1}{\text{sec}}$$

DISTRIBUTION

Commander
Naval Air Systems Command
Washington, DC 20361
Attention: AIR-954 (1 copy)
AIR-03 (1 copy)
AIR-03P3 (1 copy)
AIR-03P32 (1 copy)
AIR-320 (1 copy)
AIR-5301 (1 copy)

Chief of Naval Operations
Department of the Navy
Washington, DC 20350
Attention: OP-987 (1 copy)
OP-506E (1 copy)

Commander
Naval Facilities Engineering Command
200 Stovall Street
Alexandria, VA 22332
Attention: NFAC-03 (4 copies)

Superintendent
Naval Postgraduate School
Monterey, CA 93940
Attention: Library (1 copy)

Commander
Naval Air Development Center
Warminster, PA 18974
Attention: Code 31P3 (15 copies)
(1 Repos)

Commander
David W. Taylor Naval Ship Research and
Development Center
Bethesda, MD 20034
Attention: Director, Aerodynamics Laboratory (1 copy)

Chief of Naval Research
800 North Quincy Street
Arlington, VA 22217
Attention: Mr. T. Wilson, Code 461 (1 copy)

Commander
Naval Weapons Center
China Lake, CA 93555
Attention: Aerodynamics Branch, Code 4061 (1 copy)

ENCLOSURE (2)

DISTRIBUTION: (Continued)

Commander
Air Force Flight Dynamics Laboratory
Air Force Systems Command
Wright-Patterson Air Force Base, OH 45433
Attention: Library (1 copy)

Commander
U. S. Army Aviation Systems Command
St. Louis, MO 63166
Attention: Library (1 copy)

Director
U. S. Army Air Mobility Research and Development Laboratory
Ames Research Center
Moffett Field, CA 94035
Attention: Library (1 copy)

Director
Eustis Directorate
U. S. Army Air Mobility Research and Development Laboratory
Fort Eustis, VA 23604
Attention: Library (1 copy)
Mr. Robert Smith (1 copy)

Director
Langley Research Center
National Aeronautics and Space Administration
Hampton, VA 23365
Attention: Library (1 copy)

Director
Ames Research Center
National Aeronautics and Space Administration
Moffett Field, CA 94035
Attention: Library (1 copy)
Dr. Mark Ardema (1 copy)

Director of Forest Products and Engineering Research
U. S. Department of Agriculture, Forest Service
Washington, DC 20250
(2 copies)

Secretary
Department of Transportation
400 7th Street, S.W.
Washington, DC 20590
Attention: Assistant for Aeronautical R&D (1 copy)

DISTRIBUTION: (Continued)

Director
National Aeronautics and Space Administration
600 Independence Avenue
Washington, DC 20546
Attention: Director, Study and Analysis Office (1 copy)